Modelling Plasticity in Nanoscale Contact

THÈSE N^{O} 6443 (2014)

PRÉSENTÉE LE 31 OCTOBRE 2014
À LA FACULTÉ DE L'ENVIRONNEMENT NATUREL, ARCHITECTURAL ET CONSTRUIT
LABORATOIRE DE SIMULATION EN MÉCANIQUE DES SOLIDES
PROGRAMME DOCTORAL EN MÉCANIQUE

ÉCOLE POLYTECHNIQUE FÉDÉRALE DE LAUSANNE

POUR L'OBTENTION DU GRADE DE DOCTEUR ÈS SCIENCES

PAR

Till JUNGE

acceptée sur proposition du jury:

Prof. I. Botsis, président du jury
Prof. J.-F. Molinari, directeur de thèse
Prof. W. Curtin, rapporteur
Prof. N. Fillot, rapporteur
Prof. D. Warner, rapporteur

ÉCOLE POLYTECHNIQUE
FÉDÉRALE DE LAUSANNE
Suisse
2014

One must acknowledge [...]
no amount of violence will ever solve a math problem.
— Jacob Appelbaum

Acknowledgements

First of all, I owe many thanks to my supervisor, Professor Jean-François Molinari. Inexplicably, you hired me within the first moments of my job interview and once I joined the group, you gave me a great deal of freedom when it came to choosing my research topic and methods. I am still not sure how I deserved this high level of trust, but I am deeply grateful for it. Even with all this freedom and autonomy, you did not let me feel alone or unsupervised and provided invaluable guidance whenever I needed it.

It was Doctor Guillaume Anciaux who taught me about the implementations of molecular dynamics calculations and multiscale methods when I first arrived in the laboratory. As a curious person with a tendency to underestimate problems and overestimate my abilities to solve them, I have relied on your help and time for sometimes endless discussions more than I would like to admit. Instead of treating me like the burden that I was, you extended me your friendship. Thank you, also for all the steak overflows and raclettes with your favourite chocolate cream dessert at your place.

Doctor Nicolas Richart became a good friend of mine almost as soon as he joined the laboratory and today we share many interests and hobbies. Besides making the laboratory a more fun place to work at, your inexhaustible knowledge of software development and the GNU/Linux operating system combined with your readiness to have hour-long discussions about all things technical has helped me immensely to become a better coder. I am looking forward to more robots, roast piglets, geocaches, bike tours and discussions that do not need to be ended just because we both agree.

Special thanks go to our administrator, Birgitte Seem. You shielded me from paperwork so efficiently, that it always came as a big surprise whenever I actually had to deal with some myself. It is a universally known fact that I cannot handle even the simplest bureaucratic processes correctly, so you saved my neck many times over.

I would like to thank all members of LSMS, I really enjoyed my time here, thanks to the great atmosphere you provide. Special thanks go to David Kammer, my office mate of many years; our daily chats have not only allowed me to keep up with all the institutional gossip or let off some steam when one of us reached critical stress levels, but often were a highlight of the work day. I am looking forward to settling all those Jüngers and Doktors on our blackboard.

Professor Bill Curtin gave me the idea for my main research project. You hosted me at Brown University to teach me the intricacies of CADD and counselled me at every step of the CADD3D development. Without you, I do not know what I would have worked

on these past years, but I am sure it would have been much less interesting.
I would also like to thank the members of my jury, the Professors Derek Warner, Nicolas Fillot, Bill Curtin, Jean-François Molinari and Ioannis Botsis for their time and the warm compliments I received from them.
My partner, Sandra Penić, stuck with me throughout my thesis, even when I was not easy to be around. None of this would have been possible without your support and love. Thank you for all the help and understanding during the stressful times and the joy and happiness during the good times, I love you and cannot wait to start the next chapter in my life with you.
A big thank you also to my parents, Jacqueline and Hans-Hermann. You always supported me in my choices and helped me every step of my way. Even though I am (technically) a grown-up and should be able to get along on my own, I could still rely on you when I needed help. When Sandra and me were so busy and had to move into the new apartment, you managed an army of helpers and orchestrated what must be the quickest and most efficient moving day in human history. That was legendary! I thank you for all the love and safety you give me. And my big sister Anne-Laure, you always believed in me, even when I wasn't that sure at all; thank you.
Thank you also, Andres Müller, for those insane week-ends in Stockholm, the countless steaklettes and movie nights, the commiseration and shared suffering over our theses, and, above all, your friendship. Thank you also Constantin and Marketa Niemeyer, Patrica Scheuber, Arnaud Moretti, David Suter, Ruben Andrist, Patrick Vogt, Patrick Gubser, Steffen Ruthotto and Etienne Huber, for your friendship, especially towards the end of my thesis, when I did not make enough time for you!
My work was supported by the European Research Council (ERCstg UFO-240332).

Lausanne, October 16, 2014 Till Junge

Résumé

Le contact mécanique est un problème fondamentalement multi-échelles. Des effets atomistiques qui violent les hypothèses de la mécanique des milieux continus dominent les déformations d'aspérités en contact, tandis que l'interaction entre aspérités distantes est gouvernée par l'élasticité à longue portée. Cette thèse se concentre sur la modélisation numérique du contact entre métaux cristallins avec friction à l'échelle nanoscopique en utilisant à la fois des méthodes atomistiques mono-échelle et en améliorant les méthodes multi-échelles concurrentes.

Je présente une nouvelle approche pour quantifier le travail de frottement et l'énergie associée à l'activité plastique dans les simulations de dynamique moléculaire. Afin de déterminer l'importance des effets de taille de la boîte de simulation, de microstructure ou de vitesse de rayure, la méthode est appliquée, en combinaison avec un critère statistique, à une vaste étude paramétrique de rayure nanoscopique sur substrats en aluminium mono- ou polycristallins. Certaines différences fondamentales dans les mécanismes de frottement entre substrats monocristallins et polycristallins sont présentées.

L'étude montre aussi les limitations de la modélisation mono-échelle et met en avant l'importance du développement de méthodes multi-échelles appropriées pour la plasticité à l'échelle nanoscopique. La méthode de l'atomistique couplée à la dynamique des dislocations discrètes (Coupled Atomistics and Discrete Dislocations ou « CADD », en anglais) en est un exemple limité jusqu'à présent aux problèmes bidimensionnels. Une version tridimensionelle de la méthode CADD est présentée de manière théorique ainsi qu'un plan détaillé de son implementation efficace. Les fondements de CADD tridimensionel sont présentés par le biais de cas tests pratiques.

CADD évite les forces fantômes le long des interfaces de couplage en couplant les déplacements. Je montre que de manière générale, les méthodes de couplage des déplacements souffrent d'une instabilité dynamique intrinsèque qui les rend particulièrement mal adaptées au calcul à température finie, malgré leur utilisation répandue. L'instabilité est analysée en détails. De multiples remèdes pour la gérer sont discutés et une solution fondamentale au problème sous-jacent est présentée sous forme d'une nouvelle méthode de couplage.

Mots clés : science numérique des matériaux, mécanique numérique du contact, nanotribologie, plasticité, modèles multi-échelles concurrentes, dynamique moléculaire, dynamique des dislocations discrètes, méthode des éléments finis

Abstract

The problem of mechanical contact is a truly multiscale one. Atomistic effects that violate continuum theory dominate the deformations of contacting asperities, while the interactions between distant asperities occur through long-range elasticity. This thesis concentrates on the numerical modelling of nanoscale frictional contact between crystalline metals by using both single-scale atomistic methods and improving concurrent multiscale methods.

A novel approach to quantify frictional work and the energy associated with plastic activity in molecular dynamics simulations is presented. In combination with a statistical criterion to determine the significance of simulation box size, microstructure and sliding rate effects on the frictional quantities such as the friction coefficient and stored plastic energies, the method is used in a large parametric molecular dynamics study of single-asperity nanoscratch on monocrystalline and polycrystalline aluminium substrates. Some fundamental differences in the friction mechanisms between monocrystalline and polycrystalline substrates are presented.

The study shows the limitations of single-scale modelling and highlights the importance of developing appropriate multiscale methods for nanoscale plasticity. One such method is the Coupled Atomistics and Discrete Dislocations (CADD), which previously only existed for two-dimensional problems. A three-dimensional version of the CADD method is presented theoretically as well as a detailed practical road map for its efficient implementation. The foundations of three-dimensional CADD are presented using practical test cases.

CADD avoids ghost forces at the coupling interfaces through displacement-coupling. I reveal that such displacement-coupling methods generally exhibit an inherent dynamic instability which makes them particularly ill suited for finite temperature calculations, despite their wide use. The instability is analysed in detail. Multiple remedies to manage it are discussed and a fundamental solution to the underlying problem is presented in the form of a new coupling method.

Key words: Computational Materials Science, Computational Contact Mechanics, Nanotribology, Plasticity, Concurrent Multiscale Modelling, Molecular Dynamics, Discrete Dislocation Dynamics, Finite-Element method

Contents

Acknowledgements **i**

Abstract (Français/English) **iii**

List of Figures **xi**

List of Tables **xvii**

1 Introduction **1**

Introduction **1**

1.1 Motivation . . . 1
1.2 Objectives . . . 3
1.3 Challenges . . . 3
1.4 Contributions to the Field of Contact Modelling in Computational Material Science . . . 4
1.5 Organisation . . . 5

2 State of the Art **7**

2.1 Continuum Modelling . . . 7
2.2 Mesoscale Modelling . . . 8
2.2.1 Crystal Dislocations . . . 8
2.2.2 Discrete Dislocation Dynamics . . . 10
2.3 Atomistic Modelling . . . 14
2.4 Multiscale Modelling . . . 15
2.4.1 The Quasi-Continuum (QC) and Coupling of Length Scales (CLS) Methods . . . 20
2.4.2 The Bridging Domain Method (BDM) . . . 21
2.4.3 The Bridging Scale Method (BSM) . . . 21
2.4.4 The Composite Grid Atomistic Continuum Method (CACM) . . . 22
2.4.5 The Finite Element Combined with Atomistic (FEAt) Modelling . 23
2.4.6 The Method of Coupled Atomistics and Discrete Dislocations (CADD) . . . 23
2.4.7 The Hybrid Simulation Method (HSM) . . . 24

2.4.8 Comparisons between the Methods . . . 24

3 Plastic Activity in Nanoscratch Molecular Dynamics Simulations of Pure Aluminium 27

3.1 Molecular Dynamics Setup . . . 28
3.1.1 Single Crystal Case . . . 28
3.1.2 Polycrystal Simulations . . . 30
3.1.3 Parameter Space . . . 33
3.1.4 Simulations . . . 33
3.2 Computation of Stored Plastic Energy . . . 34
3.2.1 Energy Balance in Molecular Systems . . . 34
3.2.2 Evolution of Stored Plastic Energy . . . 34
3.3 Simulation Results . . . 37
3.3.1 Work and Plasticity . . . 37
3.3.2 Plasticity and Dislocation Activity . . . 39
3.3.3 Friction Coefficient . . . 40
3.3.4 Influence of the Microstructure . . . 44
3.4 Conclusions . . . 51

4 A Road Map Towards 3D CADD 53

4.1 Differences Between 2D and 3D CADD . . . 53
4.1.1 Dislocation Passing . . . 53
4.1.2 Dislocation Detection . . . 56
4.2 Road Map and Achieved Mile Stones . . . 57
4.2.1 Coupling Framework . . . 58
4.2.2 External Software Projects . . . 59
4.2.3 Milestones . . . 59
4.3 Periodic Array of Straight Dislocations . . . 66
4.4 Dislocation Core Template . . . 71
4.4.1 Computing a Basic Core Template . . . 74
4.5 Straight Hybrid Dislocations . . . 77
4.6 Coupled Frank-Read Source . . . 82
4.7 Conclusions . . . 86

5 Dynamic Stability of Ghost Force-Free Atomistic/Continuum Coupling Methods 87

5.1 Instability in Displacement Coupling (CADD): Numerical Examples . . . 88
5.1.1 CADD Revisited . . . 88
5.1.2 Instability of the One-Dimensional Problem . . . 89
5.2 Stability Analysis . . . 93
5.2.1 Simple One-Dimensional Displacement Coupling Case . . . 93
5.2.2 Simplified Model with Traction-Compression Asymmetry . . . 96
5.3 Strategies to Achieve Stability or Manage Instability . . . 99

5.3.1 Quasistatic Continuum . . . 100
5.3.2 Thermostatting . . . 101
5.3.3 Force-Coupling . . . 101
5.3.4 Harmonic Buffer Layer . . . 102
5.3.5 A Few Words on the Bridging Domain Method . . . 104
5.3.6 Three-Dimensional Problem . . . 105

6 Concluding Remarks and Outlook 109
6.1 Summary . . . 109
6.1.1 Single Scale Work . . . 109
6.1.2 Multiscale Work . . . 110
6.1.3 Main Contributions . . . 110
6.2 Outlook . . . 110
6.2.1 Immediate Future Work without Software Development . . . 110
6.2.2 New Software Developments . . . 111
6.2.3 New Types of Studies Made Possible by Developments . . . 112

A Fitting the Lennard-Jones Parameters 113

B On-Demand Update Strategy for Quasistatic Continuum 117

C Rotation of Elastic Tensors 119

Bibliography 130

Curriculum Vitae 131

List of Figures

1.1 Roughness hypothesis: The friction force F is the force necessary to push a load N over the steepest contacting asperity slope $\tan\alpha$. 2

2.1 Simple straight dislocations 9

2.2 Discrete dislocation dynamics problem, linearity is exploited to use superposition of elastic and plastic (dislocation) solution. 11

2.3 Planar discrete dislocation dynamics 12

2.4 Dislocation network represented as a set of “nodes” interconnected by straight segments. Empty circles represent simple computational discretisation nodes. The full disk (node 0) is both a computational node and a physical node, since it represents a dislocation triple-juncture. Note that two neighbouring segments have the same Burgers vector if the connecting node is a simple discretisation node. The sum of all incoming Burgers vectors matches the sum of all outgoing Burgers vectors across a node. . . 13

2.5 Generic partitioned-domain problem. The interface between the atomistic domain Ω_A and the continuum domain Ω_C can be a sharp interface $\partial\Omega_\mathrm{AC}$ or a finite coupling region Ω_I. 16

2.6 Two-dimensional schematic for sharp interface coupling with strong compatibility. The sharp interface $\partial\Omega_\mathrm{AC}$ separates the domains Ω_A and Ω_C unambiguously, *i.e.* a degree of freedom is either in Ω_A or Ω_C. All atoms in Ω_A are free molecular dynamics atoms (solid disks) and the finite-element boundary nodes move with them. In Ω_C, the nodes are governed by the finite-element method and pad atoms (empty circles) behave as if glued to the underlying elements. 18

2.7 Two-dimensional schematic for sharp interface coupling with weak compatibility. The sharp interface $\partial\Omega_\mathrm{AC}$ separates the domains Ω_A and Ω_C unambiguously, *i.e.* a degree of freedom is either in Ω_A or Ω_C. All atoms in Ω_A are free molecular dynamics atoms (solid disks) and the finite-element boundary nodes move with them. In Ω_C, the nodes are governed by the finite-element method and pad atoms (empty circles) behave as if glued to the underlying elements. 19

2.8 Two-dimensional schematic of coupling interface with handshake region. The subdomains Ω_A and Ω_C overlap in the handshake region Ω_I. Fully free molecular dynamics atoms are represented by solid disks, whereas the empty disks represent pad atoms. The empty squares in are partially constrained coupling atoms in the handshake region Ω_I. For instance the BDM method (Section 2.4.2) uses this type of coupling. 20

3.1 Simulation setup 29

3.2 Example of a polycrystalline microstructure. Atoms are coloured by grains which are defined by the cells of a Voronoi tessellation of 200 randomly distributed points in the substrate geometry. Each Voronoi cell is assigned a random lattice orientation and filled with atoms. The structure is heated, annealed under isostatic pressure, and quenched before the indenter is added. 31

3.3 Microstructure relaxation. 32

3.4 Snapshots of dislocation patterns during the simulation at four different indenter positions l. The indenter atoms are represented by blue spheres, red spheres represent dislocated atoms in the bulk and white spheres belong to chip and groove atoms. All other atoms are represented by transparent white dots. The substrate thickness is $h = 91.5$ Å, the indentation depth is $\Delta y = 2$ Å and the scratching speed is $v = 10$ m/s. For clarity, only the dislocated atoms belonging to the two loops are represented. 36

3.5 Grazing contact: comparison between scratching work W_{sc} (solid lines) and plastic energy E_{pl} (dashed lines). Note that W_{sc} and E_{pl} share the same abscissa. The values of E_{pl} are to be read on the right ordinate, those for W_{sc} on the left one. 38

3.6 Plastic ratio as a function of scratch speed. Data is used from the last 10 nm of scratch. The boxes span from the lower to the upper quartile, the median is at the notch and the whiskers are 1.5 interquartile range long. The ratio is distinctly rate dependent for high scratch speeds. 39

3.7 Comparison between plastic energy E_{pl} and plastic count N_{pl} for a thickness $h = 366.1$ Å and an indentation depth of 1 Å (colour online). Both plots share the abscissa. The values of E_{pl} (heavy line) are to be read on the left ordinate, the ones of N_{pl} (light line) on the right ordinate. The good agreement between the two curves suggests that E_{pl} is a good measure for the energy stored in plastic zones. 40

3.8 Influence of substrate thickness on friction forces at constant scratch speed $v = 10$ m/s. 42

3.9 Influence of scratch speed on friction forces at constant substrate thickness $h = 45.8$ Å. 43

3.10 Relative evolution of plastic energy E_{pl} for different substrate thicknesses h and two different indentation depths Δy. While E_{pl} appears to increase monotonically with increasing substrate thickness for $\Delta y = 1$ Å even for large thicknesses, this is not observed for $\Delta y = 2$ Å. Both cases show size-dependence. 44
3.11 Influence of microstructure on friction forces at constant scratch speed $v = 10$ m/s. 45
3.12 Influence of the microstructure on the plastic sensitivity. 46
3.13 Localisation of plastic activity in the substrate at $v = 10$ m/s for grazing contact $\Delta y = 0$ Å. Darker means a higher relative dislocation density. Note that the contour thresholds have been chosen ad hoc for best visibility and cannot be compared between Figures 3.13a and 3.13b. 49
3.14 Partial dislocation activity in microstructure #4 during the scratch with $\Delta y = 10$ Å . Green atoms are crystalline FCC (defect-free), pink are HCP (stacking fault) and white, blue and yellow atoms part of the amorphous grain boundaries. 50

4.1 Dislocation in the vicinity of the interface: the nonlinear core region (schematically represented by the grey area) interacts with the continuum across the interface. The continuum part of the core (dark grey) is linear elastic while the atomistic part is nonlinear, leading to spurious forces. . . 54
4.2 Lost 2D simplifications 55
4.3 Dislocation passing in two dimensions. The dislocations never get close to the interface. 56
4.4 Schematic of CADD coupling using the preexisting and proven open-source codes Lammps, Akantu, and ParaDiS as plugins for the finite-element (FE), molecular dynamics (MD), and discrete dislocation dynamics (DD) domains within the coupling framework of LibMultiscale. The six distinct flows of information between the three domains are represented by the arrows. 57
4.5 Setup for coupled periodic array of straight dislocations. A domain of height $2h$, thickness b and width w is subject to periodic boundary conditions in the x and z directions. Only the slab of thickness $2h_m$ in the centre of the domain is atomistically refined. The planes marked “atomistic limit” are the coupling interfaces. 66
4.6 Initialisation of periodic geometry. The initial geometry a) has a step where the dislocation cut plane intersects the boundary. After the application of the superposed displacement fields of several periodic images of the dislocation, b), the step becomes a bump. The bump is subsequently pushed flat c) for the finite-element periodic boundary conditions to function. 68
4.7 Coupled setups for a periodic array of straight dislocations. 69

4.8 The periodic array of straight dislocations travelling. Atoms with a centrosymmetry larger than one are shown as white balls to visualise the dislocation line. All other atoms are partly transparent. In order to help understand the illustrations, the meshes and atoms are warped by the real displacement, *i.e.* the periodic displacement has been unraveled to show the step created by accumulated slips of repeated dislocation passages. . . 70
4.9 Dislocation motion: coupled system vs full molecular dynamics 71
4.10 Schematic of dislocation core in the pad. For most of the pad, the linear elastic discrete dislocation dynamics displacement solution is adequate, in the vicinity of the dislocation line, however, adding the core template $\Delta\tilde{\boldsymbol{u}}_{\mathrm{c}}$ is required to minimise spurious forces. 73
4.11 Geometric setup for core template extraction. The fat grey line represents the straight infinite dislocation line. Because the line direction $\boldsymbol{\xi}$ coincides with the z axis and the normal to the slip plane $\boldsymbol{n}$ with the y axis, the burgers vector $\boldsymbol{b}$ is constrained to be in the $x - z$ plane. The character angle of the dislocation is ϑ. 75
4.12 Extracted core of a prismatic dislocation in magnesium. 76
4.13 Simulation setup for straight hybrid dislocation. The blue squares represent regular free discrete dislocation dynamics nodes. The constrained "detected" node, represented by the red disk, is moved by the coupling scheme, not the discrete dislocation dynamics method. The interface (marked grey) is intersected at a right angle. 78
4.14 Hybrid dislocation pinning at the interface 79
4.15 Simulation of simplified hybrid dislocation 80
4.16 Schematic of coupled Frank-Read source 82
4.17 Idealised coupled Frank-Read source. Concentric dislocation loops interact across the coupling interface $\partial\Omega_{\mathrm{AC}}$, but no hybrid dislocations occur. . . . 83
4.18 Simulation setup for Frank-Read source 84
4.19 Frank-Read source fails to open correctly. Only atoms with centrosymmetry parameter $P > 1$ are shown. The blue atoms are part of dislocations emitted from the shock-loaded vacancy visible in the centre, while the white atoms depict the failing smoothly loaded loop. 85

5.1 Sharp interface coupling in CADD. The left (continuum) half of the domain is discretised using the finite-element method, the right side is treated with full atomistic resolution using molecular dynamics. The interface atoms (in the grey ellipse in Figure 5.1a) coincide with the boundary nodes of the finite-element mesh and their displacements are used as Dirichlet boundary conditions for the continuum (lower arrow in Figure 5.1b). The atoms in the pad may or may not coincide with finite-element nodes. They are moved by the finite-element method and provide the boundary conditions for the atomistic problem (upper arrow in Figure 5.1b). 89

5.2 Schematic of one-dimensional test case. 89
5.3 Evolution of temperature for $T_0^* = 0.1$ 91
5.4 Sensitivity on details at low temperatures. 92
5.5 Schematic of a small 1D CADD case. Note that the directional springs (with arrows) act only in one direction. They are responsible for the non-Newtonian mechanics of the coupled system. The interatomic spacing a and the continuum stiffness k are given, the stiffnesses k_1 and k_2 depend on a and k. 93
5.6 Comparison between linearised (green) and nonlinear (blue) coupled system. The uncoupled, full Lennard-Jones case (red) is represented as reference. Both the full Lennard-Jones system and the linearised system are stable, while the nonlinear coupled system becomes unstable around $t^* = 15000$. 96
5.7 Simplified system with asymmetric traction-compression behaviour 97
5.8 Unstable example system 100
5.9 Stability through modified dynamics. All simulations start at $T_0^* = 0.1$, consider interactions up to the second neighbour $N_{\text{neigh}} = 2$ and are discretised in time with $\Delta t = \frac{\tau_{\min}}{50}$. 102
5.10 Harmonic buffer layer coupling. The empty circles are pad atoms. Together with the grey filled circles they form the harmonic buffer layer. This layer interacts with the bulk atoms (black solid disks) through the nonlinear interatomic potential of the bulk. 103
5.11 Stability through modified coupling. All simulations start at $T_0^* = 0.1$, consider interactions up to the second neighbour $N_{\text{neigh}} = 2$ and are discretised in time with $\Delta t = \frac{\tau_{\min}}{50}$. 103
5.12 Bridging domain method. Influence of the size of the bridging zone N_{b}. Even large zones do not avoid instability. 104
5.13 Three-dimensional simulation case. Note that the finite-element mesh is fairly coarse on the left end and then gradually refined towards the pad zone, where the finite-element nodes coincide with atomic positions. . . . 105
5.14 Temperature evolution for the three-dimensional problem. The regular displacement coupling is unstable, as predicted by the one-dimensional simulations. 107

A.1 Cut through a chain with n-th neighbour interactions. Any cut severs one first neighbour spring k_1, two second neighbour springs k_2 and so on until n n-th neighbour springs k_n. At constant strain ϵ, every n-th neighbour spring is stretched or compressed by $\Delta u = n\epsilon$. 115

B.1 Temperature of the atomistic domain with lazily updated continuum. The reported tolerances are the global tolerance divided by the number of interface atoms. 118

List of Tables

2.1 Properties of iron 15

3.1 Characteristics of investigated microstructures. Microstructures with the same number of grains have been generated with different random seeds. Grain sizes are computed using the linear intercept method (Heyn, 1903; ASTM, 2010) 32

4.1 Number of degrees of freedom in domain by subdomains. 67
4.2 Comparison between full molecular dynamics and coupled performance. The sequential runs were performed on the same Intel Xeon processor. . . 86

5.1 Parameters of numerical application. The units system is irrelevant since all results are presented in dimensionless form. The time step has been chosen as $\frac{1}{3}$ of the stable time step of the linearised system. 96

1 Introduction

1.1 Motivation

The history of mankind and civilisation is closely linked to the history of tribology[1] ever since early humans around 500,000 B.C. learnt to *exploit* frictional dissipation of mechanical work to light fire by rubbing sticks together (Carnes, 2005).

The first evidence of humans learning to *reduce* friction work stems from ancient Egypt around 1880 B.C. on drawings depicting the use of sledges, wooden rollers and lubrication for the transport of large building stones (Blau, 2008). About the same time, the invention of the axle perfected the principle of the use of a rolling (rather than a sliding) motion for transport. For the following millennia, tribological advances were aimed at reducing frictional losses through the use of different animal fats or vegetable oil for lubrication and the improvement of the wheel.

Tribology ceased to be exclusively an engineering discipline in 1495, when Leonardo da Vinci performed the first scientific investigation of friction (Carnes, 2005; Blau, 2008), and formulated what were later called the two basic laws of friction:

1. Friction is independent of the apparent contact area.
2. Friction is proportional the normal load.

In 1699, Amontons (1699)[2] rediscovered these basic laws. He, and after him Coulomb (1785) and Morin (1833), (Rabinowicz, 1995) interpreted the friction force as the result of interlocking mechanical asperities. An illustration of this *roughness hypothesis* is shown in Figure 1.1. It could explain why both *static* friction is proportional to the load and independent of the apparent contact area. However, it failed to explain the origin of *kinetic* friction. The main alternative explanation — the *adhesion hypothesis* — was rejected because it implied a proportionality between friction and contact area, which was contrary to the experimental evidence.

---

[1] This account of the history of tribology concentrates mainly on *dry contact* and intentionally skips large areas of *lubricated contact* which is out of the scope of this thesis.

[2] This article has been translated in English in Amontons (1999).

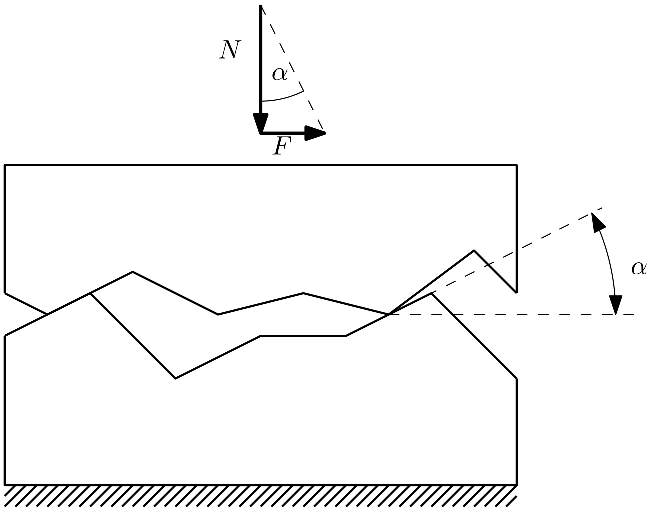

Figure 1.1 – Roughness hypothesis: The friction force F is the force necessary to push a load N over the steepest contacting asperity slope $\tan\alpha$.

The roughness hypothesis was widely accepted until advances in surface chemistry revived the adhesion hypothesis around 1920. In 1942, Bowden and Tabor (1942) introduced the important distinction between the apparent and real contact area, which allowed to explain both why friction depends on normal load and not on the apparent contact area. Additionally, the distinction makes it conceptually easier to understand the often substantial difference between the static and kinetic friction coefficients, which was first clarified by Euler (Blau, 2008). The definitive demise of the roughness hypothesis can be dated to 1955, when Bailey and Courtney-Pratt (1955) showed that atomically smooth mica surfaces have very high friction.

When the real area of contact is taken into account, friction corresponds to the shear strength of asperity contacts (Baumberger and Caroli, 2006). This represents a substantial breakthrough in the study and understanding of friction, because for the first time it links the friction force to both the geometry and the *material properties* of the contacting bodies. Although this observation helped greatly clarify the friction mechanisms and led to more and more sophisticated friction models like rate and state dependent friction coefficients accounting for ageing of asperity contact[3] (Gu et al., 1984), it is still impossible as of today to accurately compute friction coefficients *a priori*. Even the (macroscopic) concept of a friction coefficient itself becomes difficult to defend when applied to nano scale contacts (Blau, 2001).

---

[3] A good description of this development is given in Baumberger and Caroli (2006)

It has become obvious that friction and contact are *multiscale problems* involving microscopic contacts with nanoscopic friction mechanisms. The failure of macroscopic continuum approaches to explain friction (Luan and Robbins, 2005) calls for *multiscale methods* to understand friction and the associated wear and tear.

Such multiscale problems are generally intractable analytically and experiments at the nanoscale are simultaneously difficult to perform and limited in their temporal and spatial resolution. This places the most promising path to understanding nanoscale contact firmly within the third pillar of science, the domain of numerical simulation.

1.2 Objectives

This thesis is one of many in the general attempt of explaining and modelling friction and its consequences. It works towards the long term goal of predicting friction coefficients for macro scale contact between crystalline metals based on nano scale material and surface properties.

Friction is a phenomenon involving numerous processes (such as elasticity, plasticity, asperity locking, lattice vibrations and more) in a complicated interrelationship. It is known that friction dissipates energy in forms of plastic work and heat, yet the details are almost entirely unknown. Especially the role of plasticity is poorly investigated and most macro scale friction models do not include it, unless implicitly in the case of wear models (Blau, 2008; Rabinowicz, 1995). Recent molecular dynamics simulations (Luan and Robbins, 2005) however show that mechanical contact almost always involves plasticity.

In this frame, the long-term goal is to understand the nano and micro scale mechanisms involved in sliding friction. The immediate goal of this thesis is to develop the numerical tools necessary for the analysis of these mechanisms with a strong focus on coupling atomistic and continuum methods.

1.3 Challenges

As described in Section 1.1, the hypothesis that solids are continua can no longer be maintained at the scale of contacting asperities, and methods taking into account the discrete nature of solids are required. Micro scale plasticity for instance exhibits discontinuous behaviour due to dislocation activity (Hirth and Lothe, 1992; Nicola et al., 2008; Chakravarthy and Curtin, 2010) and Luan and Robbins (2005) show that even properties at the atomic (nano) scale influence the way contacting asperities behave.

As long as the study is restricted to mechanical systems at reasonable temperatures without chemical reactions (i.e., systems for which the second order Born–Oppenheimer approximation (Born and Oppenheimer, 1927) is satisfied) *classical molecular dynamics* are the largest-scale method to capture contact mechanics without loss of detail. A more detailed argumentation leading to this conclusion can be found in Berendsen (2007, Chapter 1).

Present day computing clusters are not even close to offering the necessary computational power nor memory required for modelling entire macroscopic systems in molecular dynamics. Furthermore, molecular dynamics requires integration time steps in the order of fs (femtoseconds) (Rapaport, 2004) which represents an important time scale restriction. The main challenge in this study is the development of suitable multi scale models which allow mixed descriptions of solids. These models should preserve the atomic scale resolution of molecular dynamics where needed and at the same time reduce drastically the degrees of freedom by modelling large parts with higher scale methods such as the finite element method or discrete dislocation dynamics.

1.4 Contributions to the Field of Contact Modelling in Computational Material Science

In the course of this thesis, I made three distinct contributions to modelling of contact at the atomistic scale.

Quantification of stored plastic energy in frictional contact: I developed a combined molecular dynamics and molecular statics approach to separate frictional work into heat generation and energy associated with the creation of plastic zones. The approach has been applied to a large-scale parametric nanoscratch study that investigated the effects of scratching speed, load, domain size and microstructure and we observed a significant influence of the stored plastic energy on frictional forces. The study has also shown that crystalline microstructures help shield the bulk material from wear by trapping dislocations within grain boundaries and that fine microstructures can lead to plastic energy being released instead of stored. Without shielding microstructure, however, plasticity develops over length scales that go beyond the limitations of molecular dynamics and correct treatment requires multiscale coupling methods. The results of this work are published in the *International Journal of Plasticity* (Junge and Molinari, 2014).

Stability analysis of ghost force-free displacement coupling in concurrent atomistic/continuum multiscale methods: Multiscale methods for contact were analysed because of the limitations of single scale methods and I showed that displacement coupling multiscale methods without a well-defined energy functional are dynamically unstable in general and not suited for finite temperature calculations. These restrictions appear to be poorly understood as there are numerous examples of such misuse in the literature. I propose a list of best practices to avoid the instability as well as a new ghost force-free coupling method that does not suffer from such instability issues. This work is submitted for publication and under review at the writing of this thesis.

Foundations of a three-dimensional Coupled Atomistics and Discrete Dislocations method One of the long-term goals this thesis strides for is the development of a multiscale model of contact for crystalline metals that accounts for dislocation-based plasticity. The theoretical solutions to the obstacles preventing a three-dimensional version of the method are established and the implementation of their foundations are presented here. A publication on the subject is in preparation.

1.5 Organisation

The document is organised as follows. Chapter 2 – *State of the Art* – presents previous work that is relevant to this thesis. The basic methods for continuum, mesoscale and atomistic modelling, the finite-element method, discrete dislocation dynamics and molecular dynamics, are presented only briefly as they are well established and widely used. Most of the chapter discusses pertinent coupling methods to bridge the scales from atomistics to continuum and motivates my choice to concentrate on the coupled atomistics and discrete dislocations method.

The only fully single scale chapter in this thesis is Chapter 3 – *Plastic Activity in Nanoscratch Molecular Dynamics Simulations of Pure Aluminium* – which presents in detail a novel approach to quantifying the plastic energy that is stored or released during scratching. The method is applied to in a large parametric study of single-asperity nanoscale scratching, in which I investigate how the evolution of stored plastic energy is influenced by sliding speed, simulation size, load and microstructure. I show how the stored plastic energy correlates with frictional forces.

I established the foundations for the extension of the coupled atomistics and discrete dislocations (CADD) method to three dimensions in Chapter 4 – *A Road Map Towards 3D CADD* – and discuss the challenges and strategies for future work, including a detailed road map to the full implementation of three-dimensional CADD.

Finally, in Chapter 5 – *Dynamic Stability of Ghost Force-Free Atomistic/Continuum Coupling Methods* – I show that ghost-force free displacement coupling methods are dynamically unstable in general and in practice and not suitable for finite temperature dynamics, even though they are routinely used for this exact purpose. I present a new method, that employs an adaptor layer of non-local finite elements at the interface and does not suffer from dynamic instability.

2 State of the Art

Understanding friction implies understanding the interactions of all length scales of the problem from the (macroscopic) scale of the problem structure, where the elastic reactions to frictional contact on its boundaries need to be computed, down to the atomistic scale at the tips of contacting asperities, where highly nonlinear effects nucleate dislocations and give rise to plastic deformation.

This section explains briefly the pertinent numerical tools that exist at the different length scales and provides some mechanical background where necessary, to motivate my choice of a set of tools to combine into a model that helps understand aforementioned interactions across the length-scales. The focus of this chapter lies on an overview of recent multiscale methods that allow to consider the interactions between the macro- and the microscale.

2.1 Continuum Modelling

In continuum mechanics, the length scale of the problem is considered so large that discrete phenomena (*e.g.* of atomistic or microstructural origin) can safely be neglected, *i.e.* the mechanical properties of any material point or infinitesimal volume corresponds to the average properties of its surroundings.

The equations of continuum mechanics are, in general, local *nonlinear partial differential equations*. Such equations do not usually have an analytical solution and need to be linearised and discretised in both time and space in order to obtain (approximated) linear algebraic equations which can be solved using standard linear algebra (Anton and Rorres, 2000).

The finite-element method is a well established method for the spatial discretisation of (non-)linear partial differential equations to *(non-)linear ordinary differential equations*. The resulting ordinary differential equations are linearised through iterative procedures if necessary and finally discretised in time using the finite differences method (Curnier, 2000). The main idea behind the finite-element method is the decomposition of a continuum domain into small elements for which the integral (weak) form of the governing partial differential equation is solved approximately. No detailed description of the method is given here as it is a well-known and established method. For a more exhaustive description of the FEM for fully nonlinear time-dependent problems refer to Curnier (2000); Belytschko et al. (2000) or Zienkiewicz (1986), for linear time-dependent problems to Hughes (1987) and for simple linear static problems to Gmür (2000).

The finite-element method has classically been used for contact mechanics, however Luan and Robbins (2005) showed that contact mechanics are dominated by nano scale asperities, where continuum mechanics (and therefore FEM) drastically underestimates local stresses. Furthermore, continuum mechanics usually fails to capture size effects, unless special theories such as strain-gradient plasticity (see Evans and Hutchinson, 2009) are used.

2.2 Mesoscale Modelling

I define the mesoscale as the intermediate scale at which discrete, length scale-dependent behaviour causes continuum models to fail but full atomistic resolution is not yet required. In the context crystalline metals (the focus of this thesis), the mesoscale can be thought of as the scale at which dislocations move, because plastic flow at the length scale of microns and below is dominated by the motion of individual (discrete) dislocation segments. Continuum models cannot capture such behaviour by their very nature. This section provides a brief introduction into the modelling of discrete dislocations.

2.2.1 Crystal Dislocations

Dislocations are line defects in crystal structures. The concept is best explained in the form of a thought experiment: consider a block of length l, width w and height h made of an elastic material and cut part-way through. The cut surfaces are now glued back together, but shifted with respect to one another. The magnitude and direction of the shift define the so-called *Burgers* vector $\boldsymbol{b}$. We call the edge or tip of the cut a dislocation line and its direction defines the unit vector $\boldsymbol{\xi}$. The cut plane is the dislocation's *glide plane* of normal unit vector $\boldsymbol{n}$ (omitted in Figure 2.1 for clarity) If the shift between the cut surfaces is normal to the dislocation line as in Figure 2.1a, we call it an *edge dislocation* and if the shift is parallel to the dislocation line (Figure 2.1b) we speak of a *screw dislocation*. Shifts that form an intermediate angle with the dislocation line lead to *mixed dislocations*. Volterra (1907) was the first to analyse this problem using continuum mechanics, but he did not link it to crystal plasticity yet. Note that the way I defined a dislocation line as the boundary of a cut-and-shifted internal surface implies that a dislocation can only form a closed loop or exit the body through a free boundary. It cannot end within a solid. For more details on these basics, refer to Hirth and Lothe (1992, chapters 1 and 3). In real crystalline materials, the available slip planes and Burgers vectors depend on the crystal lattice.

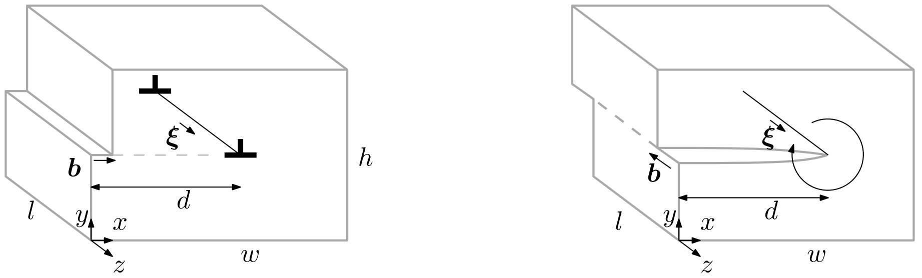

(a) Edge dislocation. The shift between the cut surfaces is normal to the dislocation line.

(b) Screw dislocation. The shift between the cut surfaces is parallel to the dislocation line.

Figure 2.1 – Simple straight dislocations

Dislocation lines can move as the crystal rearranges and by doing so, they plastically deform their surroundings. Consider the two example cases in Figure 2.1: the area behind the dislocation is shifted and therefore strained by

$$\epsilon_{xy} = \frac{b}{2h} \qquad \text{(edge), or} \qquad \epsilon_{zy} = -\frac{b}{2h} \qquad \text{(screw),} \tag{2.1}$$

where $b = ||\boldsymbol{b}||$ is the magnitude of the Burgers vector. For brevity's sake, the rest of reasoning will only be applied to the edge case. As the dislocations line advances (*i.e.* d increases), the average plastic strain $\epsilon^{\mathrm{p}}_{xy}$ can be expressed as a function of dislocation position d

$$\epsilon^{\mathrm{p}}_{xy} = \frac{b}{2h}\frac{d}{w} = \frac{bA}{2V}, \tag{2.2}$$

where $A = dl$ is the area swept by the dislocation and $V = lwh$ is the volume of the block. This result can easily be generalised to arbitrary situations, see *e.g.* Bulatov and Cai (2006),

$$\epsilon^{\mathrm{p}}_{ij}(A) = \frac{[b_i n_j + b_j n_i]A}{2V}. \tag{2.3}$$

Now that we have established that dislocations are a transport mechanism for plasticity, let us specify the driving forces behind dislocation motion. Consider the edge dislocation case and imagine the bottom surface is blocked and the top surface is subject to a traction force in x direction per unit area τ_x. Remembering that the area behind the dislocation line is shifted by b, we can write the external work W_{ext} done by τ_x as a function of A

$$W_{\mathrm{ext}} = b \cdot \tau_x A, \tag{2.4}$$

which must balance the internal work W_{int} absorbed by the dislocation motion. We define a force per unit length f acting on the dislocation line and write the work balance

$$\begin{aligned} W_{\text{int}} &= d \cdot fl = W_{\text{ext}}, \\ &\Rightarrow f = b\tau. \end{aligned} \tag{2.5}$$

This result can be generalised to obtain the Peach-Koehler formula (see, *e.g.* Hirth and Lothe (1992))

$$\boldsymbol{f} = [\boldsymbol{b} \cdot \boldsymbol{\sigma}] \times \boldsymbol{\xi}, \tag{2.6}$$

where $\boldsymbol{\sigma}$ is the local stress tensor.

The displacement and stress fields around straight dislocations in an infinite medium as well as some simple curved cases are available in the literature, *e.g.* Hirth and Lothe (1992). For a deeper introduction to the theory of crystal dislocations, refer to Weertman and Weertman (1992) or Hirth and Lothe (1992) and for a more hands-on view on the numerical aspects of dislocation description and modelling, Bulatov and Cai (2006) is a good starting point.

2.2.2 Discrete Dislocation Dynamics

We saw in the previous section that plastic deformation in crystalline materials is due to the collective motion of dislocations which have a fundamental length scale, the Burgers vector $\boldsymbol{b}$. Continuum plasticity theory (*i.e.* length scale-independent) is suitable for the treatment of length scales much larger than b, where individual dislocation segments need not be taken into account. At the micron scale however, continuum methods fail to accurately describe plastic flow because it is dominated by the motion of few individual dislocation segments and their effect can therefore not be averaged as required by continuum methods. The method of *discrete dislocation dynamics* models dislocation networks explicitly and evolves them using empirical constitutive laws. The key idea is that the discontinuous displacement fields in crystal plasticity can be computed as a superposition of the elastic response $\hat{\boldsymbol{u}}$ of the solid and the displacement field $\tilde{\boldsymbol{u}}$ of the dislocation within the solid. That way, classic linear finite elements are used to solve the elastic field, which is then in turn used to drive the dislocations accordingly.

Both simple planar (van der Giessen and Needleman, 1995) and fully three-dimensional models (Cai et al., 2004b) of discrete dislocation dynamics exist. There is a fundamental difference between the planar and the three-dimensional method: in two dimensions, dislocations are parallel to one another and form neither obstacles nor sources which then have to be modelled separately and explicitly (Nicola et al., 2007, 2008; Chakravarthy and Curtin, 2010), whereas a fully three-dimensional simulation of dislocations forms sources and obstacles on their own (Weygand et al., 2008; Bulatov et al., 2006).

The problem targeted in discrete dislocation dynamics is illustrated in Figure 2.2a. A volume Ω with boundary $\partial\Omega$ is subject to an external traction $\boldsymbol{t}_{\text{ext}}$ on a part $\partial\Omega_t$ of its boundary and an imposed displacement $\boldsymbol{u}_{\text{ext}}$ on the remainder $\partial\Omega_u = \partial\Omega \setminus \partial\Omega_t$ of the boundary. The volume contains a network of dislocations. In two-dimensional problems, the dislocation network is a set of individual straight parallel edge dislocations whereas three-dimensional networks are approximated by discretisation into segments. We consider only linear elastic material and small strains. The linearity condition allows us to use superposition, *i.e.* to write the displacement $\boldsymbol{u}$, strain $\boldsymbol{\epsilon}$ and stress field $\boldsymbol{\sigma}$ as

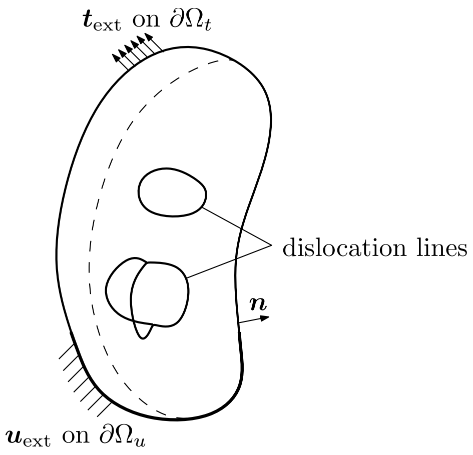
$\boldsymbol{t}_{\text{ext}}$ on $\partial\Omega_t$
dislocation lines
$\boldsymbol{n}$
$\boldsymbol{u}_{\text{ext}}$ on $\partial\Omega_u$

(a) Full initial and boundary value problem: The volume Ω contains a dislocation network. External tractions $\boldsymbol{t}_{\text{ext}}$ act on $\partial\Omega_t$ and a displacement $\boldsymbol{u}_{\text{ext}}$ is imposed on $\partial\Omega_u$.

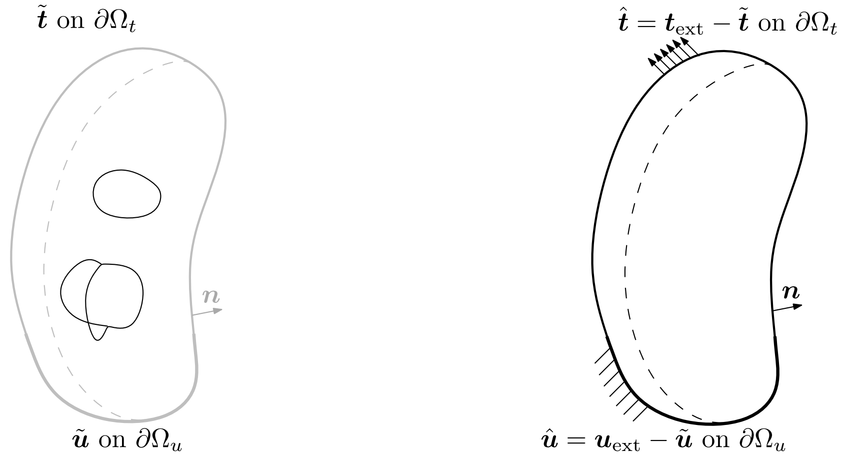
$\tilde{\boldsymbol{t}}$ on $\partial\Omega_t$
$\boldsymbol{n}$
$\tilde{\boldsymbol{u}}$ on $\partial\Omega_u$
$\hat{\boldsymbol{t}} = \boldsymbol{t}_{\text{ext}} - \tilde{\boldsymbol{t}}$ on $\partial\Omega_t$
$\boldsymbol{n}$
$\hat{\boldsymbol{u}} = \boldsymbol{u}_{\text{ext}} - \tilde{\boldsymbol{u}}$ on $\partial\Omega_u$

(b) Dislocation network in infinite space. The displacement $\tilde{\boldsymbol{u}}$ is evaluated on $\partial\Omega_u$, and the traction $\tilde{\boldsymbol{t}} = \tilde{\boldsymbol{\sigma}}\,\boldsymbol{n}$ on $\partial\Omega_t$.

(c) Boundary conditions are corrected for the elastic problem by subtracting the contributions of the dislocation network that violate the boundary conditions.

Figure 2.2 – Discrete dislocation dynamics problem, linearity is exploited to use superposition of elastic and plastic (dislocation) solution.

sums of an elastic contribution and a plastic contribution due to the dislocation network

$$\boldsymbol{u} = \hat{\boldsymbol{u}} + \tilde{\boldsymbol{u}}, \quad \boldsymbol{\epsilon} = \hat{\boldsymbol{\epsilon}} + \tilde{\boldsymbol{\epsilon}}, \quad \boldsymbol{\sigma} = \hat{\boldsymbol{\sigma}} + \tilde{\boldsymbol{\sigma}}, \tag{2.7}$$

where $(\tilde{*})$ denotes (plastic) contributions of the dislocation network and $(\hat{*})$ the elastic contribution. The fields associated with the dislocation network are the superposition of the fields $\tilde{\boldsymbol{u}}_i$, $\tilde{\boldsymbol{\epsilon}}_i$, $\tilde{\boldsymbol{\sigma}}_i$ due to all n dislocation segments,

$$\tilde{\boldsymbol{u}} = \sum_{i=1}^{n} \tilde{\boldsymbol{u}}_i, \quad \tilde{\boldsymbol{\epsilon}} = \sum_{i=1}^{n} \tilde{\boldsymbol{\epsilon}}_i, \quad \tilde{\boldsymbol{\sigma}} = \sum_{i=1}^{n} \tilde{\boldsymbol{\sigma}}_i. \tag{2.8}$$

The solid is considered infinite for the contributions of individual dislocation segments, see Figure 2.2b and the displacements $\tilde{\boldsymbol{u}}$ and traction $\tilde{\boldsymbol{t}} = \tilde{\boldsymbol{\sigma}}\,\boldsymbol{n}$ are evaluated of $\partial\Omega_u$ and $\partial\Omega_t$, respectively. These fields are then used to correct the boundary conditions for the elastic problem, see Figure 2.2c, which may be solved using any suitable method, such as for instance the finite-element method.

As to the evolution of the dislocation network, two examples of DD solvers are briefly presented here.

Needleman 2D (van der Giessen and Needleman, 1995)
Dislocation sources and obstacles are supposed to be preexisting in the solid and distributed over a grid of slip planes. Figure 2.3a shows three slip plane orientations, in the complete grid, each of the slip planes is repeated periodically throughout the crystal. If a source and an obstacle lie on the same slip plane, they can interact as depicted in Figure 2.3b. If the resolved shear stress τ on a source exceeds the nucleation stress τ_{nuc} a dipole of dislocations (two dislocations with opposite Burgers vectors) is nucleated. The position of an edge dislocation is marked with the symbol $\perp$. The nucleated dislocations then move with a velocity proportional to τ until they hit an obstacle, which they overcome if τ exceeds the obstacle strength τ_{obs}.

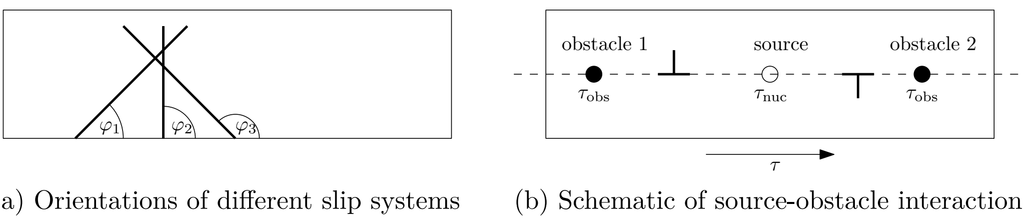

(a) Orientations of different slip systems (b) Schematic of source-obstacle interaction

Figure 2.3 – Planar discrete dislocation dynamics

Among others, this planar approach has been used successfully in contact mechanics (Nicola et al., 2008, 2007) and in the prediction of yield stress (Chakravarthy and Curtin, 2010).

Also a three dimensional version based on the Needleman method has been implemented by Weygand et al. (2008)

Cai 3D (Cai and Bulatov, 2004; Cai et al., 2004b)
A dislocation structure is discretised in linear segments as shown if Figure 2.4.

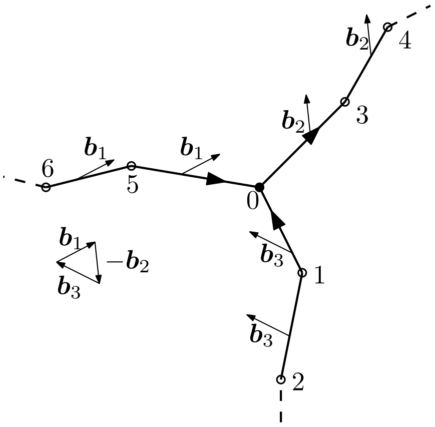

Figure 2.4 – Dislocation network represented as a set of “nodes” interconnected by straight segments. Empty circles represent simple computational discretisation nodes. The full disk (node 0) is both a computational node and a physical node, since it represents a dislocation triple-juncture. Note that two neighbouring segments have the same Burgers vector if the connecting node is a simple discretisation node. The sum of all incoming Burgers vectors matches the sum of all outgoing Burgers vectors across a node.

The self energy $E(\boldsymbol{r}_1, \boldsymbol{r}_2, \cdots)$ of such a discretised dislocation network is given by the elastic energy due to its displacement field (Cai et al., 2006). The force acting on node i is obtained by derivation,

$$\boldsymbol{f}_i = \nabla_{\boldsymbol{r}_i} E(\boldsymbol{r}_1, \boldsymbol{r}_2, \cdots, \boldsymbol{r}_n), \tag{2.9}$$

and its velocity $\boldsymbol{v}_i$ is determined according to a constitutive law. In the example of FCC metals such a law could be a linear viscous one, e.g.,

$$\boldsymbol{v}_i = B\left(\mathbf{I} - \boldsymbol{n} \otimes \boldsymbol{n}\right)\boldsymbol{f}_i, \tag{2.10}$$

where B is a drag coefficient and depends on the magnitude of the Burgers vector and $\boldsymbol{n}$ is the normal unit vector of the slip plane. Note the similarity with a MD calculation scheme. The details of this method can be found in Cai (2001)

Such fully three-dimensional DD methods are used to predict strain hardening, among others (Cai et al., 2004b; Bulatov et al., 2006; Weygand et al., 2008). A massively parallel open source implementation of this method can be found in Cai et al. (2004a).

The main drawback of DD methods is that dislocation nucleation is not yet fully understood and very important in contact mechanics (see Nicola et al., 2007). For DD to work, dislocations must be preexisting or nucleated using ad-hoc nucleation criteria. This problem can be solved by molecular dynamics (presented in the next section), where dislocations arise naturally.

2.3 Atomistic Modelling

Classical molecular dynamics is a method to simulate matter (fluid or solid) at the atomic scale by modelling point mass atoms subject to interatomic potentials. Born and Oppenheimer (1927) formulated this approximation which is well founded if the nuclei move much slower than the electrons (i.e., in mechanics at moderate temperatures without chemical reactions). In such a case, the distribution of electrons adapts in a quasi-static manner to the positions of the nuclei, and the interatomic forces (*i.e.* forces between nuclei) depend only their respective positions. It can be shown that the forces are therefore conservative and derive from a potential. The force $\boldsymbol{f}_i$ acting on any atom i of a system of N atoms is

$$\boldsymbol{f}_i = -\nabla_{\boldsymbol{r}_i} U(\boldsymbol{r}_1, \boldsymbol{r}_2, \cdots, \boldsymbol{r}_N), \tag{2.11}$$

where U is the potential energy of the system and $\boldsymbol{r}_j,\ j \in \{1, 2, \cdots, N\}$ are the atomic positions.

The equation for the evolution of a system modelled by molecular dynamics is Newton's second law

$$m_i \ddot{\boldsymbol{r}}_i = \boldsymbol{f}_i, \tag{2.12}$$

where m_i is the mass of atom i. Different (explicit) integration schemes such as Verlet and Leap-Frog are commonly used to integrate (2.12) in time, but also any classical mechanics integrator such as Newmark's corrector-predictor algorithm could be used. More details can be found in Griebel et al. (2007); Rapaport (2004); Berendsen (2007).

MD is conceptually very simple and the main difficulty in its use is the sheer size of molecular systems. As an illustration, the number N of atoms in $V = 1\ \mathrm{mm}^3$ of iron is

$$N = N_\mathrm{a} a \frac{\varrho V}{m_\mathrm{Fe}} \approx 8.5 \cdot 10^{19}, \tag{2.13}$$

where $N_\mathrm{a} = 1.6022 \cdot 10^{23}$ is Avogadro's constant, ϱ and m_Fe are the solid density and the molar mass respectively, see Table 2.1. Such a number of atoms is at least ten orders of magnitude larger than what a single computer nowadays can handle. Molecular dynamics

Table 2.1 – Properties of iron

atomic mass	$m_{\mathrm{Fe}} = 55.845$ g/mol
density at room temperature	$\varrho = 7874$ kg/m^3

relies heavily on high performance computing using parallel machines and is restricted to small simulation boxes.

Furthermore, the time steps necessary in the integration (2.12) is of the order of 1 fs $= 1 \cdot 10^{-15}$ s, which is extremely small from a contact mechanics point of view.

2.4 Multiscale Modelling

A great many methods exist in computational mechanics that deserve to be called multiscale methods. For the purpose of this thesis however, I limit the scope to concurrent partitioned-domain methods. Such methods aim at obtaining results equivalent to those of very large scale molecular dynamics simulations at a fraction of their cost by splitting the computational domain into a small, carefully determined region Ω_{A} where atomistic behaviour cannot be neglected and a region Ω_{C}, where continuum methods suffice. This geometrical partitioning makes them uniquely suitable for contact mechanics applications, where the entirety of nonlinear, discrete atomistics-dominated behaviour is concentrated around contacting asperities and the bulk of the domain exhibits behaviour consistent with the continuum mechanics hypotheses. It is then possible to use (the costly) molecular dynamics method only in Ω_{A} and to model Ω_{C} with the finite-element method, possibly in conjunction with discrete dislocation dynamics, at a much coarser scale.[1]

Several partitioned-domain multiscale methods are presented and compared here. For more comprehensive reviews and detailed comparisons, refer to *e.g.* Curtin and Miller (2003), Miller and Tadmor (2009) or Tadmor and Miller (2012). For brevity, I will subsequently refer to these methods simply as coupling methods.

Figure 2.5 illustrates the partitioning of the computational domain in a generic way. The subdomain Ω_{C} is modelled using the finite-element method while Ω_{A} is fully resolved to the atomic scale using molecular dynamics. Depending on the details of the method, the coupling is performed across a sharp interface $\partial\Omega_{\mathrm{AC}} = \partial\Omega_{\mathrm{A}} \cap \partial\Omega_{\mathrm{C}}$, or in a subdomain $\Omega_{\mathrm{I}} = \Omega_{\mathrm{A}} \cap \Omega_{\mathrm{C}}$ in which the atomistic and continuum domain overlap.

There are three major categories in which coupling methods in the literature differ from one another. [2]

---

[1] It should be noted that there are also alternative partitioned-domain methods that use coarse-grained molecular dynamics to reduce the computational cost instead of the finite-element method (e.g. Rudd and Broughton, 2005). Such methods were not pursued in this work.

[2] The topical review by Miller and Tadmor (2009) identifies four such categories of which 2) and 3)

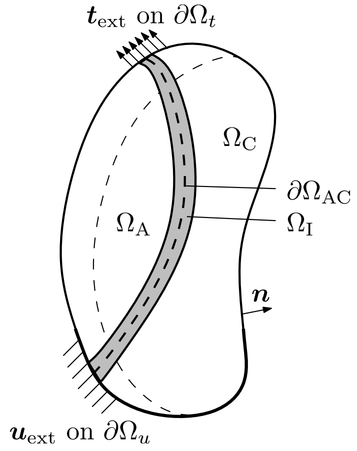
$\boldsymbol{t}_{\text{ext}}$ on $\partial\Omega_t$
Ω_{C}
$\partial\Omega_{\text{AC}}$
Ω_{A}
Ω_{I}
$\boldsymbol{n}$
$\boldsymbol{u}_{\text{ext}}$ on $\partial\Omega_u$

Figure 2.5 – Generic partitioned-domain problem. The interface between the atomistic domain Ω_{A} and the continuum domain Ω_{C} can be a sharp interface $\partial\Omega_{\text{AC}}$ or a finite coupling region Ω_{I}.

1. The governing formulation:

1. *Energy-based* methods have a single, well-defined potential energy functional $U(\boldsymbol{r})$, where $\boldsymbol{r}$ is the vector of degrees of freedom of the coupled problem. The functional can be minimised for static calculations or the forces $\boldsymbol{f}$ can be obtained by differentiation with respect to individual degrees of freedom for dynamic calculations

   $$\boldsymbol{f} = -\nabla_{\boldsymbol{r}} U(\boldsymbol{r}). \tag{2.14}$$

   Some examples of these methods are discussed subsequently; the Quasi-Continuum method and Coupling of Length Scales method (Section 2.4.1), the Bridging Domain Method (Section 2.4.2) and the Bridging Scale Method (Section 2.4.3).

2. In *displacement coupling* methods[3] the subdomains are considered as separate problems which are coupled by providing each other's Dirichlet boundary conditions ("mutual displacement boundary conditions" (Kohlhoff et al., 1991)) on the coupling interface. Among these methods, the Composite Grid Atomistic Continuum Method (Section 2.4.4), the Finite Element Combined with Atomistic Modelling method (Section 2.4.5), the Coupled Atomistics and Discrete Dislocations method (Section 2.4.6) as well as the Hybrid Simulation method (Section 2.4.7) are discussed subsequently.

Each of the two variants has their non-physical side effects which stem from the fact that we are coupling a local (continuum) domain to a non-local (atomistic) domain: the

---

together correspond to the category I call interface.

[3] Miller and Tadmor (2009) refer to these as *force-based* methods.

functional U of energy-based methods derives from an energy density that is defined in every point in Ω_C but from discrete energy contributions concentrated in atomic positions in Ω_A. It is very difficult to avoid over- or under-counting potential energy at the interface, a mismatch that leads to so-called *ghost forces* (Shenoy et al., 1999). Displacement coupling methods on the other hand do not suffer from ghost forces, but as I will show in more detail in Chapter 5 they generally exhibit asymmetric non-conservative forces across the coupling interface that violate Newton's Third Law, thus leading to severe dynamic instabilities in practice.

2. The coupling interface:

1. In *sharp interface* methods, the domain is unambiguously split, *i.e.* every degree of freedom lies in either Ω_A or Ω_C as illustrated by Figures 2.6 and 2.7. All degrees of freedom are governed by the subdomain they lie in, *i.e.* in such methods, finite-element nodes within Ω_A are slaves to the surrounding atomic displacements whereas the atoms within Ω_C move as if glued to the underlying finite-element mesh. The region in which these slave atoms lie is called the *pad* and is common to all coupling methods. A pad assures that none of the free (bulk) atoms "feels" a void on the other side of the interface. With the exception of the Bridging Domain Method (Section 2.4.2), all methods discussed in the following are sharp interface methods.

2. Other methods, however, such as the Bridging Domain Method, allow for a certain degree of mixing of the continuum and atomistic description in a *handshake region.* The manner of the mixing varies substantially from method to method. Figure 2.8 illustrates this coupling type. The pad functions the same way as for sharp interface methods.

Independently of whether a method has a sharp interface or a handshake region, a pad of slave atoms thicker than the cutoff radius of the interatomic potential is required due to the non-local nature of molecular dynamics; without the pad, some of the bulk or handshake atoms would behave as if they were close to a free boundary, leading to unphysical forces in the vicinity of the coupling interface.

Furthermore, the coupling can be enforced strongly or weakly (*e.g.* through averaging or penalty methods) in either direction (molecular dynamics to finite-element method and vice-versa). A strong enforcement of finite-element boundary conditions requires a one-to-one correspondence between interface nodes and atoms, *i.e.* the position $\boldsymbol{x}$ and displacement $\boldsymbol{u}$ of an I-th interface node must correspond to the position and displacement of an atom i,

$$\boldsymbol{u}_I(t) = \boldsymbol{u}_{i(I)}(t), \quad \boldsymbol{x}_I(t) = \boldsymbol{x}_{i(I)}(t), \tag{2.15}$$

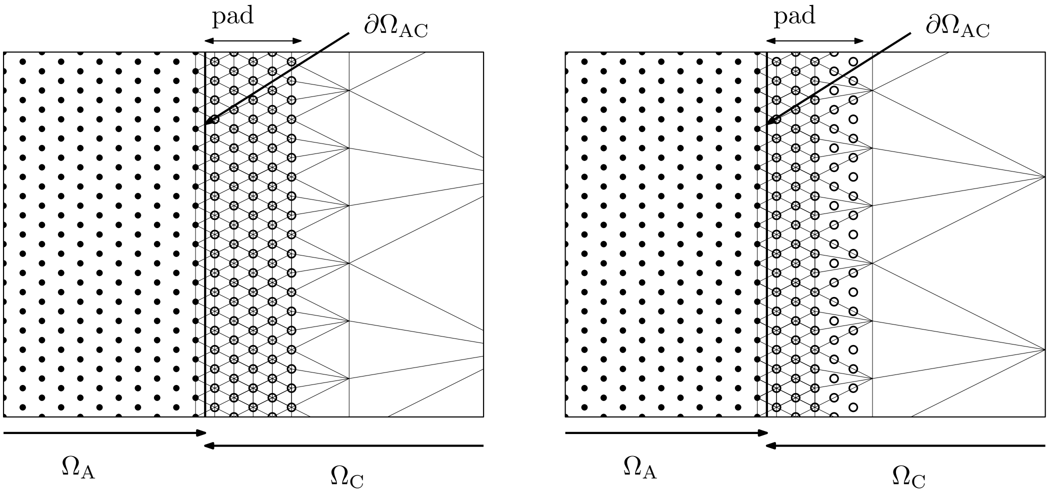

(a) Fully refined pad. This is conceptually the simplest setup for coupling molecular dynamics to the finite-element method: The mesh is refined near the interface so that pad atoms (slaves) coincide with bulk finite-element nodes (masters) and surface nodes (slaves) coincide with free atoms (masters). For instance the FEAt method (Section 2.4.5) uses this type of coupling.

(b) Coarse pad. Very similar to method shown in 2.6a. The mesh is only fully refined at the interface and the pad atoms do not necessarily coincide with finite-element nodes. As a consequence, pad nodes are slaves to elements as opposed to nodes and their displacement has to be interpolated. This has the advantage of reducing the number of elements in the mesh, but increases the interfacial stiffness. For instance the CADD (Section 2.4.6), QC and CLS (Section 2.4.1) methods use this type of coupling.

Figure 2.6 – Two-dimensional schematic for sharp interface coupling with strong compatibility. The sharp interface $\partial\Omega_{\mathrm{AC}}$ separates the domains Ω_{A} and Ω_{C} unambiguously, *i.e.* a degree of freedom is either in Ω_{A} or Ω_{C}. All atoms in Ω_{A} are free molecular dynamics atoms (solid disks) and the finite-element boundary nodes move with them. In Ω_{C}, the nodes are governed by the finite-element method and pad atoms (empty circles) behave as if glued to the underlying elements.

where t is time and the map $i(I)$ stores which atom corresponds to which interface node. Conversely, a strong enforcement of the molecular dynamics boundary conditions consists in interpolating the finite-element displacements on (pad-)atomic positions

$$\boldsymbol{u}_i(t) = \sum_{I=1}^{N_{\mathrm{nd}}} \boldsymbol{N}_I(\boldsymbol{x}_i(t_0))\, \boldsymbol{u}_I(t), \tag{2.16}$$

where N_{nd} is the number of nodes belonging to the element that contains atom i, $\boldsymbol{N}_I$ and $\boldsymbol{u}_I$ are the shape function and displacement of node I. The shape function is evaluated at the reference coordinate $\boldsymbol{x}_i(t_0)$ of pad atom i. Note that if the mesh is fully resolved to the atomistic scale (*i.e.* all pad atoms coincide with a finite-element node), (2.16)

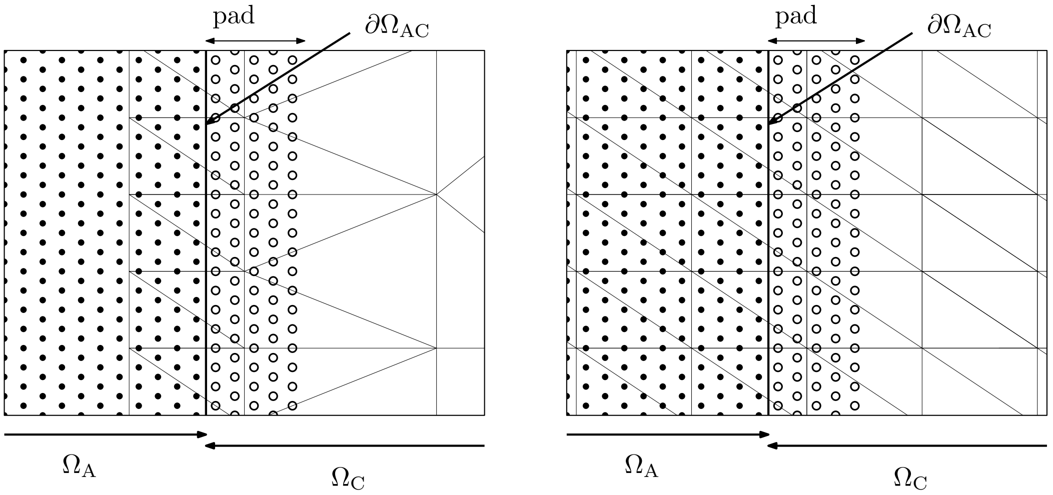

(a) The mesh is not refined at the interface but reaches into the free molecular dynamics domain Ω_{A}. Nodes within Ω_{A} follow the displacements of nearby atoms in a average sense, the details of which depend on the method in question. For instance the CACM method (Section 2.4.4) uses this type of coupling.

(b) The finite-element mesh exists everywhere. Otherwise as 2.7a. Methods such as the BSM method (Section 2.4.3) use this type of coupling.

Figure 2.7 – Two-dimensional schematic for sharp interface coupling with weak compatibility. The sharp interface $\partial\Omega_{\mathrm{AC}}$ separates the domains Ω_{A} and Ω_{C} unambiguously, *i.e.* a degree of freedom is either in Ω_{A} or Ω_{C}. All atoms in Ω_{A} are free molecular dynamics atoms (solid disks) and the finite-element boundary nodes move with them. In Ω_{C}, the nodes are governed by the finite-element method and pad atoms (empty circles) behave as if glued to the underlying elements.

simplifies to

$$\boldsymbol{u}_i(t) = \boldsymbol{u}_{I(i)}(t), \tag{2.17}$$

where the map $I(i)$ stores which pad atom corresponds to which finite-element node.

3. The treatment of the continuum:

Although all the methods mentioned here employ the finite-element method to solve the continuum problem, they vary in the level of complication of the description (small vs. finite strain), constitutive law (linear elasticity, Cauchy-Born rule (Tadmor et al., 1996)), etc.

In the following, I discuss briefly a few representative coupling methods.

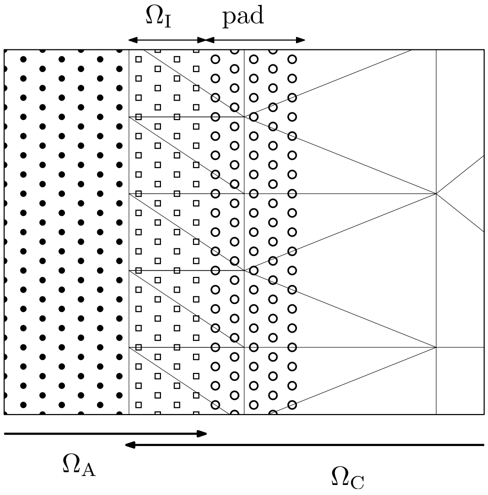

Figure 2.8 – Two-dimensional schematic of coupling interface with handshake region. The subdomains Ω_A and Ω_C overlap in the handshake region Ω_I. Fully free molecular dynamics atoms are represented by solid disks, whereas the empty disks represent pad atoms. The empty squares in are partially constrained coupling atoms in the handshake region Ω_I. For instance the BDM method (Section 2.4.2) uses this type of coupling.

2.4.1 The Quasi-Continuum (QC) and Coupling of Length Scales (CLS) Methods

The quasi-continuum method (Shenoy et al., 1998, 1999; Tadmor et al., 1996) has a sharp interface, see Figure 2.6b, and is energy-based. The continuum is modelled using finite-strain finite elements with the Cauchy-Born rule. In its original formulation, it suffers from ghost forces at the interface, however a ghost force-“corrected” version of the quasi-continuum method precomputes the ghost forces and subtracts them as dead loads from the affected degrees of freedom. These dead loads compensate the ghost forces in the configuration for which they have been computed by construction, but small second-order ghost forces reappear as the system deforms. Both static and dynamic calculations are possible. The coupling of length scales method (Abraham et al., 1998; Broughton et al., 1999; Abraham et al., 2000) is very similar to the quasi-continuum method and differs only on minor details of the drawing of the interface $\partial\Omega_{AC}$. Both methods rely on exact enforcement of the boundary conditions according to (2.16) and (2.15) and therefore on a node-to-atom correspondence between the interface nodes and the last layer of free atoms, but not necessarily on an atom-to-node correspondence between pad atoms and bulk nodes.

At least the quasi-continuum method has also been implemented as an adaptive method, where the atomistic region is allowed to grow as needed (Shenoy et al., 1999).

2.4.2 The Bridging Domain Method (BDM)

The bridging domain method (Xiao and Belytschko, 2004) is an energy-based method with a handshake region Ω_{I} in which the atomistic and continuum energies are mixed linearly. This mixing leads to a smearing of the ghost forces over the entire handshake region: the ghost force acting on any given atom in Ω_{I} is greatly reduced, however more atoms are subject to them. The coupling is enforced weakly using a Lagrange multiplier-based penalty method which introduces arbitrary (*i.e.* unphysical) penalty parameters that make it “not clear how to interpret the resulting dynamics” (Miller and Tadmor, 2009) in the handshake region.

The weak enforcement allows to drop the node-to-atom correspondence of interface nodes with free atoms. This greatly simplifies the preparation of finite-element meshes, see Figure 2.8. Miller and Tadmor (2009) mention as a drawback of the relaxation of the one-to-one node-to-atom correspondence condition that it makes it more difficult to adaptively extend the atomistic domain when needed, however Moseley et al. (2012) have successfully implemented such a dynamically evolving bridging domain method.

The bridging domain method works in both dynamics and statics.

2.4.3 The Bridging Scale Method (BSM)

The bridging scale method (Qian et al., 2004; Wagner and Liu, 2003) is an energy-based method with a sharp interface. It differs substantially from all previously mentioned methods in that the “coarse scale” (continuum region) exists everywhere in the domain *i.e.* Ω_{A} and Ω_{I} are identical and the entire domain is meshed, see Figure 2.7b. The method does not assume that the mesh is fully refined anywhere. Within the molecular dynamics region, the full solution $\boldsymbol{u}$ is decomposed into a coarse scale $\boldsymbol{u}'$ and a fine scale $\boldsymbol{u}''$

$$\boldsymbol{u} = \boldsymbol{u}' + \boldsymbol{u}'' \tag{2.18}$$

The coarse scale solution is defined by projection of the full atomistic solution onto the finite-element shape functions. This represents a weak atomistic-to-continuum coupling and constrains the finite-element nodes that lie in Ω_{A}. The finite-element solution in Ω_{C} is used to strongly enforce boundary conditions on the pad atoms.[4]

The decomposition of the solution into a coarse and a fine scale allows two different time steps to be used to integrate the motion of the (slow) coarse scale and the (fast) fine scale. The BSM works for both dynamics and statics.

---

[4] At finite-temperature, stochastic fine scale vibrations are introduced into the pad to account for fine scale effects in an averaged sense, see Wagner and Liu (2003, Section 3.1) for details.

2.4.4 The Composite Grid Atomistic Continuum Method (CACM)

The composite grid atomistic continuum method (Datta et al., 2004) is a very simple sharp interface method that uses displacement coupling. As in the bridging scale method, the entire domain is meshed coarsely as in Figure 2.7b. The boundary conditions of the atomistic domain are defined by the pad atoms which are strongly coupled to the underlying finite-element solution. The continuum boundary conditions are set by weakly enforcing nodal displacement $\boldsymbol{u}_\mathrm{C}$ within Ω_A to follow the atomistic solution $\boldsymbol{u}$ in an average sense

$$\boldsymbol{u}_{\mathrm{C},I} = \sum_i \boldsymbol{u}_i w_i(||\boldsymbol{x}_i - \boldsymbol{x}_I||), \tag{2.19}$$

where the uppercase index I designates quantities relative to the I-th node and the lowercase i relative to the i-th atom in a neighbourhood with cutoff radius R_c around the node, $\boldsymbol{x}_I$ and $\boldsymbol{x}_i$ are nodal and atomic positions in space respectively and $w(r)$ is a weighting function.[5]

The combined solution of the coupled system is calculated iteratively as follows.

- The pad atoms are set using (2.16).
- With the pad held fixed, the molecular dynamics problem is solved by minimising its potential energy U_A.
- The interface nodes are set using (2.19).
- With the interface nodes held fixed, the finite-element problem is solved by minimising its potential energy U_C.
- Repeat until converged.

The simplicity of this algorithm is its clear strength, however, the iterative approach comes at a very high computational cost if the problems are nonlinear (Miller and Tadmor, 2009). In its original description, CACM is only applicable to statics problems. It is, however, worth noting that the alternating minimisations of each subdomain's energy functional with the other subdomain's degrees of freedom blocked, make this method essentially a displacement-coupling method that could be more efficiently solved concurrently.

---

[5] In Datta et al. (2004), $w(r)$ is seemingly arbitrarily defined as

$$w(r) = \frac{1 - 3\left(\frac{r}{R_\mathrm{c}}\right)^2 + 2\left(\frac{r}{R_\mathrm{c}}\right)^3}{\sum_i 1 - 3\left(\frac{r}{R_\mathrm{c}}\right)^2 + 2\left(\frac{r}{R_\mathrm{c}}\right)^3},$$

but they mention that, in principle, any other appropriate weighting function could be used as well. If, for instance, the shape functions of the underlying finite elements were used, the continuum boundary conditions would be identical to the ones used in the bridging scales method.

2.4.5 The Finite Element Combined with Atomistic (FEAt) Modelling

The finite element/atomistics method (Kohlhoff et al., 1991) is the oldest of the methods presented here and one of the oldest atomistics/continuum coupling methods there is.[6] It is a sharp-interface displacement coupling method with strong enforcement of the coupling boundary conditions and a fully refined pad as shown in Figure 2.6a, *i.e.* every pad is slave to a bulk node and follows its displacement in time, thus serving as Dirichlet boundary conditions for the free atoms. The inverse direction works analogously, with boundary nodes following their corresponding free atoms. In the original paper on this method, Kohlhoff et al. (1991) use a nonlinear and non-local constitutive law for the finite-element description, but in principle, any other appropriate description could be used.

Kohlhoff et al. (1991) present their method as suitable for both statics and dynamics and present a limited dynamic test. In Chapter 5, however, I show that this class of methods is dynamically unstable at finite temperatures.

2.4.6 The Method of Coupled Atomistics and Discrete Dislocations (CADD)

Among the coupling methods mentioned here, coupled atomistics and discrete dislocations takes a special place because it allows mobile continuum defects such as dislocations to exist in the continuum domain and to interact elastically with the atomistic domain, even to transition freely between domains. It does this by coupling an atomistic domain to a discrete dislocation dynamics domain. This is particularly useful for the study of plasticity problems where dislocation nucleation is restricted to a small part of the computational domain. Examples of such phenomena include, but are not restricted to, fracture (nucleation of dislocations only in the vicinity of the crack tip), indentation (nucleation under the indenter) and friction (nucleation under contacting asperities) problems. Dislocation nucleation is implicitly handled in the atomistic domain and the developing dislocation network is free to grow beyond the limits of the atomistic domain[7].

The method uses a sharp interface and strong enforcement of the coupling boundary conditions as shown in Figure 2.6b, but fully refined pads as in Figure 2.6a have also been used. Originally, an energy-based formulation was proposed (see Shilkrot et al. (2002b,a)), but a revised displacement coupling version was presented in Shilkrot et al. (2004) that does not suffer from ghost forces and increased coupling interface stiffness. The molecular dynamics-to-finite-element coupling method there is identical to the FEAt method. In this document, the name CADD always refers to the revised, displacement coupling version.

---

[6] Which is probably the reason why it can use this straight-forward name.

[7] Another method, AtoDis by Brinckmann et al. (2012) has similar properties, but has not been shown to function with multiple interacting dislocations.

The atomistic domain can be treated using any type of atomistic method, such as for instance molecular statics, MD or more complex and exact methods, and the continuum domain is discretised using finite elements with discrete dislocations. Because the discrete dislocations method is based on the principle of linear superposition of the stress-strain fields due to all individual dislocation segments and the elastic solution (see Section 2.2.2), CADD is restricted to use linear elastic finite elements in the continuum. The use of discrete dislocation dynamics is also the reason why – contrary to the other methods mentioned here – CADD is difficult to extend to three dimensions. Some preliminary work on extending CADD to three dimensions is presented in Chapter 4.

The dynamic properties of CADD (and in a general sense all displacement coupling methods) are discussed in detail in Chapter 5.

2.4.7 The Hybrid Simulation Method (HSM)

Finally, the hybrid simulation method proposed by Luan et al. (2006) is a relatively recent displacement coupling method with a sharp interface[8]. The continuum-to-atomistics coupling works exactly as in CADD or FEAt, *i.e.* strong enforcement of molecular dynamics boundary conditions in the pad. In the inverse direction, a weak enforcement using (2.19) is used. This allows the use of simpler non-matching meshes as in Figure 2.7a.

2.4.8 Comparisons between the Methods

Miller and Tadmor (2009) have compared the methods presented here (and a few more) using the same numerical framework on the same static test case in terms of efficiency and accuracy of the solution (measured in displacement error). In terms of accuracy, three main results are relevant here:

1. sharp interface methods are more accurate than handshake methods,
2. strong enforcement of coupling boundary conditions leads to more accurate solutions than weak enforcement,
3. displacement-coupling methods are more accurate than energy-based methods, unless the energy-based method includes a ghost force correction (as does the ghost force corrected quasi-continuum method).

In contact mechanics problems, dislocations loops tend to nucleate under contacting asperities and travel long distances that are intractable in molecular dynamics (more on this in Chapter 3). This motivates the use of either adaptive methods, where the atomistic domain can expand as needed when dislocations travel, or coupled atomistics and discrete dislocations, where dislocations can leave the refined domain. Three of the discussed methods fit that bill: CADD (obviously), ghost force corrected QC and the dynamically evolving BDM, the last of which was not available at the beginning of this thesis.[9]

---

[8] It is sometimes erroneously categorised as a method with a handshake region, as in Miller and Tadmor (2009). While it is true that there is an overlap between the finite-element mesh and the non-pad part of the atomistic domain, the description in that overlap region is pure molecular dynamics without mixing.

Between the two remaining options, CADD and ghost force corrected QC, the big disadvantage of the QC is that the atomistic domain keeps growing as dislocations travel, which may make large problems intractable because the multiscale calculation gradually degenerates towards a full molecular dynamics calculation. On the other hand, CADD has the disadvantage that only two-dimensional implementations exist currently.

I pursued working towards a three-dimensional CADD implementation, because this method is the only one that, in principle, can handle the development of large dislocation networks at manageable cost.

It is worth mentioning that an additional disadvantage of CADD, its dynamic instability at finite temperature (more on this in Chapter 5) did not enter into the decision since it was unknown. However, since remedies that largely mitigate this problem exist (see Section 5.3) the same choice would likely have been made.

After this somewhat lengthy review of various multiscale methods, the next chapter takes a step back to atomistic modelling, exploring the challenges and limitations of the single(-nano)-scale approach to contact.

---

[9] Anyway, it would probably still not be an appropriate choice since the BDM has a) a handshake region, b) weak enforcement of coupling boundary conditions and c) suffers from ghost forces, all three of which are shown to be bad for accuracy.

3 Plastic Activity in Nanoscratch Molecular Dynamics Simulations of Pure Aluminium

This chapter is a modified version of the journal paper *Plastic activity in nanoscratch molecular dynamics simulations of pure aluminium* published in the *International Journal of Plasticity* (Junge and Molinari, 2014).

Traditionally, tribology has been the study of macroscale contact and has been dominated by experiments (Amontons, 1699; Rabinowicz, 1995; Blau, 2008). One goal of tribology is to predict friction, i.e. the friction coefficient, from material properties and contact topology. There are two main sources of challenges preventing prediction. On one hand, contact as a mechanics problem involves all length scales, from atomistics to the scale of the structure, and therefore all time scales from the period of atomistic vibrations to the duration of contact. On the other hand, it involves complex mechanisms such as third body interactions, plasticity, frictional heating and melting. At the same time, the push towards surface effect dominated micro- and nano-electromechanical systems as well as the use of atomic force microscopy (Giessibl, 2003) make it more important to understand mechanical contact at its fundamental scale, the single-asperity nanoscale contact.

Luan and Robbins (2005) showed that nanoscale contact is ruled by atomistic phenomena and virtually always accompanied by plastic deformation in the form of dislocation nucleation at the surface or asperity flattening (Luan and Robbins, 2009). These phenomena cannot be captured or understood using continuum mechanics because of their inherently discrete nature. Discrete dislocation dynamics (Bulatov and Cai, 2006) studies attempt to solve this problem by modelling the motion of individual dislocation loops but do not offer accurate treatment of dislocation nucleation, which has been shown to be an important factor (Nicola et al., 2007, 2008). On the other hand, molecular dynamics naturally handles both dislocation motion and nucleation (Bulatov and Cai, 2006; Griebel et al., 2007). There have been many molecular dynamics studies of nanoscale contact. While the early ones suffered more from the inherent length and time scale restrictions of molecular dynamics (e.g., Komanduri et al. (2000)), modern computing hardware allows for the investigation of more and more realistic contact cases (Szlufarska et al., 2008). Relevant studies include the investigation of the influence of indenter sizes and shapes (Nair et al., 2008; Gao et al., 2009; Chandross et al., 2008), of surface roughness (Spijker et al., 2011, 2012), indentation depth and third bodies (Liu and Szlufarska, 2010), surface chemistry (Mo and Szlufarska, 2010; Mo et al., 2009; Brukman et al., 2006), nano-machining (Romero et al., 2012) and surface coating (Liu et al., 2012) have been published. However, to the best of our knowledge, there has not been a systematic quantitative investigation of the degree to which the plastic mechanisms involved in friction contribute to the overall friction and how they depend on simulation parameters such as simulation box size, sliding speed and microstructure, even though plasticity in frictional contact determines wear and tear.

Non-continuum analytical models exist, but they usually involve perfect flat on flat contact and are based on the assumption that interfaces are considerably weaker than bulk material (e.g. Merkle and Marks (2007)).

We present a novel molecular dynamics based method to quantify the energies associated with the creation of plastic zones during friction. Our method is then applied to a parametric study of single asperity nanoscale scratching of a crystalline aluminium substrate. Aluminium has been chosen as an application example, but the presented method is suitable for any crystalline metal. The simulation setup and parameter space are presented in Section 3.1. Section 3.2 derives the details of the method from the molecular dynamics energy balance. The study investigates the influence of scratching speed, substrate thickness, indentation depth and microstructure. The results are presented in Section 3.3, where we also show a fundamental difference between friction mechanisms in polycrystalline and monocrystalline substrates.

3.1 Molecular Dynamics Setup

3.1.1 Single Crystal Case

The scratching simulations included in this chapter combine molecular dynamics simulations with molecular statics minimisations and have the same basic setup, shown in Figure 3.1a. The system is composed of a rigid spherical indenter and a deformable block-shaped substrate. Most of the parametric study deals with single crystal substrates. Both indenter and substrate are modelled by aluminium atoms governed by the Mendelev embedded atom model (EAM) potential (Mendelev et al., 2008) of the form

$$E_{\mathrm{pot}} = \frac{1}{2}\sum_{ij} V(r_{ij}) + \sum_{i} \Phi(\bar{\varrho}_i), \tag{3.1}$$

where $V(r_{ij})$ is a pair potential, $r_{ij} = ||\boldsymbol{r}_i - \boldsymbol{r}_j||$ is the distance between atoms i and j and Φ is the embedding energy required to insert an atom[1] into the electron density $\bar{\varrho}_i = \sum_{j \neq i} \varrho(r_{ij})$ at the position of atom i due to all other atoms. The functions V, Φ and ϱ are semi-empirical potentials.

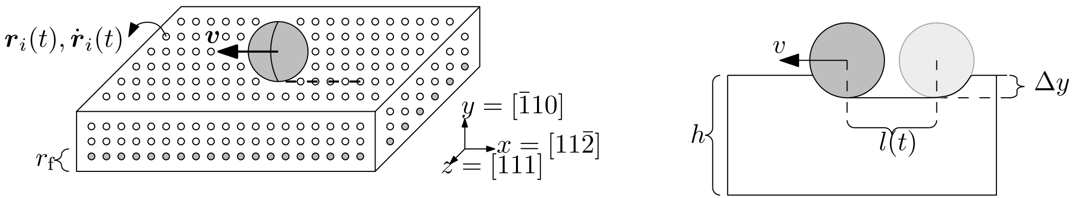

(a) Schematic simulation setup: Grey atoms in the bottom layer represent fixed atoms within r_f from the bottom boundary. The velocity vector $\boldsymbol{v}$ is imposed on all indenter atoms, $\boldsymbol{r}_i(t)$ and $\dot{\boldsymbol{r}}_i(t)$ are the position and velocity vectors of atom i. The crystal orientation of both the indenter and the substrate with respect to the coordinate system is shown in Miller indices.

(b) Schematic depiction of scratch parameters; h is the substrate thickness, Δy the indentation depth. The scratch speed v is applied by imposing the indenter position $l(t) = v\,t$ at time t.

Figure 3.1 – Simulation setup

Aluminium has a face centred cubic (FCC) lattice with a lattice constant of $a = 4.05$ Å. The substrate and the indenter are cut from the same crystal and are therefore entirely commensurate. Here, commensurability has been chosen because it provides an upper bound on friction (Hod, 2012) but later simulations on polycrystalline substrates are naturally non-commensurate. Studies of nanoscale contact with incommensurate crystals have for instance been performed by Spijker et al. (2011) and for the case of nanomachining, the influence of lattice orientation on tool-chip interface friction is studied by Romero et al. (2012).

The lattice orientation is given by the Miller indices in the figure. The boundary conditions in the x and z directions are periodic in order to avoid spurious effects due to free or rigid boundaries. This means that effectively, the simulation corresponds to a grid of asperities scratching on an infinite substrate. The atoms within a cut-off distance $r_\text{f} = 4.47$ Å of the bottom are kept fixed. The distance r_f corresponds to the cut-off distance of the Mendelev EAM potential.

Due to the crystal orientation, the lattice constants (unit cell sizes) in each direction of the (x, y, z) coordinate system are

---

[1] The published version (Junge and Molinari, 2014) erroneously states “electron” instead of the correct “atom”.

$$a_x = \left|\left[\bar{1}\bar{1}2\right]\right| = \sqrt{6}\,a = 9.91\text{ Å}, \tag{3.2}$$

$$a_y = \left|\left[\bar{1}10\right]\right| = \sqrt{2}\,a = 5.72\text{ Å}, \tag{3.3}$$

$$a_z = \left|\left[111\right]\right| = \sqrt{3}\,a = 7.01\text{ Å}. \tag{3.4}$$

Indentation and scratch directions are $[1\bar{1}0]$ and $[11\bar{2}]$, respectively. The length and width of the substrate (in x and z directions) are 64 lattices (634 Å) and 16 lattices (113 Å) while the height is varied between 4 (22.9 Å) and 64 (366.1 Å) lattices. The spherical indenter has a diameter of 46 Å.

In annealed metals, the typical dislocation density is in the range of 10^{10} to 10^{12} m^{-2}(Barnoush et al., 2010) and is typically lower close to the surface than in the bulk since free surfaces serve as dislocation sinks (Lee et al., 2009; Hirth and Lothe, 1992). The expected dislocation line length in any of the single crystals used in this study is therefore less than 1 Å. Even though preexisting dislocations has been shown to have an important effects on flow strength and plastic behaviour (Lee et al., 2009; El-Awady et al., 2013; Barnoush et al., 2010) of different metals at the scale of microns, it is reasonable at the scale of this study to assume a dislocation-free sample where plastic deformation during scratching is controlled by dislocation nucleation at the surface under the indenter where stress is concentrated Lee et al. (2009).

Starting from a cold ($T = 0$ K) system, the substrate is indented to a depth of Δy (see Figure 3.1b) in a molecular dynamics run and subsequently cooled down to 0 K in a molecular statics minimisation. The indented cold setup is the starting point for the friction analysis and its potential energy will be used as the system's reference potential energy.

For the scratch, the indenter is dragged in negative x direction at constant speed $v = ||\boldsymbol{v}||$ and indentation depth Δy. For every 1 Å of scratch path, a snapshot $\boldsymbol{R}(\bar{\tau}_j)$ of the system is saved along with the kinetic energy $E_{\text{kin}}(\bar{\tau}_j)$ and the temperature $T(\bar{\tau}_j)$, where $\bar{\tau}_j$ is the dump time step. A snapshot contains the positions $\boldsymbol{r}$ and velocities $\dot{\boldsymbol{r}}$ of each atom in the system. The force between the indenter and the substrate $\boldsymbol{F}(\tau_i)$ is evaluated at every simulation time step τ_i and its average, mean, standard deviation and 95% confidence interval is saved along with the previously mentioned quantities.

3.1.2 Polycrystal Simulations

Besides the single crystal substrate described in the previous section, we have considered four polycrystalline microstructures in order to investigate the influence of grain boundaries on friction and friction-induced plasticity.

The microstructures are based on Voronoi tessellations (Voronoï, 1908) of randomly distributed points within the substrate geometry. Each Voronoi cell is randomly assigned a lattice orientation and filled with atoms, see Figure 3.2. Atoms are coloured by grain. The Voronoi tessellation is periodic in x, y and z. The length and width of the generated polycrystalline substrates as well as the indenter are identical to the monocrystals described in the previous section.

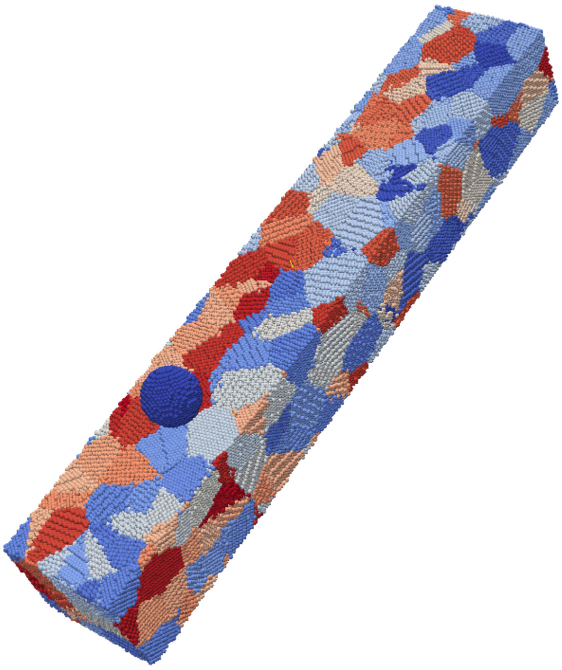

Figure 3.2 – Example of a polycrystalline microstructure. Atoms are coloured by grains which are defined by the cells of a Voronoi tessellation of 200 randomly distributed points in the substrate geometry. Each Voronoi cell is assigned a random lattice orientation and filled with atoms. The structure is heated, annealed under isostatic pressure, and quenched before the indenter is added.

A raw microstructure created this way is a very artificial construct and highly unstable because of its high energy grain boundaries with excess energies of the order of the latent heat of fusion. It needs to be relaxed before it can be used for molecular dynamics simulations. Previous molecular dynamics studies involving polycrystals propose simple heuristic relaxation procedures (e.g., Van Swygenhoven et al. (2006); Derlet and Van Swygenhoven (2003)) from which the procedure used in this study derives.

The relaxation is performed in six steps, see Figure 3.3 for an illustration. The original raw crystal is under very high pressure because some boundary atom cores are so close to each other that the EAM potential yields nonphysically high repulsive forces. An isochoric molecular statics minimisation of the potential energy (label “min 1”, solid line) relaxes these extremely high energy atoms and brings the pressure down to a few GPa and a subsequent variable volume minimisation (label “min 2”, solid line with “+” markers) relaxes the entire configuration to zero global pressure. The resulting microstructure is stable at 0 K and can be used as a starting point for molecular dynamics annealing.

Using a Nosé-Hoover thermostat and barostat (Berendsen, 2007), the system is heated up to 600 K and pressurised to 400 MPa in 1500 time steps (label “heat”, dashed line). The temperature and pressure are then maintained (label “anneal”, dotted line) while the volume of the simulation box shrinks slowly as high energy grain boundary atoms shuffle and rearrange themselves. After a few thousand time steps, the volume stops shrinking and the system is considered fully annealed. The pressure and temperature are then brought close to zero (label “quench”, dash-dotted line) using the thermostat and barostat, and a final molecular statics minimisation (label “min 3”, solid line with “x” markers) produces the fully relaxed system at 0 K and 0 Pa.

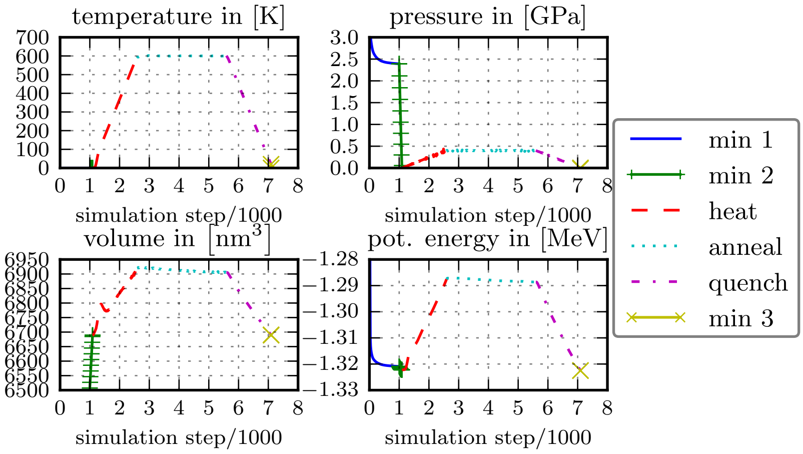

Figure 3.3 – Microstructure relaxation.

Four microstructures have been created this way with 200 or 40 grains and different random seeds. Table 3.1 lists their characteristics. The grain sizes have been computed using Heyn’s intercept method (Heyn, 1903) based on the original Voronoi tessellation. Visual inspection suggests that the annealing does not significantly change the grain sizes.

Table 3.1 – Characteristics of investigated microstructures. Microstructures with the same number of grains have been generated with different random seeds. Grain sizes are computed using the linear intercept method (Heyn, 1903; ASTM, 2010)

id	N_{grains}	mean	quartiles		
			1st	2nd	3rd
1	200	24.6 Å	21.2 Å	23.7 Å	26.9 Å
2	200	24.3 Å	20.9 Å	23.5 Å	26.6 Å
3	40	45.6 Å	37.4 Å	43.5 Å	51.6 Å
4	40	52.3 Å	42.6 Å	50.6 Å	59.3 Å

3.1.3 Parameter Space

The parametric study is split in 3 groups. All the substrates have the same x and z dimensions and the scratch paths are 30 nm long. Every scratch is performed at five different indentation depths Δy:

$$\Delta y \in \{0, 1, 2, 5, 10\}\ \text{Å},$$

where $\Delta y = 0$ is the case of grazing contact.

The first group investigates the effect of substrate thickness h. Monocrystals of thickness

$$h \in \{4, 8, 16, 32, 64\}\ \text{lattices}\ = \{22.9, 45.8, 91.5, 183.1, 366.1\}\ \text{Å},$$

are scratched at a constant scratch speed $v = 10$ m/s.

The effect of the scratching speed v is investigated in the second group. A monocrystal of thickness

$$h = 8\ \text{lattices}\ = 45.8\ \text{Å}$$

is scratched at different constant speeds v:

$$v \in \{2.5, 5, 10, 20, 40, 80, 1000\}\ \text{m/s}.$$

For the simulations at 1 km/s, only a restricted analysis has been performed, see Section 3.3.3. Finally, the third group investigates the influence of the microstructure. The four different polycrystals previously described are scratched at $v = 10$ m/s. They have a thickness $h = 91.5$ Å.

3.1.4 Simulations

All simulations are performed with LAMMPS (Plimpton, 1995) used through the multiscale modelling framework LibMultiscale (Anciaux, 2009). This combination has been chosen because LibMultiscale allows the simple implementation of constrained minimisation problems for molecular statics and simplifies the use of displacement boundary conditions in LAMMPS.

The evaluation of the chosen parameter space requires about 150 individual molecular dynamics simulations and 25 000 individual molecular statics minimisations (see next section). In order to avoid the difficulties associated with managing hundreds of thousands of input and output files, a central database server contains all the input data, starts computations, tracks their progress and gathers the output data. An incidental advantage of using a central data base is that results can be analysed in quasi–real time without having to repeatedly parse dozens of thousands of output files. The data base used in this study is PostgreSQL 8.4.8 (PostgreSQL, 2008).

3.2 Computation of Stored Plastic Energy

3.2.1 Energy Balance in Molecular Systems

The total internal energy E_{tot} present in a molecular system is given by the sum of the kinetic energy E_{kin} and the potential energy E_{pot} of the atomic cores.

$$E_{\text{tot}} = E_{\text{kin}} + E_{\text{pot}}, \tag{3.5}$$

where E_{kin} is given by

$$E_{\text{kin}} = \tfrac{1}{2} \sum_i m_i \left|\left|\dot{\boldsymbol{r}}_i\right|\right|^2, \tag{3.6}$$

m_i and $\dot{\boldsymbol{r}}_i$ being the mass and velocity vector of atom i, and E_{pot} by the semi-empirical Mendelev potential chosen to represent the atom interactions.

Any variation of E_{tot} is due to the work of external forces W_{sc}

$$\dot{E}_{\text{tot}}(t) = \dot{W}_{\text{sc}}(t) = \sum_i \boldsymbol{F}_i(t) \cdot \dot{\boldsymbol{r}}_i(t), \tag{3.7}$$

where $\boldsymbol{F}_i$ is the external force acting on atom i.

3.2.2 Evolution of Stored Plastic Energy

At absolute zero temperature $T = 0\,\text{K}$, the kinetic energy is zero as a consequence of the equipartition theorem (Hill, 1987) and the corresponding potential energy is at a local minimum. The system is said to be at equilibrium. If such a cold system is plastically deformed, i.e. quasi-statically or through low temperature deformation followed by a quenching, its equilibrium potential energy changes. The amount of the variation corresponds to the plastic energy which has been stored or released by the system during the deformation. We call this difference of equilibrium potential energy the *stored plastic energy* E_{pl}

$$E_{\text{pl}}(t) = E_{\text{pot}}^{\text{min}}(t) - E_{\text{pot}}^{\text{min}}(0). \tag{3.8}$$

A way to determine which atoms participate in plastic deformation is to compute their centrosymmetry parameter P which is zero for FCC material under homogeneous elastic deformation and nonzero for plastic deformation (Kelchner et al., 1998). Atoms in an aluminium FCC lattice for which $P > 0.5\ \text{Å}^2$ are part of a plastic event which is at least a partial dislocation and we refer to them as *dislocated atoms*. The number of dislocated atoms will later be referred to as the *plastic count* N_{pl}.

Figure 3.4 shows four snapshots taken during a scratching simulation, which clearly depict such changes in the crystal structure. Indenter atoms (blue), dislocated atoms (red) and atoms belonging to the chip and the groove (white) are represented as spheres. All other atoms are plotted as transparent white dots. We observe that there is a trail of plasticity behind the indenter, but also that the scratch causes dislocation loops to nucleate under the indenter (Figure 3.4b) and to travel into the bulk.

The system heats up during scratching and, as a consequence, both E_{kin} and E_{pot} rise. Since (3.8) relies on the system being at static equilibrium, determining E_{pl} quantitatively requires a method to split E_{pot} into a thermal and a structural component,

$$E_{\text{pot}}(t) = E_{\text{pot,therm}}(t) + E_{\text{pot,struc}}(t), \tag{3.9}$$

where $E_{\text{pot,struc}}(t)$ corresponds to $E_{\text{pot}}^{\text{min}}$ at time t.

The state of an atomic system is given by the velocities and positions of all its atoms $\boldsymbol{R}(t) = \{\dot{\boldsymbol{r}}(t), \boldsymbol{r}(t)\}$, i.e. its current position in phase space. Such snapshots $\boldsymbol{R}(t)$ of the system are taken periodically, and their equilibrium potential energies are computed by performing a molecular statics minimisation of the potential energy.

The goal of a molecular statics computation is to find the closest local minimum of $E_{\text{pot}}(\{r_i\})$ starting from a given snapshot $\{r_i\,(t)\}$[2]. A local minimum of E_{pot} is a state $\{r_i^{\text{min}}\}$ for which all atoms are at equilibrium

$$\left\{r_i^{\text{min}}\right\} = \underset{\{r_i\}|_{\text{free}}}{\operatorname{argmin}} E_{\text{pot}}\left(\{r_i\}\right), \text{ starting from } \{r_i\} = \{r_i\,(t)\}\,, \tag{3.10}$$

where $\{r_i\}|_{\text{free}}$ are the positions of the free atoms, i.e. all but the atoms in fixed boundaries. Equations (3.5) and (3.9) can be restated in incremental form,

$$\Delta E_{\text{tot}}(t) = \Delta E_{\text{kin}}(t) + \Delta E_{\text{pot}}(t), \tag{3.11}$$

$$\Delta E_{\text{pot}}(t) = \Delta E_{\text{pot,therm}} + E_{\text{pl}}, \tag{3.12}$$

where $\Delta E_{(*)}(t) = E_{(*)}(t) - E_{(*)}(0)$.

Note that the sum of ΔE_{kin} and $\Delta E_{\text{pot,therm}}$ corresponds to the heat Q which is created by the friction phenomenon. Both E_{kin} and $E_{\text{pot,therm}}$ are zero at equilibrium (0 K), therefore E_{pl} becomes

$$E_{\text{pl}}(t) = \min_{\boldsymbol{R}(t)} E_{\text{pot}}(t) - E_{\text{pot}}(0), \tag{3.13}$$

---

[2] The atomic velocities $\{\dot{r}_i\,(t)\}$ are not considered in molecular statics and set to zero.

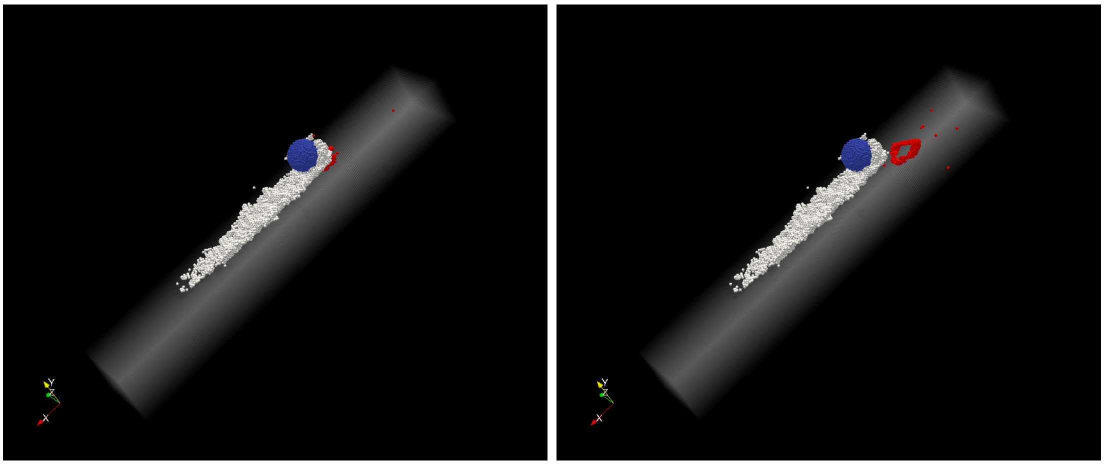

(a) Nucleation of a loop at $l = 259$ Å

(b) Loop fully formed at $l = 260$ Å

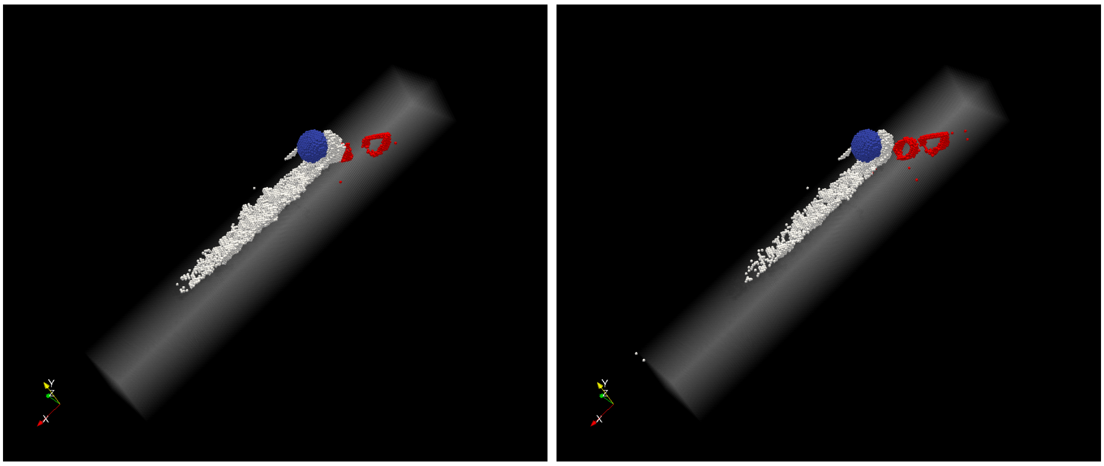

(c) Another loop nucleating, previous loop travelling into the crystal at $l = 279$ Å

(d) Dislocation pile-up at bottom of simulation box at $l = 280$ Å

Figure 3.4 – Snapshots of dislocation patterns during the simulation at four different indenter positions l. The indenter atoms are represented by blue spheres, red spheres represent dislocated atoms in the bulk and white spheres belong to chip and groove atoms. All other atoms are represented by transparent white dots. The substrate thickness is $h = 91.5$ Å, the indentation depth is $\Delta y = 2$ Å and the scratching speed is $v = 10$ m/s. For clarity, only the dislocated atoms belonging to the two loops are represented.

where $E_{\mathrm{pot}}(0)$ is the potential energy of the cold indented system before the start of the molecular dynamics scratch. Equation (3.8) is valid if the used minimisation algorithm finds the closest local minimum, i.e. that it does not modify any plastic phenomena. We used a conjugate gradient (CG) method and a visual inspection of the dislocation patterns, such as those shown in Figure 3.4 before and after minimisation, suggested that this condition is satisfied by CG at the temperatures reached during the simulations in this study (typically less than 100 K). If the plastic deformation happens at high temperatures, especially if strong temperature gradients are present, this definition of E_{pl} (3.8) is no longer applicable, because thermal expansion during the temperature changes can itself introduce plastic deformations, especially close to the bottom, where the fixed boundary atom layers cannot expand thermally.

3.3 Simulation Results

3.3.1 Work and Plasticity

Figure 3.5a compares the evolution of the scratching work W_{sc} to the evolution of E_{pl} for three different substrate thicknesses h at a scratching speed $v = 10$ m/s for grazing contact $\Delta y = 0$. Deeper indentation depths yield similar evolutions with higher energies involved. We can see that both W_{sc} and E_{pl} rise essentially monotonically (save for high frequency fluctuations) with increasing scratch distance. Most importantly, we see a significant size effect; W_{sc} is significantly higher for the two thicker substrates than for the thin one. The same cannot be said for E_{pl}; for most of the scratch, fluctuations are so strong that they make it difficult to see any size effect, and only after about 20 nm of scratch, it appears that the thicker substrates have a consistently higher E_{pl} than the 22.9 Å substrate. These complicated size effects are not yet understood. Note that E_{pl} is a non-negligible proportion of the total scratching work contributing to roughly one tenth of the energy increase at this speed. The difference between W_{sc} and E_{pl} is the heat generated by the scratch. Figure 3.5b shows similar plots for which $h = 45.8$ Å has been kept constant and the scratching speed is varied. We observe a rate dependence for W_{sc} at higher scratch speeds, while E_{pl} appears to be rate dependent over the entire range of speeds. Note that the rate dependence of W_{sc} and E_{pl} are of opposite sign: W_{sc} increases while E_{pl} decreases with scratch speed. It appears that the stored plastic energy strongly depends on the amount of time plastic activity has to develop. Overall, for the range of speeds and sizes covered in this study, both E_{pl} and W_{sc} are size and rate dependent.

One can discern a transient regime in the first 10 to 15 nm in which W_{sc} grows like a parabola, followed by what appears to be a permanent regime in which W_{sc} grows linearly. This effect can be explained by the developing plastic zone under the indenter: early dislocations can easily travel into the still perfect crystal (see Figure 3.4b) while later dislocations tend to pile-up against the fixed bottom layers of the crystal (see Figure 3.4d)

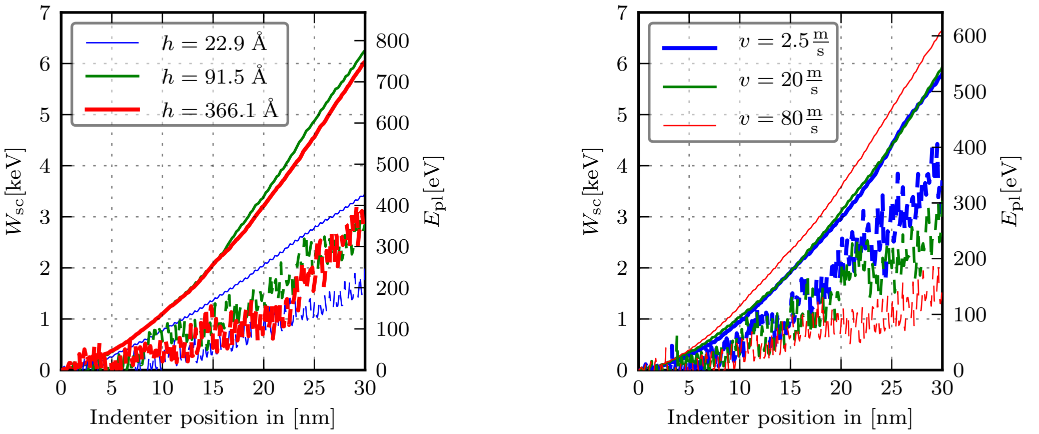

(a) $v = 10$ m/s for different substrate thicknesses h. Heavier lines stand for thicker substrates. Solid and dashed lines show the scratch work W_{sc} and the plastic energy E_{pl}, respectively. Note the size dependence of both W_{sc} and E_{pl}.

(b) $h = 45.8$ Å for different scratch speeds. Solid and dashed lines show the scratch work W_{sc} and the plastic energy E_{pl}, respectively. Note the rate dependence of both W_{sc} and E_{pl} and that they are of opposite effect.

Figure 3.5 – Grazing contact: comparison between scratching work W_{sc} (solid lines) and plastic energy E_{pl} (dashed lines). Note that W_{sc} and E_{pl} share the same abscissa. The values of E_{pl} are to be read on the right ordinate, those for W_{sc} on the left one.

and harden it, hence the increasing slope of W_{sc} during the transient regime[3]. Once the pile-up is reached, the plastic zone cannot keep growing and a permanent regime is reached. The size effect we observe is a reflection of the inability of the plastic zone to develop fully.

By defining the plastic ratio η as

$$\eta(t) = \frac{E_{\mathrm{pl}}(t)}{W_{\mathrm{sc}}(t)}, \tag{3.14}$$

the rate dependence of E_{pl} is conveniently visualised. Figure 3.6 shows η as a function of v for grazing contact, compare Figure 3.5b. In order to avoid transient effects, η has been evaluated for the last 10 nm of each scratch. The previously observed rate dependence appears to apply for high scratch speeds with a transition between 5 to 10 m/s.

---

[3] Note in Figures 3.4a and 3.4b that after nucleation, dislocations move much faster than the indenter: while the indenter moved by 1 Å, the dislocation advanced by about 1 indenter diameter (46 Å). This means that once dislocations are being nucleated, pile-up happens practically instantaneously.

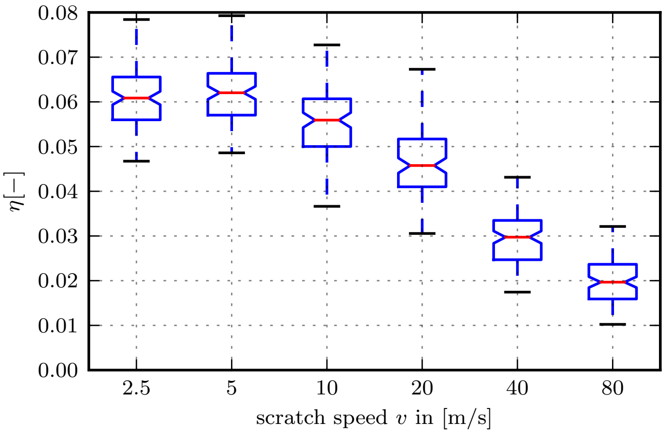

Figure 3.6 – Plastic ratio as a function of scratch speed. Data is used from the last 10 nm of scratch. The boxes span from the lower to the upper quartile, the median is at the notch and the whiskers are 1.5 interquartile range long. The ratio is distinctly rate dependent for high scratch speeds.

3.3.2 Plasticity and Dislocation Activity

Figure 3.7 shows a comparison between E_{pl} and the number of dislocated atoms N_{pl} for $h = 366.1$ Å and an indentation depth $\Delta y = 1$ Å. Atoms are counted as dislocated if their centrosymmetry factor $P > 0.5$ Å^2. Note that the two plots share the same abscissa, but have different ordinates on either side of the graph.

The idea to use a count of plastic events to quantify plasticity is not new, e.g., Luan (2006) defined plasticity as a change of nearest neighbours and Hoy and Robbins (2007) used a strain-based criterion. More complex analysis methods such as the common neighbour analysis (CNA) (Honeycutt and Andersen, 1987) or maximum relative displacements (Brandl et al., 2011) based on the slip vector proposed by Zimmerman et al. (2001) could offer a more detailed analysis of plasticity, but here only a global quantification rather than a detailed distribution of plasticity is necessary.

One can observe that E_{pl} is slightly smoother than N_{pl} and has less extreme spikes. This is not surprising since E_{pl} computes a continuous result of a global measure, whereas the count of dislocated atoms is based on categorical data; either the centrosymmetry parameter P is above threshold or not and a nucleating loop pushes numerous atoms over this threshold in a short amount of time. However, the excellent fit between the two plots is evident and shows that E_{pl} is indeed a satisfactory quantitative measure for the energy stored in plastic zones.

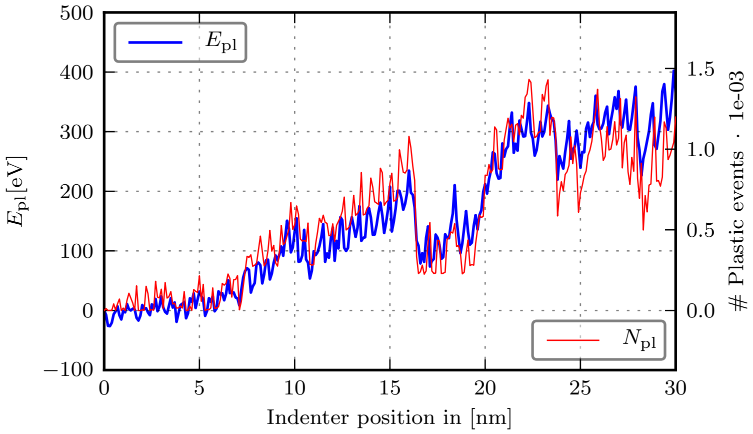

Figure 3.7 – Comparison between plastic energy E_{pl} and plastic count N_{pl} for a thickness $h = 366.1$ Å and an indentation depth of 1 Å (colour online). Both plots share the abscissa. The values of E_{pl} (heavy line) are to be read on the left ordinate, the ones of N_{pl} (light line) on the right ordinate. The good agreement between the two curves suggests that E_{pl} is a good measure for the energy stored in plastic zones.

3.3.3 Friction Coefficient

The most common characterisation of friction is through the friction coefficient μ defined as (Blau, 2001)

$$\mu \equiv \frac{\mathrm{d}F}{\mathrm{d}L}, \tag{3.15}$$

where F is the friction force in the scratching direction and L is the normal force. The definition is based on the assumption that F is an affine function of L of the form

$$F = F_{\mathrm{a}} + \mu\, L, \tag{3.16}$$

where F_{a} is an adhesion force which depends on the contact area and the friction coefficient μ is a parameter describing the interaction between the indenter and substrate.

The friction coefficient is a macroscale concept and requires some adaptation in order to be meaningful at the nanoscale; the forces $F(t)$ and $L(t)$ are window-averaged

$$\langle F \rangle_i = \tfrac{1}{N_{\mathrm{w}}} \textstyle\sum_j^{N_{\mathrm{w}}} F(t_{i+j}), \tag{3.17}$$

$$\langle L \rangle_i = \tfrac{1}{N_{\mathrm{w}}} \textstyle\sum_j^{N_{\mathrm{w}}} L(t_{i+j}), \tag{3.18}$$

$$i \in \{0, 1, 2, \cdots, N - N_{\mathrm{w}}\},$$

where the window size N_w is given by

$$N_\mathrm{w} = \frac{a_x}{v\,\Delta t}, \tag{3.19}$$

where a_x is one lattice distance in the scratching direction, see (3.2), for the crystal orientation of the indenter, and Δt is the simulation time step. The window size corresponds to the number of time steps it takes the indenter to move over one periodic unit cell of length a_x of the substrate crystal. The ceiling function $\lceil * \rceil$ is used to round N_w up to the next integer value. This way, each window-averaged data point represents forces clean from fluctuations of higher frequencies than those which are crystallographically explicable.

Size dependence Figure 3.8a shows $\langle F \rangle$ as a function of the substrate thickness h. Each plotted data point represents a window-averaged force measurement cluster for an entire scratch simulation and the error crosses show their standard deviations which are used as confidence intervals. One cluster has been computed for each scratch case in the parameter space

$$\begin{aligned}\mathbb{P}_h &= \{h\} \times \{\Delta y\},\\ \{h\} &= \{22.9, 45.8, 91.5, 183.1, 366.1\}\ \text{Å},\\ \{\Delta y\} &= \{0, 1, 2, 5, 10\}\ \text{Å},\end{aligned}$$

at a scratch speed $v = 10$ m/s. The straight lines are obtained from least-squares linear approximations for clusters of equal substrate thickness and their slope is the friction coefficient μ, see Definition (3.15). It can be clearly seen that the linear approximations intersect all the confidence intervals of their corresponding clusters. Except for the thinnest substrate (red circles in Figure 3.8), the friction coefficients are statistically indistinguishable at about $\mu \approx 1.75$. At a first glance, this suggest that the friction coefficient is size independent for thick substrates (in this case, substrates for which $h \geq 45.8$ Å). In other words, μ exhibits a size dependence only in the thin substrate case when the indentation depth is in the order of a quarter of the substrate thickness. The size dependence may be linked to the fact that there is not enough space for plastic zones to develop in the thin substrate. This explanation is supported in the next paragraph in the case of very high scratching speeds.

Rate dependence Figure 3.9a shows the result of the same analysis with varying scratch speed v. The speeds 2.5, 10 and 40 m/s are not shown in Figure 3.9a for clarity but do not differ substantially from the rest.

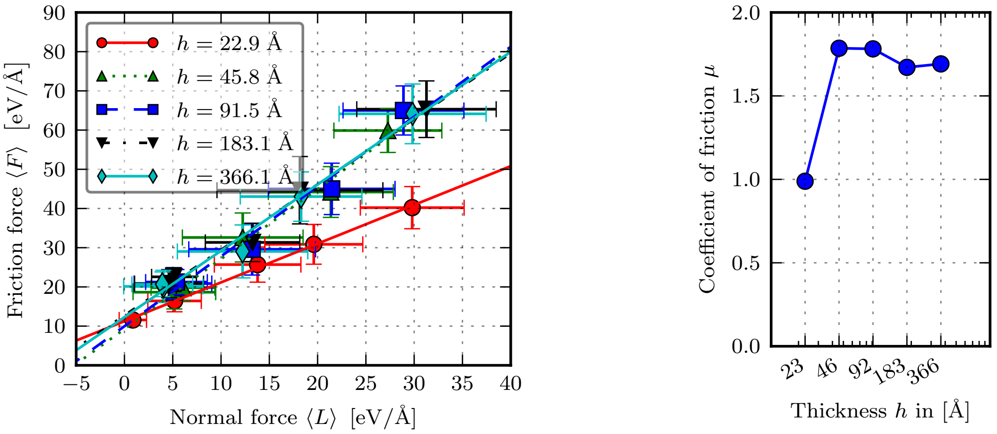

(a) Each data point represents averaged force measurements for a scratch simulation at a given indentation depth. Error crosses indicate the standard deviation of these measurements in both F and L. The straight lines represent linear least-square approximations to data points of equal thickness h.

(b) Friction coefficient μ as a function of the substrate thickness h. The measure for the coefficient of friction appears to stabilise above $h = 45.8$ Å.

Figure 3.8 – Influence of substrate thickness on friction forces at constant scratch speed $v = 10$ m/s.

One cluster has been computed for each scratch case in the parameter space $\mathbb{P}_v$

$$\begin{aligned} \mathbb{P}_v &= \{v\} \times \{\Delta y\}, \\ \{v\} &= \{2.5, 5, 10, 20, 40, 80, 500, 1000, 2000\} \text{ m/s}, \\ \{\Delta y\} &= \{0, 1, 2, 5, 10\} \text{ Å}, \end{aligned}$$

for $h = 45.8$ Å. One can see that all linear approximations intersect the confidence intervals of their corresponding clusters. We conclude that there is indeed an affine relationship between $\langle F \rangle$ and $\langle L \rangle$. Even though the friction coefficient is not strongly rate dependent at speeds between 2.5 and 80 m/s the friction coefficient seems to follow a bell curve with a transition from velocity-increasing to velocity-decreasing behaviour at about 20 m/s. At very high speeds of $v \geq 0.5$ km/s, the friction coefficient is significantly lower and appears to have reached a plateau. The dependence of E_{pl} on the scratching speed, see Figure 3.6, suggests that at very high scratch speeds, the plastic zones have insufficient time to develop. We observe that suppressing bulk plasticity by either scratching at very high speed or on a very thin substrate (Figure 3.8b leads to very similar friction coefficients of about unity. It appears that even though E_{pl} is only a small proportion of W_{sc}, the two seem strongly linked when the development of plastic zones is suppressed.

Macroscale measurements of steel on steel friction performed by Philippon et al. (2004) show the same bell-shaped behaviour with a trailing plateau. They attribute the decay

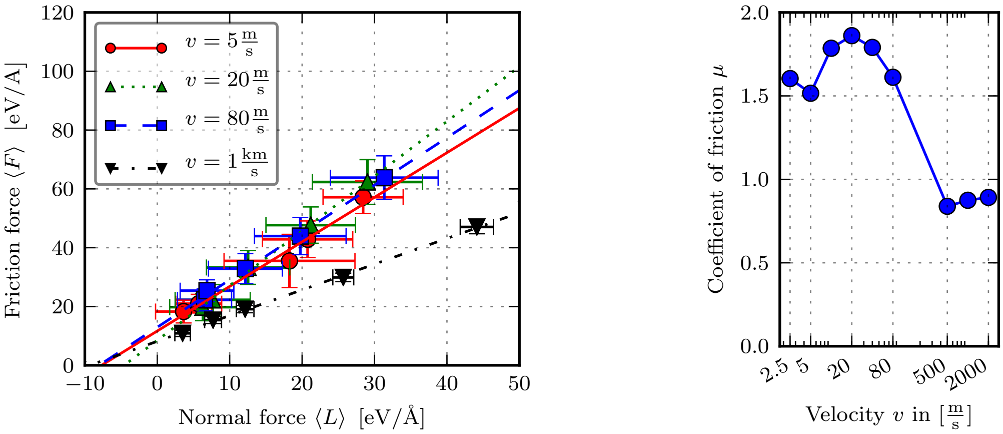

(a) Each data point represents averaged force measurements for a scratch simulation at a given indentation depth. Error crosses indicate the standard deviation of these measurements in both F and L. The straight lines represent linear least-square approximations to data points of equal scratch speed v.

(b) Friction coefficient μ as a function of the scratch speed v.

Figure 3.9 – Influence of scratch speed on friction forces at constant substrate thickness $h = 45.8$ Å.

of μ at high speed to thermal effects. The high temperatures at the interface soften the material locally, see Molinari et al. (1999), and lead to only a thin boundary layer being affected.

In their molecular dynamics study of nanoscale machining of copper, Romero et al. (2012) find very similar curves for the tool-chip interface friction and they analyse the chip interface temperature. The study confirms the link between increased interface temperature and lowered friction in a system that is very close to the one studied here.

A more detailed investigation of the thermal effects in nano-machining (Romero et al., 2013) shows uniform temperature gradients for sliding velocities below the peak of the bell, which corresponds to $v < 20$ m/s in the present case and suggests that the drop of friction with an eventual plateau coincides with the creation of a thermal boundary layer close to the friction interface at higher speeds.

Figure 3.10 compares the relative evolution of plastic energy E_{pl} as a function of the thickness h for two different indentation depths. For both indentation depths, the evolution of E_{pl} overall rises with increasing substrate thickness and this trend is monotonic for the shallow indentation. For the deeper indentation depth however the trend is non-monotonic, indicating once more that the simulation domain was not large enough to allow the plastic zones to fully develop. While the friction coefficient μ (and therefore the involved scratching work W_{sc}) seems to stabilise for large h, the plastic energy E_{pl}

reveals that the underlying mechanisms and plastic effects are still size-sensitive and that sufficiently large simulation boxes have *not* been reached.

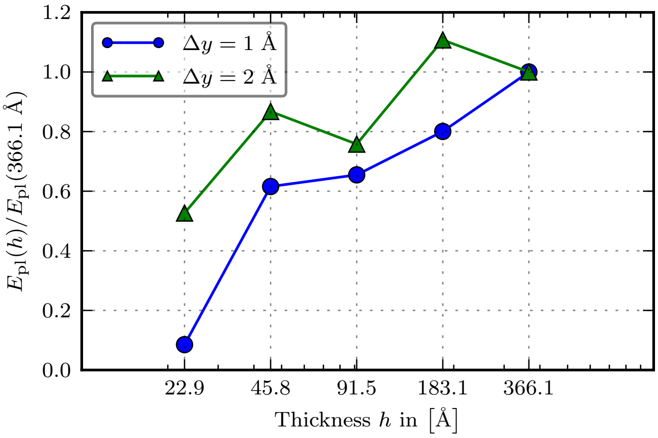

Figure 3.10 – Relative evolution of plastic energy E_{pl} for different substrate thicknesses h and two different indentation depths Δy. While E_{pl} appears to increase monotonically with increasing substrate thickness for $\Delta y = 1$ Å even for large thicknesses, this is not observed for $\Delta y = 2$ Å. Both cases show size-dependence.

Note also that a) the scratch speeds v in the simulations are quite high and that the heat production Q during scratching decreases or stabilises with decreasing v, and b) that our results suggest that E_{pl} *increases* with decreasing v (see Figure 3.5b). This entails that E_{pl} becomes a more important and determining quantity at lower v.

3.3.4 Influence of the Microstructure

Figure 3.11a shows the friction coefficient comparison for different microstructures at scratching speed $v = 10$ m/s and substrate thickness $h = 91.5$ Å. The explored parameter space $\mathbb{P}_{\mathrm{M}}$ is defined by

$$\begin{aligned}\mathbb{P}_{\mathrm{M}} &= \{\mathrm{M}\} \times \{\Delta y\},\\ \{\Delta y\} &= \{0, 1, 2, 5, 10\}\ \text{Å},\end{aligned}$$

where $\{\mathrm{M}\}$ is the set of microstructures composed of the polycrystals described in Section 3.1.2 and the single crystal of thickness $h = 91.5$ Å. One can see that the affine relationship between $\langle F \rangle$ and $\langle L \rangle$ is valid for the polycrystals as every linear approximation intersects the confidence intervals of all the corresponding clusters.

The friction coefficients vary substantially between polycrystals, even for the structures with practically the same mean grain size, 24.3 Å and 24.6 Å, see Figure 3.11b. These differences between polycrystals are explained by the random nature of the microstruc-

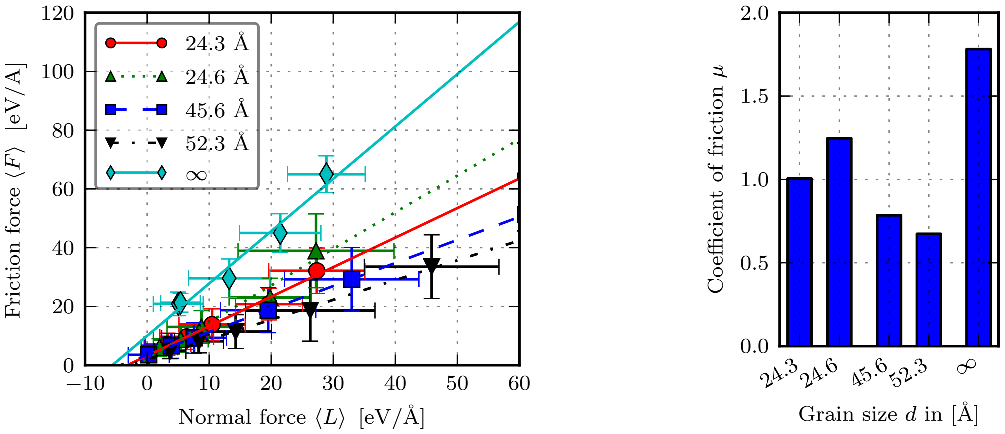

(a) Each data point represents averaged force measurements for a scratch simulation at a given indentation depth. Error crosses indicate the standard deviation of these measurements in both F and L. The straight lines represent linear least-square approximations to data points computed for the same microstructure.

(b) Friction coefficient μ for different polycrystals and a monocrystal. Polycrystals have a consistently lower friction coefficient than the commensurate monocrystal.

Figure 3.11 – Influence of microstructure on friction forces at constant scratch speed $v = 10$ m/s.

tures: the indenter scratches over a limited number of grains over the scratch path length of 30 Å so that effects due to grain boundaries and different lattice orientations do not average out between microstructures.

The most obvious qualitative difference between the single crystal case and all the polycrystal cases, however, is that the friction coefficients computed for the polycrystal is consistently lower than for the commensurate monocrystal scratched in $[11\bar{2}]$ direction. This difference is due to a fundamentally different evolution of plastic energy between polycrystals and monocrystals. Figure 3.12a shows this evolution $E_{\text{pl}}(x) = \Delta E_{\text{min}}(x)$ for a scratching depth $\Delta y = 2$ Å for the polycrystal with a mean grain size of 45.6 Å and compares it to the monocrystal. Note that, in the case of the monocrystal, E_{pl} overall increases during the scratching, while it *decreases* in the case of the polycrystal. The phenomenon is plotted for only two cases, however we observe it for all microstructures and indentation depths.

This implies that the local frictional heating due to the scratching excites grain boundaries more than the annealing of the microstructure described in Section 3.1.2 did and allows some of them to relax: some of the high energy stored in the grain boundaries gets *released* as heat as portions of the microstructure recrystallise, thus causing E_{pl} to decrease. Sansoz and Dupont (2006) and Tucker and Foiles (2013) observed similar microstructure coarsening in nanocrystalline indentation.

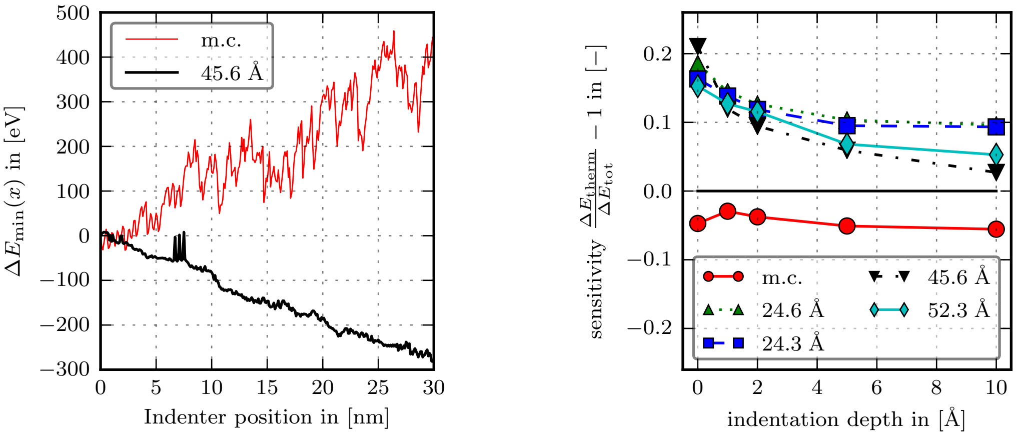

(a) Comparison of plastic energy evolution for a monocrystal (m.c.) and a polycrystal (45.6 Å). Both substrates have a thickness of $h = 95.5$ Å and are indented to a depth of $\Delta y = 2$ Å and scratched at a speed of $v = 10$ m/s. The polycrystal has a mean grain size of 45.6 Å. Note that the monocrystal accumulates plastic energy during the scratch while the polycrystal releases it.

(b) Influence of the microstructure on the plastic sensitivity. The straight solid black line is the low temperature threshold below which the scratched substrate stores plastic energy and above which it releases it.

Figure 3.12 – Influence of the microstructure on the plastic sensitivity.

A way to visualise this is to analyse the creation of heat and to compare it to the increase of total energy of the system during scratching. Absent plastic phenomena, a molecular dynamics system behaves like a system of coupled oscillators. At low temperatures, it can safely be approximated by a coupled system of harmonic oscillators (McQuarrie, 1975),

$$\mathbf{M}\ddot{\boldsymbol{x}}(t) + \mathbf{K}\boldsymbol{x}(t) = \boldsymbol{f}(t), \tag{3.20}$$

where $\mathbf{M}$ and $\mathbf{K}$ are the mass and stiffness matrix of the system, $\boldsymbol{f}$ a vector of external forces which we will neglect from now on and $\boldsymbol{x}$ is the vector of the degrees of freedom of the atoms. The potential and kinetic energy are given by

$$E_{\text{pot}}(t) = \tfrac{1}{2}\boldsymbol{x}(t)^{\mathrm{T}}\,\mathbf{K}\,\boldsymbol{x}(t) \tag{3.21}$$

$$E_{\text{kin}}(t) = \tfrac{1}{2}\dot{\boldsymbol{x}}(t)^{\mathrm{T}}\,\mathbf{M}\,\dot{\boldsymbol{x}}(t) \tag{3.22}$$

Such a system can be represented as a decoupled system of harmonic oscillators for which

$$\boldsymbol{x} = \mathbf{B}\,\boldsymbol{q}, \tag{3.23}$$

$$q_i(t) = A_i \cos(\omega_i t + \phi_i), \tag{3.24}$$

where $\mathbf{B}$ is the matrix formed of the eigenvectors of $\mathbf{M}^{-1}\mathbf{K}$, A_i, ω_i and ϕ_i are the amplitude, angular velocity and phase shift of the i-th eigenmode, see e.g., Del Pedro and Pahud (2003) for more details. As $\mathbf{B}$ diagonalises both $\mathbf{K}$ and $\mathbf{M}$, the expressions for E_pot and E_kin become

$$E_\text{pot}(t) = \tfrac{1}{2}\boldsymbol{q}(t)^\text{T}\ \underbrace{\mathbf{B}^\text{T}\mathbf{K}\mathbf{B}}_{\text{diagonal}}\ \boldsymbol{q}(t) = \frac{1}{2}\sum_{i=1}^{N} k_i A_i^2 \cos^2(\omega_i t + \phi_i), \tag{3.25}$$

$$E_\text{kin}(t) = \tfrac{1}{2}\dot{\boldsymbol{q}}(t)^\text{T}\ \underbrace{\mathbf{B}^\text{T}\mathbf{M}\mathbf{B}}_{\text{diagonal}}\ \dot{\boldsymbol{q}}(t) = \frac{1}{2}\sum_{i=1}^{N} \underbrace{m_i\omega_i^2}_{=k_i} A_i^2 \sin^2(\omega_i t + \phi_i). \tag{3.26}$$

The structural potential energy $E_\text{pot,struc}$, see (3.9), is the constant part of E_pot, i.e., its eigenmode for which $\omega = 0$. The sum of all fluctuating energies, i.e., the sum of E_pot and E_kin due to all eigenmodes with nonzero angular velocities, is the heat Q [4]

$$Q = \tfrac{1}{2} \sum_{i=1,\omega_i\neq 0}^{N} k_i A_i^2 \left(\cos^2(\omega_i t + \phi_i) + \sin^2(\omega_i t + \phi_i)\right) = \tfrac{1}{2} \sum_{i=1,\omega_i\neq 0}^{N} k_i A_i^2. \tag{3.27}$$

Therefore, on average over time, $\langle E_\text{kin}\rangle$ is half of Q

$$\begin{aligned}\langle E_\text{kin}\rangle &= \left\langle \tfrac{1}{2}\sum_{i=1}^{N} k_i A_i^2 \sin^2(\omega_i t + \phi_i)\right\rangle = \tfrac{1}{2}\sum_{i=1}^{N} k_i A_i^2 \left\langle \sin^2(\omega_i t + \phi_i)\right\rangle \\ &= \tfrac{1}{4}\sum_{i=1}^{N} k_i A_i^2 = \tfrac{1}{2}Q,\end{aligned} \tag{3.28}$$

In the case of the scratching simulations of this study, most of the substrate is at low temperature, where this approximation applies. We can therefore express the heat as

$$Q \approx 2\,E_\text{kin}. \tag{3.29}$$

Locally, at the frictional interface and in the vicinity of moving dislocations, plastic phenomena introduce variations of potential energy not associated with heat as they introduce potentially permanent changes to the crystal structure. This allows the definition of a *thermal sensitivity* s

$$s = \frac{\Delta Q}{\Delta E_\text{tot}} - 1, \tag{3.30}$$

which is the ratio between the variation of heat and total energy. Figure 3.12b shows a plot of s during scratching for all considered indentation depths and microstructures. Absent plasticity, the sensitivity would be $s \approx 0$ as most of the crystal is at low temperature.

---

[4] This separation assumes that the energy in long wavelength modes (mechanical waves) is negligible. This condition is satisfied for our scratching simulations where no mechanical vibrations are observed.

However, we observe $s < 0$ for the monocrystal and $s > 0$ for the polycrystal. This shows that plastic work is accumulated during scratching for the monocrystal, i.e., the heat generation is lower than the scratching work as some of the scratch work ends up bound in the crystal. For the polycrystals however, the high energy grain boundaries release stored potential energy as heat, i.e., the heat generation is greater than the scratching work as the crystal relaxes grain boundaries.

The indentation depth does not seem to have a significant influence on the sensitivity for the monocrystal. For polycrystals, the sensitivity decreases with increasing indentation depth. This tendency can be explained by the ploughing during scratch. At small indentation depths, only very little ploughing occurs and most of the scratch work is done in the form of frictional heating. The localised frictional heating leads locally to high temperatures allowing the high energy grain boundaries to relax. However at larger indentation depths, more of the scratch work is done in the form of ploughing, which leads to more plastic deformation in both grain boundaries and bulk. The bulk behaves like a single crystal and *stores* plastic energy when plastically deformed and thus counteracts the energy release in the grain boundaries.

The energy release mechanism can be qualitatively visualised by observing the evolution of the vertical centrosymmetry distribution during scratching as shown in Figure 3.13. For each snapshot, the substrate is cut in horizontal slabs of thickness a_y and for each slab, the mean centrosymmetry parameter of all atoms is computed[5] as a qualitative representation of the dislocation density.

Although the increase of mean temperature ΔT during the scratch is small (typically $\Delta T < 100$ K), the overall mean centrosymmetry increases during the scratch due to ΔT, the distributions of subsequent time steps have been made comparable by plotting the difference between the local mean centrosymmetry and the mean centrosymmetry of the entire lower half of the substrate. The contour thresholds have been chosen ad hoc for best visibility.

In the case of the single crystal, see Figure 3.13a, high dislocation density is initially only observed in the upper 10 to 20 Å of the substrate until at about $t \approx 750$ ps, when a dislocation loop enters the bulk quickly and remains at a depth of 50 Å for about one nanosecond before leaving the bulk again. After this, the high density region grows from the top down to about 50 Å. In the polycrystal, see Figure 3.13b, the initial distribution of dislocation density is due to the grain structure and it makes it impossible to discern individual dislocation loops. However, it can be seen that the high density region at about 22 Å shrinks over the duration of the scratch and disappears at about $t = 2$ ns and the relative dislocation density below the surface decreases.

We also observe that changes in dislocation density are essentially restricted to the

---

[5] The top slab, where the mean centrosymmetry is dominated by surface atoms, is not considered.

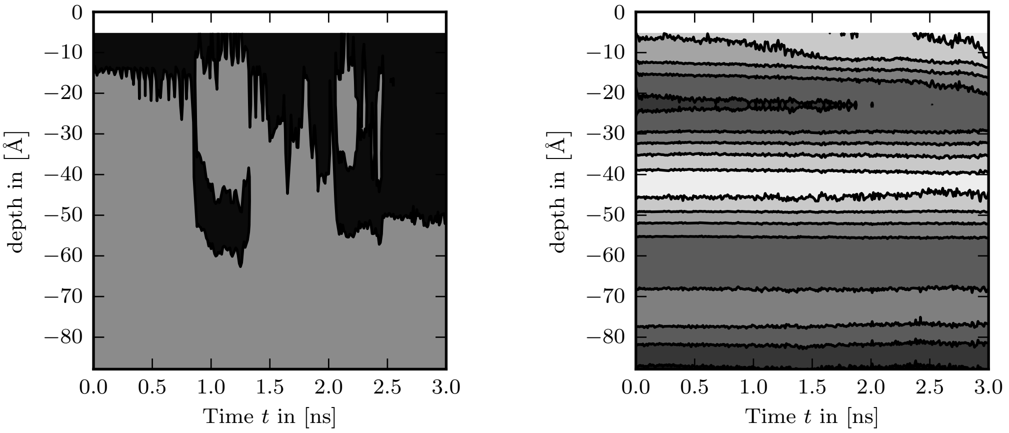

(a) Monocrystal. Note the appearance of a single dislocation loop at about $t \approx 750$ ps

(b) Polycrystalline microstructure #1, see Table 3.1

Figure 3.13 – Localisation of plastic activity in the substrate at $v = 10$ m/s for grazing contact $\Delta y = 0$ Å. Darker means a higher relative dislocation density. Note that the contour thresholds have been chosen ad hoc for best visibility and cannot be compared between Figures 3.13a and 3.13b.

top 25 Å in the case of the polycrystal while individual dislocations can travel far and quickly in the single crystal. This suggests that plasticity in the polycrystal is mostly confined within the grains and dislocations do not overcome grain boundaries. To support this conclusion, we have performed common neighbour analyses (CNA) on some of the microstructures during scratching and visualised examples of this confined dislocation activity, see Figure 3.14, which shows a dislocation life-cycle we typically observe in the microstructures.

Figure 3.14a shows an outside view of the situation as an overview. Green atoms are defect-free FCC atoms, pink is HCP (e.g., stacking fault between partials in FCC) and white, yellow and blue atoms are part of the amorphous grain boundaries. Note that these boundaries make up a substantial part of the structure. Free surfaces are not recognised as crystalline FCC and show up as white atoms. Figure 3.14b shows the same time step, where a vertical cut through the indenter path has been performed to view the zone under the indenter, where most of plasticity is expected to develop. On the right side of the white line, FCC atoms have been omitted to allow seeing defects inside the grains. All subsequent visualisations will also omit the crystalline FCC atoms. Note that the entire interior of the large grain under the indenter appears empty. This means that there is no crystal defect in the grain. When the indenter advances, however, a sheet of HCP atoms appears (white arrow in Figure 3.14c). This means that a partial dislocation must have crossed the grain and been absorbed by the grain boundary, leaving a stacking fault defect along its slip plane. The propagation of the partial dislocation is not shown, as it is too short-lived of a phenomenon to be captured by the visualisation frequency we

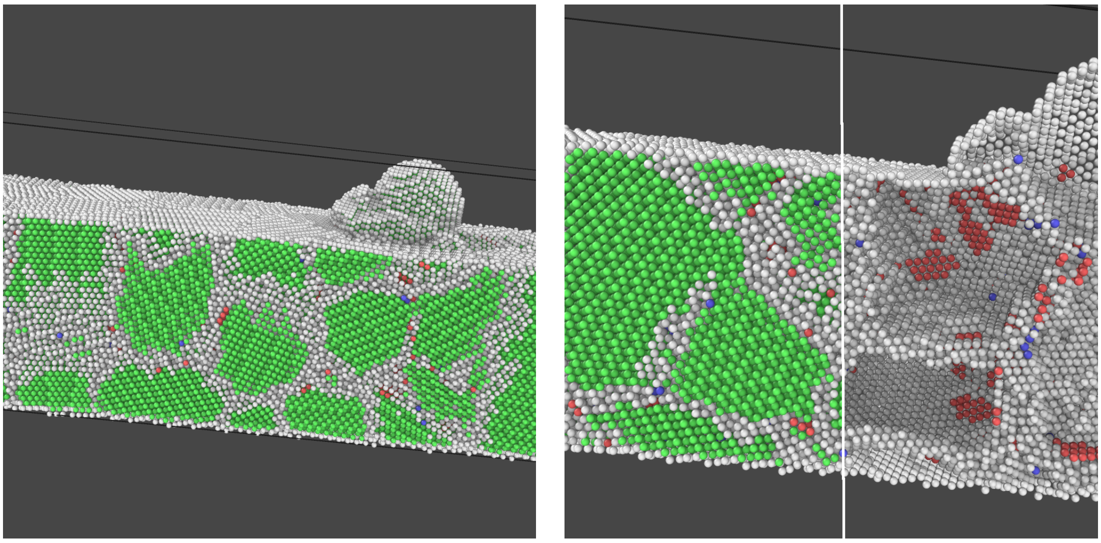

(a) Outside view

(b) Sliced view exposing a vertical cut surface through the indenter. FCC atoms are omitted on the right side to expose the interior of grains.

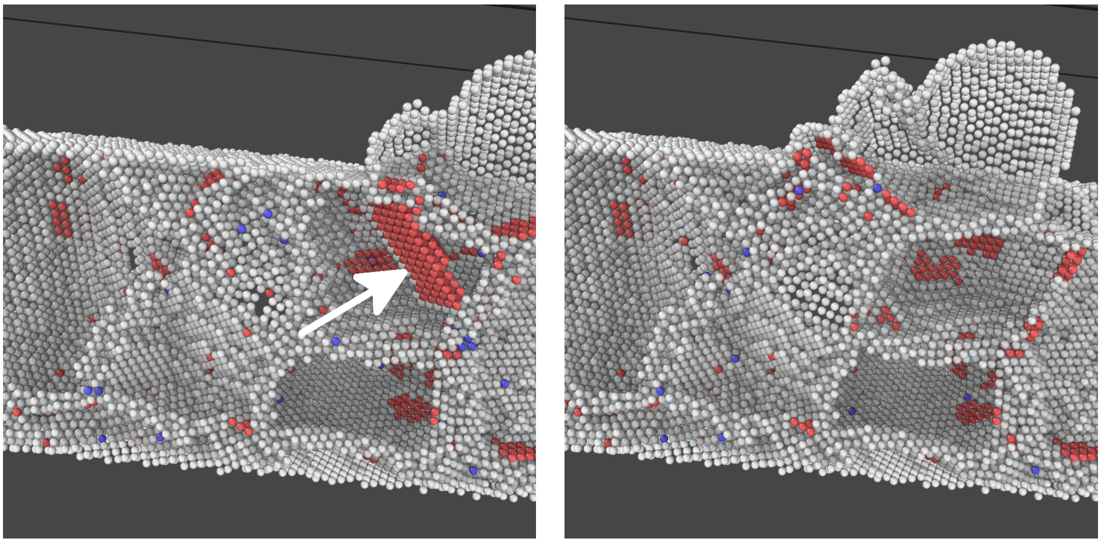

(c) Indenter has advanced by 4 Å with respect to Figure 3.14b. A layer of HCP atoms has formed (arrow).

(d) Indenter has advanced by another 26 Å, the entire grain has reverted back to FCC.

Figure 3.14 – Partial dislocation activity in microstructure #4 during the scratch with $\Delta y = 10$ Å . Green atoms are crystalline FCC (defect-free), pink are HCP (stacking fault) and white, blue and yellow atoms part of the amorphous grain boundaries.

used. Note also that much of the chip pushed in front of the indenter has recrystallised and itself now forms a part of the indenter. As the indenter advances (Figure 3.14d), the stacking fault sheet disappears again. This implies that either a trailing partial has also crossed the grain or that the previously observed partial has crossed back after the stress induced by the indenter is relieved. Either way, it appears in all similar situations we observed that dislocation activity is confined within grains and we could not find evidence of dislocations crossing grain boundaries. A more detailed analysis of plastic phenomena in the microstructure however exceeds the scope of this study and is left for future work.

The CNA and visualisations shown in Figure 3.14 have been performed using OVITO (Stukowski, 2009).

3.4 Conclusions

We have performed a large parametric molecular dynamics study of single-asperity aluminium nano-scratch simulations in which we varied the substrate thickness, indentation depth and the scratch speed over more than an order of magnitude each. Furthermore, several different microstructures where considered. The indenter size is about an order of magnitude smaller than a typical atomic force microscopy tip. Using a novel combined molecular dynamics and molecular statics approach for analysing nanoscale friction, we have been able to define a clean separation of the friction work W_{sc} into heat generation Q and creation or release of permanently stored plastic deformation energy E_{pl}. By comparing the evolution of the number of dislocated atoms $N_{\text{pl}}(t)$ to the evolution of the plastic energy $E_{\text{pl}}(t)$ for monocrystalline substrates we obtained strong indications that our method to compute E_{pl} is indeed able to accurately quantify the energy associated with plastic zones independently of how they have been created.

Both Q and E_{pl} have been found to be distinctly scratch speed dependent, but while Q increases with increasing speed, E_{pl} appears to do the opposite. This indicates that at higher scratch speeds, plasticity does not have the time to develop fully. Q appears to be simulation box size independent for large box sizes, but E_{pl} remains sensitive to the box size even for thick substrates.

Scratching on polycrystals revealed a friction mechanism which releases stored potential energy as heat and competes with the friction mechanism observed in monocrystals. In the range of very small grain sizes which were investigated here, this energy release mechanism is strong enough to overcompensate the energy accumulation associated with newly created plastic zones. It is possible that this would not be the case for microstructures with large grain sizes. Such large microstructures are, however, not easily tractable on current computing hardware.

We have presented a regression-based method to compute friction coefficients μ and defined a window-average for measurements extracted from the simulations. This window-average provided us with a statistically motivated criterion to determine that – for a wide range of moderate scratch speeds – there is a weak bell shaped speed sensitivity of μ, but at very high scratch speeds bulk plasticity is suppressed and the friction coefficient drops considerably. This behaviour corresponds, for a single scale model, remarkably well to known macroscale behaviour. The same criterion has shown that μ is simulation box size independent for thick substrates: the average value of μ seems to stabilise for substrates thicker than about five times the indentation depth. The associated E_{pl}, however, does not stabilise, indicating that the plastic zones are not resolved, even for the relatively small scratch case covered in this parametric study.

Allowing plastic zones to fully develop would require the modelling of substantially larger simulation domains, which come at prohibitively high computational cost if treated fully atomistically. The next chapter works towards a multiscale method specifically designed to allow the development of large plastic zones while retaining small atomistic domains.

4 A Road Map Towards 3D CADD

Only two-dimensional implementations of CADD exist to date, even though the method works in both two and three dimensions in principle. Two-dimensional discrete dislocation dynamics and CADD studies helped analyse and understand many interesting phenomena (e.g. Chakravarthy and Curtin, 2010; Nicola et al., 2007; Miller et al., 2004, to just mention a few), but many basic plastic phenomena, as for instance dislocation entanglement, Frank-Read sources *etc.* are *fundamentally* three-dimensional. An extension of CADD to the third dimension could therefore be very useful, but presents a number of challenges, which are reviewed here. For this thesis, I have worked out a practical road map for the implementation of a fully three-dimensional CADD that addresses each of these challenges and aims at minimising the required effort by using available, proven open-source solutions rather than developing them wherever possible.

This chapter reviews the obstacles to a three-dimensional CADD implementation by highlighting the fundamental differences between two and three-dimensional CADD, explains my proposed road map for a complete implementation of three-dimensional CADD and presents the parts of the road map that I have completed.

4.1 Differences Between 2D and 3D CADD

4.1.1 Dislocation Passing

The main advantage of CADD over other coupling methods is the possibility to nucleate dislocations in the atomistic subdomain Ω_{A} and have the evolving dislocations roam freely across the coupling interface $\partial\Omega_{\mathrm{AC}}$ into the continuum subdomain Ω_{C}, where they are computationally much cheaper to handle. Special care has to be taken when choosing the numerical recipe for letting dislocations cross the interface (referred to as "passing" in the context of two-dimensional problems, see *e.g.* Shilkrot et al. (2004)): the stress-strain fields around a dislocation core can be split into a highly nonlinear core region, where continuum mechanics fail to provide an adequate description and a far-field, where the continuum mechanics solution fits (Bulatov and Cai (2006, Chapter 10) or Hirth and Lothe (1992, Chapter 8)). While full molecular dynamics simulations handle both the core and the far-field correctly, the continuum with coupled finite-element and discrete dislocation dynamics modelling provides accurate strains –and therefore displacements– only for the far-field. As a consequence, spurious forces act on dislocation cores that approach the interface in coupled systems. When a molecular dynamics dislocation comes close to the interface (see Figure 4.1), its (normally) nonlinear core is intersected by $\partial\Omega_{\mathrm{AC}}$. The continuum part of the core (dark grey area in Figure 4.1) is constrained to linear elasticity instead of reacting nonlinearly and therefore exhibits exaggerated stresses, leading to a repulsive spurious force on the dislocation.

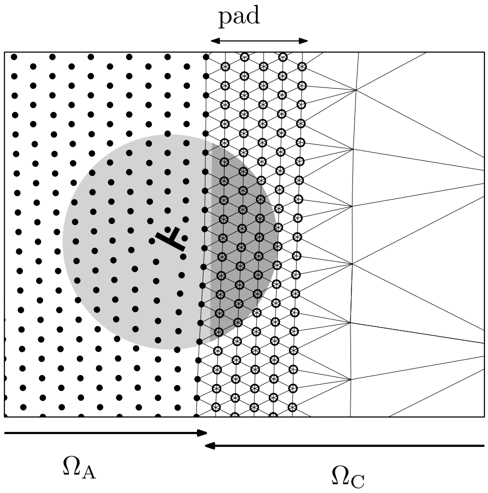

Figure 4.1 – Dislocation in the vicinity of the interface: the nonlinear core region (schematically represented by the grey area) interacts with the continuum across the interface. The continuum part of the core (dark grey) is linear elastic while the atomistic part is nonlinear, leading to spurious forces.

In the inverse case, when a discrete dislocation approaches the interface, an analogous spurious attractive force acts on the dislocation. The recipe for letting dislocations cross the interface needs to account for these spurious forces and minimise their effect.

Two-dimensional implementations are greatly simplified by the fact that dislocations are straight lines and parallel to domain interfaces, *i.e.* dislocations in a two-dimensional problem are essentially point entities that are either in the continuum or the atomistic domain without ambiguity. Three-dimensional dislocations however form loops that coalesce into networks which can be partly in the continuum, partly in the atomistic domain with dislocation segments intersecting the continuum/atomistic interface. Figure 4.2 illustrates the general situation.

In order to highlight the implications of this difference it is instructive to start by recalling how dislocations are passed across the interface in two-dimensional CADD (see Shilkrot

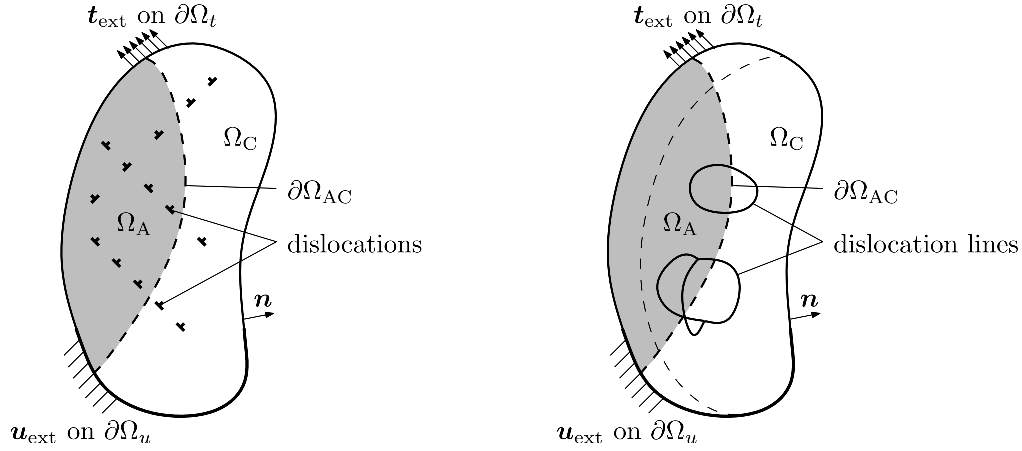
$\boldsymbol{t}_{\text{ext}}$ on $\partial\Omega_t$
Ω_C
$\partial\Omega_\text{AC}$
Ω_A
dislocations
$\boldsymbol{n}$
$\boldsymbol{u}_{\text{ext}}$ on $\partial\Omega_u$
$\boldsymbol{t}_{\text{ext}}$ on $\partial\Omega_t$
Ω_C
$\partial\Omega_\text{AC}$
Ω_A
dislocation lines
$\boldsymbol{n}$
$\boldsymbol{u}_{\text{ext}}$ on $\partial\Omega_u$

(a) In two dimensions, dislocations are individual point entities, located in *either* the continuum *or* the atomistic domain. They are all edge dislocations.

(b) In three dimensions, dislocations form loops and networks, spanning across the interface $\partial\Omega_\text{AC}$. Contiguous dislocation loops can *simultaneously exist* implicitly in Ω_A and explicitly in Ω_C by spanning across $\partial\Omega_\text{AC}$.

Figure 4.2 – Two-dimensional simplifications that are no longer valid in three-dimensional problems

et al. (2004, Section 3.3) for the full details): as a dislocation approaches the interface, schematically shown in Figure 4.3a, the dislocation is detected[1] before the nonlinear core (grey area) interacts with the continuum (*i.e.* before a spurious repulsion force from the interface acts on the dislocation) and is passed into the continuum region by inserting a dislocation dipole that cancels the original molecular dynamics dislocation, see Figure 4.3b.

The jump distance is just long enough to ensure that the nonlinear area never intersects the interface and is commonly estimated to a few lattice spacings. For example, Dewald and Curtin (2006) find that in aluminium, spurious forces are significant if a dislocation comes closer than about 20 Å (depending on the dislocation's character angle) to the interface. Two types of errors occur during the insertion of the dislocation dipole that annihilates the molecular dynamics dislocation and creates the discrete dislocation in the continuum: a) the annihilation is not exact, since the nonlinear atomistic core is compensated by a linear elastic solution leading to a local displacement residual where the core used to be and b) the jump itself is not physical since the displacement error immediately after the passing corresponds to the field of the dislocation dipole. However, several successful two-dimensional CADD studies have shown that these errors have an insignificant impact on the overall behaviour.

---

[1] The detection method used in the original description defines a band of detection atoms in the bulk that are constantly monitored for relative displacement consistent with a passing dislocation. The details can be found in Shilkrot et al. (2004).

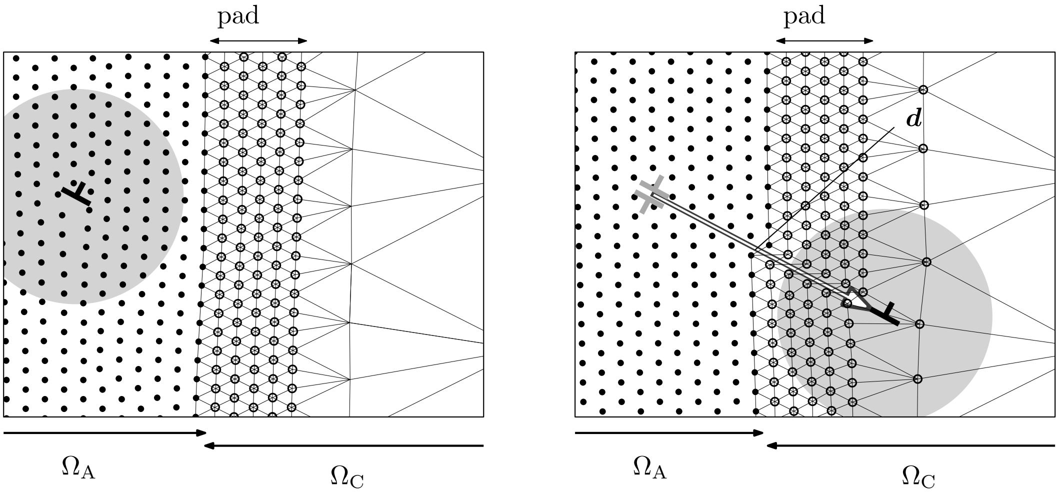

(a) A dislocation approaches the interface, which is slightly deformed under its influence. The grey area around it represents schematically the nonlinear core that is not allowed to interact with the continuum, to avoid spurious forces.

(b) A dislocation dipole of spacing $||\boldsymbol{d}||$ has been introduced astride the interface. The dislocation in the molecular dynamics domain is thereby (approximately) annihilated, and has seemingly made a jump along $\boldsymbol{d}$ into the continuum. Here, the grey area represents the (erroneously) linear core. Note the shear band in the slip of the dislocation, made very visible by the distorted mesh.

Figure 4.3 – Dislocation passing in two dimensions. The dislocations never get close to the interface.

In essence, two-dimensional CADD offers the possibility to trade the error due to spurious forces of dislocation-interface interaction (which can lead to dislocation pinning and pile-up at the interface) for an error due to the insertion of a dislocation dipole (which is very short range). This trade-off is a tremendous simplification of the method, but it is only applicable in two dimensional problems.

4.1.2 Dislocation Detection

Only edge dislocations on a very small set of slip planes (three for a hexagonally close-packed plane) occur in two-dimensional CADD. In order to detect a dislocation approaching the interface, it suffices to monitor a narrow band of atoms for the kinematic footprint of the approaching core (see Shilkrot et al., 2004, for details). This simplicity is lost in three-dimensional simulations, where more slip systems can be active and dislocation lines can have arbitrary character angles. A further complication due to the third dimension is the need of *detected and constrained discrete dislocation nodes* inside the molecular dynamics domain to provide boundary conditions for dislocation segments that point from the continuum into the atomistic domain. These constrained nodes will be discussed in a bit more detail in Section 4.5. In any case, the problem of dislocation detection and identification in three-dimensional problems is a notable complication over the detection band of the original two-dimensional CADD.

Stukowski et al. (2012) and Stukowski and Albe (2010) developed a method called *Dislocation Extraction Algorithm* (DXA) that performs Burgers circuit analyses and computes a line segment representation of entire dislocation networks (and other defects such as grain boundaries). It is possible that the integration of such a full-blown analysis method into three-dimensional CADD will prove necessary. Preliminary discussions with the main author and developer of DXA have indicated that the method could indeed be adapted to provide the information CADD needs.

4.2 Road Map and Achieved Mile Stones

Figure 4.4 shows schematically the architecture of a modular CADD implementation. The goal of the modular approach is to use existing and proven open-source codes wherever possible and to unite them within a central coupling framework in the hopes to minimise duplicate developments and maintain high overall performance while concentrating all efforts on the coupling between the various code blocks. The three main code blocks that need to be made to work together are a finite-element solver, a molecular dynamics solver and a discrete dislocation dynamics solver, which I subsequently refer to as the *computational domains*.

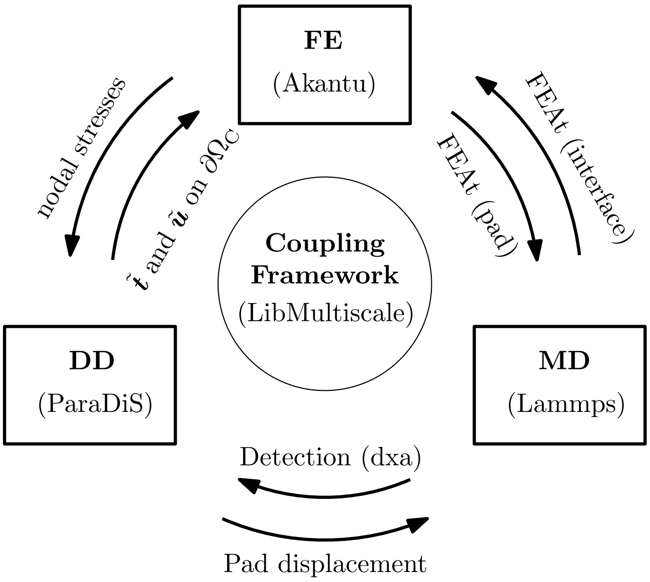
FE
(Akantu)
nodal stresses
$\tilde{\boldsymbol{t}}$ and $\tilde{\boldsymbol{u}}$ on $\partial\Omega_C$
FEAt (pad)
FEAt (interface)
Coupling Framework
(LibMultiscale)
DD
(ParaDiS)
MD
(Lammps)
Detection (dxa)
Pad displacement

Figure 4.4 – Schematic of CADD coupling using the preexisting and proven open-source codes Lammps, Akantu, and ParaDiS as plugins for the finite-element (FE), molecular dynamics (MD), and discrete dislocation dynamics (DD) domains within the coupling framework of LibMultiscale. The six distinct flows of information between the three domains are represented by the arrows.

The central coupling framework has two tasks: it manages the exchange of data between the domains and synchronises their progress in time.

4.2.1 Coupling Framework

LibMultiscale (see Anciaux, 2009; Anciaux et al., 2006) is a parallel C++ framework specifically developed for multiscale coupling methods using existing external software projects for the physics calculations of the coupled domains. It has been used successfully for a massively parallel implementation of the bridging domain method (see Section 2.4.2 or (Xiao and Belytschko, 2004)), among others and is currently developed and maintained in-house.

A particularly useful feature of LibMultiscale is the abstraction of the computational domains: it defines interfaces to generic finite-element, molecular dynamics, and discrete dislocation dynamics domains. The interfaces provide access to their domain's degrees of freedom and to the steps of their main integration loops. Coupling methods are then defined in relation to these abstract domain interfaces, and are fully agnostic of the actual piece of code, called the *plugin*, that performs the underlying physics computations. This has the great advantage that plugins for the same domain are in principle interchangeable. Should any of the three plugins chosen here – Akantu for the finite-element method, Lammps for molecular dynamics, and ParaDiS for discrete dislocation dynamics – prove to be a bad choice in the future, or should a better alternative emerge, replacing the plugin does not affect the implementation of the coupling. Through the heavy use of template metaprogramming, LibMultiscale achieves this feature without sacrificing performance.

The functional principle of LibMultiscale is the following: the main computational loops of the plugins are broken up into individual steps, which are then performed by LibMultiscale instead of the original code. Between the steps, LibMultiscale uses the abstract domain interfaces to intervene and manipulate degrees of freedom of the plugins to enforce the coupling.

For instance, a typical molecular dynamics code integrates the equations of motion by applying the velocity Störmer-Verlet scheme (see LAMMPS, 2010; Rapaport, 2004; Griebel et al., 2007), and dynamic finite-element codes typically use the explicit Newmark β algorithm (see Zienkiewicz, 1986; Hughes, 1987; Curnier, 2000).[2] Both schemes are commonly split into the three parts predictor, force computation, and corrector. The abstract molecular dynamics and finite-element domains provide access to them as well as access to the degrees of freedom of the domains. By having LibMultiscale execute the steps, the domains are synchronised, and in between the steps, LibMultiscale can intervene within the domains to realise a multiscale coupling. Because this is done through the abstract domain interfaces, the coupling can be engineered independently of what code is used as plugins. This genericity makes it possible to reuse some of the existing code base of LibMultiscale that has been developed for the bridging domain method, see Anciaux et al. (2006).

---

[2] Note that the Newmark β method with $\beta = 0$ and $\gamma = \frac{1}{2}$ and the velocity Störmer-Verlet scheme are the same thing.

The mentioned qualities make LibMultiscale an excellent framework for the implementation of three-dimensional CADD.

4.2.2 External Software Projects

The following existing software projects have been selected in order to reduce the amount of code that needs to be written for the CADD implementation.

- **Molecular dynamics: Lammps**
  The Large-scale Atomic/Molecular Massively Parallel Simulator (Lammps), see LAMMPS (2010) is a very widely used and well documented open-source classical molecular dynamics C++ code (see LAMMPS, 2010; Plimpton, 1995). A LibMultiscale plugin for Lammps existed already before the beginning of this research, making it an obvious choice for the molecular dynamics domain.
- **Finite elements: Akantu**
  Akantu (Richart and Molinari, 2014; Richart et al., 2010) is a very efficient open-source parallel C++ finite-element code. Its design as a library greatly helps the development of plugins. Akantu is developed in-house, which makes it convenient to follow closely and influence its further development. This allows to profit from improvements in the plugin without breaking compatibility with LibMultiscale.
- **Discrete dislocation dynamics: ParaDiS**
  The Parallel Dislocation Simulator (ParaDiS) is an open-source, large scale discrete dislocation dynamics code written in C (Cai et al., 2004a; Bulatov et al., 2004). The code base is relatively small and easy to modify into a plugin. A major strong point of ParaDiS is that the algorithms it implements and theory it bases itself on are very well described in the literature, see *e.g.*, Cai et al. (2006); Bulatov and Cai (2006); Cai et al. (2004b); Cai (2001).

4.2.3 Milestones

In order to formulate all the individual pieces of code that need to be written for the full implementation and how they have to work together, it is instructive to go through the process of writing the CADD coupling scheme in algorithmic form. For this, we look at the individual domains and how they integrate their equations of motion in time to determine at which points in their integration schemes LibMultiscale has to intervene with coupling actions.

Molecular dynamics or explicit dynamic finite-element domain: As mentioned earlier, the most widely used time integration scheme in molecular dynamics is velocity Störmer-Verlet (Griebel et al., 2007) and in explicit dynamic finite-element it is Newmark β (Hughes, 1987; Curnier, 2000). Both methods are usually implemented as a predictor-corrector algorithm, which is shown in simplified form in Algorithm 4.1. The main loop starts after the initial conditions are set and the initial accelerations have been calculated. In the first step, the predictor, the positions (or displacements) $\boldsymbol{r}$ and velocities $\dot{\boldsymbol{r}}$ are updated. Note that the updated $\dot{\boldsymbol{r}}$ are not yet the final velocity of the time step, but $\boldsymbol{r}$ is definitive for this time step. The second step, consists in computing the forces based on the new positions to update the accelerations $\ddot{\boldsymbol{r}}$.[3] The updated forces are finally used to compute the final $\dot{\boldsymbol{r}}$ of the time step, and the loop starts over. Since CADD is a displacement coupling method, any coupling action needs to occur after the predictor step, or it will couple outdated positions (or displacements) $\boldsymbol{r}$, but also before the force calculation or the force calculation will be based partly on updated $\boldsymbol{r}$ (the local degrees of freedom) and partly on outdated $\boldsymbol{r}$ (the boundary conditions managed by an external coupling partner domain).

Algorithm 4.1 Simplified main loop of for a velocity Störmer-Verlet or explicit Newmark β scheme with $\gamma = \frac{1}{2}$. The degrees of freedom $\boldsymbol{r}$ correspond to displacements $\boldsymbol{u}$ in the case of finite elements and positions $\boldsymbol{x}$ in the case of molecular dynamics.

```
$\boldsymbol{r} \leftarrow \boldsymbol{r}_0$, $\dot{\boldsymbol{r}} \leftarrow \dot{\boldsymbol{r}}_0$, $t \leftarrow t_0$        ▷ Set initial conditions
$\ddot{\boldsymbol{r}} \leftarrow f(\boldsymbol{f}(\boldsymbol{r}), \boldsymbol{m})$        ▷ acceleration is function of forces $\boldsymbol{f}$ and masses $\boldsymbol{m}$
while $t < t_{\text{end}}$ do        ▷ Main loop
    Step 1, Predictor:
        $\dot{\boldsymbol{r}} \leftarrow \dot{\boldsymbol{r}} + \frac{1}{2}\Delta t\, \ddot{\boldsymbol{r}}$        ▷ tentative, often indexed $\dot{\boldsymbol{r}}_{t+\frac{1}{2}\Delta t}$
        $\boldsymbol{r} \leftarrow \boldsymbol{r} + \Delta t\, \dot{\boldsymbol{r}}$        ▷ definitive, often indexed $\boldsymbol{r}_{t+\Delta t}$
    Step 2, Force calculation:
        $\ddot{\boldsymbol{r}} \leftarrow f(\boldsymbol{f}(\boldsymbol{r}), \boldsymbol{m})$        ▷ definitive, often indexed $\ddot{\boldsymbol{r}}_{t+\Delta t}$
    Step 3, Corrector:
        $\dot{\boldsymbol{r}} \leftarrow \dot{\boldsymbol{r}} + \frac{1}{2}\Delta t\, \ddot{\boldsymbol{r}}$        ▷ definitive, often indexed $\dot{\boldsymbol{r}}_{t+\Delta t}$
    $t \leftarrow t + \Delta t$
end while
```

Molecular statics or static finite-element domain: Such quasistatic domains are particularly simple to couple in CADD: because of the absence of dynamics, every static computation simply yields the degrees of freedom $\boldsymbol{r}$ that correspond to the current boundary conditions without notion of outdatedness. Coupling actions occur after the static solution to the current boundary conditions is computed.

---

[3] Note that it is assumed here that the forces depend purely on $\boldsymbol{r}$. Care must be taken when viscous forces or thermostats are present. These complications, however, occur (and can be solved) independently of the coupling issues and are therefore neglected here for the sake or clarity.

Discrete dislocation dynamics domain: Even though the equations of motion of a discrete dislocation dynamics system are simple first order ordinary differential equations, see (2.10) or (Cai and Bulatov, 2004), the time integration of discrete dislocation dynamics systems is a cumbersome affair: discrete dislocation dynamics systems have to deal with dislocation node collisions and frequently, dislocation segments need to be split or merged. Because of these events, discrete dislocation dynamics time integration schemes do not have a constant or predictable time step, see Bulatov et al. (2004) or Bulatov and Cai (2006) for details. Therefore, the discrete dislocation dynamics domain potentially needs to perform multiple fractional time steps during a single global CADD time step. Fortunately, no part requires the forces based on the final configuration, and all these complications remain hidden from the coupler inside the plugin. Coupling steps occur after the integrator reaches the end of the time step.

Coupled procedure: Having established that all CADD coupling actions need to occur between the predictor and force computation for dynamic domains and after the main step for quasistatic domains or discrete dislocation dynamics domains, the full coupling can be formulated. Algorithm 4.2 shows the simplified main loop for the full CADD coupling scheme.[4] It is essentially the temporal representation of Figure 4.4.

After the initialisation of the domains, which entails the reading of input files, allocation of working memory, setting of initial conditions *etc.* for all plugins plus, for dynamic domains like molecular dynamics and discrete dislocation dynamics, usually a first calculation of the forces in the system, the main loop is entered.

- **Step 1:**
  Each domain computes the positions for the new time step. For the static finite-element domain and the discrete dislocation dynamics domain, this means doing a complete iteration of the main loop they would have in an uncoupled problem. The molecular dynamics domain merely performs the predictor step of its integration scheme
- **Coupling Step:**
  All coupling actions occur now. The three pair interactions between the domains are;

---

[4] The algorithm describes the coupling scheme for a quasistatic continuum, rather than a dynamic one. This makes no difference regarding the implementation of the coupling scheme itself, however I show that fully dynamic CADD suffers from severe numerical stability issues in Chapter 5 and therefore generally prefer to discuss it in the quasistatic context.

Algorithm 4.2 CADD Coupling algorithm with quasistatic continuum

```
Initiate finite-element domain
Initiate molecular dynamics domain
Initiate discrete dislocation dynamics domain
$t \leftarrow t_0$
while $t < t_{\text{end}}$ do                                   ▷ Main loop
    Step 1:                                  ▷ LibMultiscale executes plugin code
        FE:  Full static solve
        MD:  Verlet prediction
        DD:  Full step
    Coupling step :                        ▷ LibMultiscale executes coupling code
        FE → MD:  Set pad atom positions from FE nodes
        MD → FE:  Set interface node displacements from atoms.
        DD → FE:  Subtract $\tilde{\boldsymbol{t}}$ and $\tilde{\boldsymbol{u}}$ from free and blocked boundary nodes.
        FE → DD:  Provide $\hat{\boldsymbol{\sigma}}$ on DD nodes.
        MD → DD:  Detect dislocations and set constrained DD nodes.
        DD → MD:  Add $\tilde{\boldsymbol{u}}$ to pad atoms.
    Step 2:                                  ▷ LibMultiscale executes plugin code
        MD:  Compute forces
    Step 3:                                  ▷ LibMultiscale executes plugin code
        MD:  Verlet correction
    $t \leftarrow t + \Delta t$
end while
```

  - **MD $\leftrightarrow$ FE**
    The interaction between finite-element and molecular dynamics domains corresponds to the FEAt method described in Section 2.4.5. The current positions of the pad nodes are communicated to the molecular dynamics domain to set the corresponding pad atoms accordingly and in the inverse direction, the positions of the interface atoms are communicated to the finite-element domain to update the corresponding interface nodes.
  - **FE $\leftrightarrow$ DD**
    This part of the coupling corresponds to the discrete dislocation dynamics method as described in Section 2.2.2. The finite-element boundary conditions need to be corrected for the fact that the dislocation stress-strain fields are computed for an infinite solid by subtracting the displacements $\tilde{\boldsymbol{u}}$ from all boundary nodes on which Dirichlet conditions are imposed (including coupling interface nodes) and the tractions $\tilde{\boldsymbol{t}}$ from the remaining boundary nodes. In the reverse way, the elastic stresses need to be evaluated in the finite-element domain on the positions of discrete dislocation nodes and communicated to the discrete dislocation dynamics domain.
  - **DD $\leftrightarrow$ MD**
    To the best of my knowledge, the steps involved in this interaction are unique to CADD. Within the molecular dynamics domain, dislocations are detected and their Burgers vector, line direction and slip plane communicated to the discrete dislocation dynamics domain. The “detected and constrained” discrete dislocation nodes are then set accordingly. The displacement field $\tilde{\boldsymbol{u}}$ is evaluated on pad atom positions by the discrete dislocation dynamics domain and communicated to the molecular dynamics domain, where it is added to the pad atom position according to (2.7).

- **Step 2:**
  The explicit dynamic domains (in this example only the molecular dynamics domain) perform the force computations.

- **Step 3:**
  The explicit dynamic domains (in this example only the molecular dynamics domain) perform the corrector step.

Now that all the steps of the CADD coupling procedure are detailed, they can be grouped into mostly independent pieces of code to implement. The most obvious ones are the plugins,

- The **Lammps plugin** allows LibMultiscale to run molecular dynamics calculations using Lammps through the molecular dynamics domain interface. This piece of code mostly existed at the beginning of this research and only minor adaptations where necessary for the CADD project. This plugin is fully implemented and well-tested.

- The **Akantu plugin** lets LibMultiscale run finite-element calculations through the finite-element domain interface. At the beginning of the CADD project, the plugin supported sequential explicit dynamics and has since been extended to both static and explicit dynamic calculations with periodic boundary conditions including periodic boundary conditions with initial strain (which will be used in Section 4.3) as well as large-scale parallel calculations with non-periodic boundary conditions. Anisotropic elastic and viscoelastic constitutive laws as well as the capability to evaluate stresses in any point in the domain (for discrete dislocation dynamics coupling) have also been added for CADD. The capabilities of this plugin are thoroughly tested.
- The **ParaDiS plugin** is partially implemented. At the time of the writing of this thesis, the plugin allows LibMultiscale to run ParaDiS calculations, to add and constrain dislocation Nodes on the fly and to evaluate the stress $\tilde{\boldsymbol{\sigma}}$ and displacement $\tilde{\boldsymbol{u}}$ fields.[5]

The tasks of the coupling step are more interesting. The order in which they are presented subsequently has been chosen so that every newly implemented task (coupler) allows to solve a new type of problem that can serve as test case.

- **FEAt coupling** has been fully implemented and works in sequential as well as parallel simulations, in statics, dynamics and mixed situations where for instance the atomistic domain is dynamic and the continuum quasistatic. The coupling also supports periodic boundary conditions with the periodic boundaries intersecting the coupling interface. The only constraint is that the mesh be fully refined in the entire pad region and all pad/interface atoms need to coincide with a finite-element node.

  Test problems:

  - Standard patch test:
    In a patch test, a coupled domain Ω is subject do Dirichlet boundary conditions that correspond to a uniform strain by applying the displacement

    $$\boldsymbol{u}(\boldsymbol{x}) = \boldsymbol{\epsilon}\,\boldsymbol{x} \tag{4.1}$$

    on the domain boundary $\partial\Omega$, where $\boldsymbol{\epsilon}$ is a (small) strain tensor and $\boldsymbol{x}$ a position in the undeformed domain. The static equilibrium is calculated and the displacement of the bulk degrees of freedom are compared to the theoretical displacements (4.1). The test is not interesting enough to be discussed in detail here, but the coupler passes it.

---

[5] The capability to evaluate $\tilde{\boldsymbol{u}}$ has been implemented in collaboration with the Laboratory for Multiscale Mechanics Modeling (LAMMM).

- Dynamic test:
  The thorough testing of this coupler has led to the observation the FEAt/-CADD coupling has severe stability problems in fully dynamic systems. Chapter 5 is dedicated to a detailed description and analysis of this instability, and provides recommendations as to how to manage or solve the instability. The instability strongly limits the usefulness of fully dynamic test cases, however an interesting semi-dynamic test case is a periodic array of straight dislocations, discussed in more detail in Section 4.3.

- **DD ↔ MD: pad coupling and dislocation detection:** The displacement of the pad atoms is given by the superposition of the elastic solution $\hat{\boldsymbol{u}}$ (provided by the FEAt coupling) and the displacement due to the dislocation segments $\tilde{\boldsymbol{u}}$. The latter field is tricky: while it is straight-forward to compute the linear far field displacement due to a dislocation network by triangulating it (see Barnett, 1985), the nonlinear core region needs to be treated with special care to avoid spurious forces on dislocation segments intersecting the interface. No coupler has been developed for a generic case as of yet, however a method to deal with the nonlinear core, called the *dislocation core template* has been developed theoretically and is discussed in some detail in Section 4.4. Its generic implementation is one of the goals of a PhD project subsequent to this one. The second half, the dislocation detection and identification in the general case, is still an open question and even though ideas for its solution exist (see Section 4.1.2) none have been developed yet.

Test Problems

- The infinite hybrid[6], straight edge dislocation that intersects the interface at a right angle appears to be the only test case that does not require FEAt coupling nor an elastic solution from the continuum (because the displacement field of edge dislocation is restricted to the plane spanned by the Burgers vector and the normal to the slip plane). A somewhat simplistic proof of concept implementation of this test case has been implemented and is discussed in some detail in Section 4.5. The test does not require a complicated detection method because there is only a single dislocation line and both its slip plane and Burgers vector are known *a priori*.
- Because the straight hybrid edge dislocation can only test the edge core template, the test case of a straight hybrid dislocation of arbitrary character angle intersecting the interface at a right angle should be the next step.

---

[6] I refer to dislocation lines which are partly discrete dislocation dynamics, partly molecular dynamics, intersecting the interface as hybrid.

Because such a dislocation's displacement field has a non-zero component normal to the interface, however, this problem requires the FEAt coupling, the DD ↔ MD coupling and the FE ↔ DD coupling and has to wait for full CADD to be implemented.

- **FE ↔ DD coupling:** This third and last coupler is straight forward compared to the complications of the two others.

Test Problems Any test case in which dislocations are present in a finite continuum domain can serve as a test case, there is no particular difficulty present.

4.3 Periodic Array of Straight Dislocations

The problem of a periodic array of straight dislocations is successfully used in the literature for dislocation mobility studies in molecular dynamics (e.g. Olmsted et al., 2005). In this section, the problem is modified by replacing the molecular dynamics domain is by a CADD/FEAt-coupled domain, of which only a fraction around the slip plane is atomistically refined. This system provides not only a good test case for the coupling implementation, including periodic boundary conditions intersecting the coupling interface, but also a cheaper way to evaluate dislocation mobility. Figure 4.5 illustrates the setup with the example of an edge dislocation.

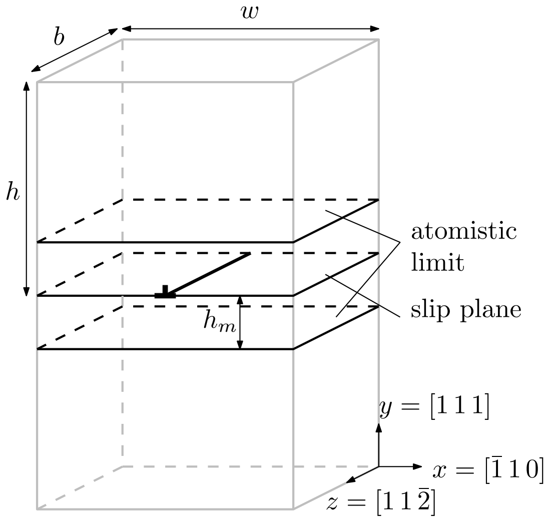

Figure 4.5 – Setup for coupled periodic array of straight dislocations. A domain of height $2h$, thickness b and width w is subject to periodic boundary conditions in the x and z directions. Only the slab of thickness $2h_m$ in the centre of the domain is atomistically refined. The planes marked "atomistic limit" are the coupling interfaces.

The test case simulates a block of pure aluminium using the EAM potential developed by

Mendelev et al. (2009) in the atomistic domain and an anisotropic, linear elastic, small strain constitutive law in the continuum that is fitted to the potential. The continuum is modelled using static finite elements. As we will see subsequently, this mixed quasistatic approach leads to a shortened transient regime before the steady state glide velocity is reached. A straight edge dislocation slips in the $(1\,1\,1)$ plane of its FCC lattice, its Burgers vector points in the $[\bar{1}\,1\,0]$ direction and the dislocation line is parallel to the $[1\,1\,\bar{2}]$ direction. See Appendix C for details on how to rotate the anisotropic elastic tensor $\mathbb{C}$ of the continuum to fit this orientation. Periodic boundary conditions are imposed in the dislocation line direction and the Burgers direction. The domain therefore represents a periodic array of infinitely long, straight edge dislocations.[7] The bottom surface is fixed and the top surface is subject to traction in Burgers direction. The centre of the domain is atomistic with a thickness of h_m on either side of the slip plane. With the entire central slab atomistically refined, the dislocation line never exits the atomistic domain and no CADD-specific dislocation passing concerns exist. Because of the massive reduction in the number of degrees of freedom in the coupled domain compared to a full molecular dynamics domain, its height $2h$, thickness b and width w could be chosen to be larger than what can be handled in molecular dynamics, but in this test case, the full molecular dynamics system will be used as a reference to evaluate the effectiveness of the coupling. I chose the dimensions

$$h = 40\,a_y, \tag{4.2}$$

$$b = 6\,a_z, \tag{4.3}$$

$$w = 37\,a_x, \tag{4.4}$$

$$h_m \in \{0, 5, 10\}\,a_y \tag{4.5}$$

where the a_i are the size of the oriented lattice in the direction of i-th axis of the coordinate system and $h_m = 0$ corresponds to the full molecular dynamics system. Table 4.1 lists the number of degrees of freedom for each of the systems.

	MD	FE top	FE bottom	total
$h_m = 5\,a_y$	225288	68028	73302	366618
$h_m = 10\,a_y$	386208	68721	73989	528918
$h_m = 0\,a_y$	1287360	0	0	1287360

Table 4.1 – Number of degrees of freedom in domain by subdomains.

In order to accommodate the dislocation, the initial, undeformed domain must have a step on its surface, where the cut plane of the dislocation intersects the boundary, see Figure 4.6a). In order to obtain an approximation of the relaxed initial displacements, the superposition of the displacement field of the dislocation and several of its periodic images is applied to all nodes and atoms, leading to a block with nearly plane boundaries containing the dislocation, see Figure 4.6b), causing the step to be reduced to a bump. The periodic boundary conditions, however, require the finite-element mesh to have flat and parallel periodic boundaries or spurious deadload stresses will occur. To avoid these, the bumped side is simply flattened numerically, leading to some initial spurious compressive stresses on the interface which disappear during the initial equilibration to relax the dislocation core.

---

[7] Note that the setup is not restricted to edge dislocations, but the edge dislocation suffices to demonstrate a functional coupling.

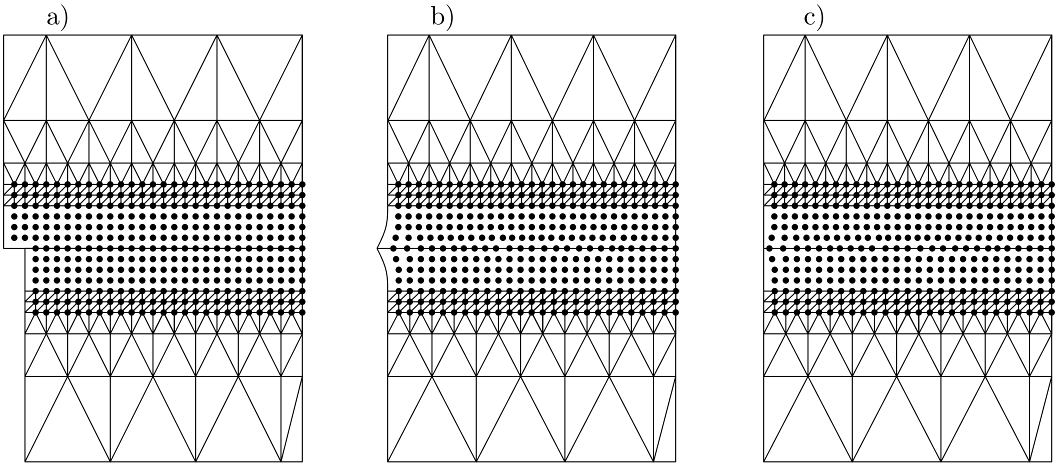

Figure 4.6 – Initialisation of periodic geometry. The initial geometry a) has a step where the dislocation cut plane intersects the boundary. After the application of the superposed displacement fields of several periodic images of the dislocation, b), the step becomes a bump. The bump is subsequently pushed flat c) for the finite-element periodic boundary conditions to function.

Figure 4.7 shows the three test cases in their initial configuration. The colouring indicates displacement in x direction with dark red being half a Burgers in the positive sense and dark blue in the negative sense. For the two coupled cases in Figure 4.7b and 4.7c, the edges of the finite elements are shown in order to illustrate the varying mesh density: the interface and pad are fully resolved with every interface/pad atom coinciding with a node. Further away from the coupling interfaces, the mesh rapidly coarsens. This leads to a very high concentration of finite-element degrees of freedom near the interface and explains why both coupled domains have nearly the same number of finite-element degrees of freedom despite their meshes having significantly different volumes.

The simulation starts with 2000 time steps with viscous damping on the atomic degrees of freedom in order to relax the dislocation core and the initial spurious compressive stress along the periodic boundary in x direction. After relaxation a traction in x-direction $\boldsymbol{t} = [34, 0, 0]$ MPa is applied on the top surface and the entire system is sheared in the

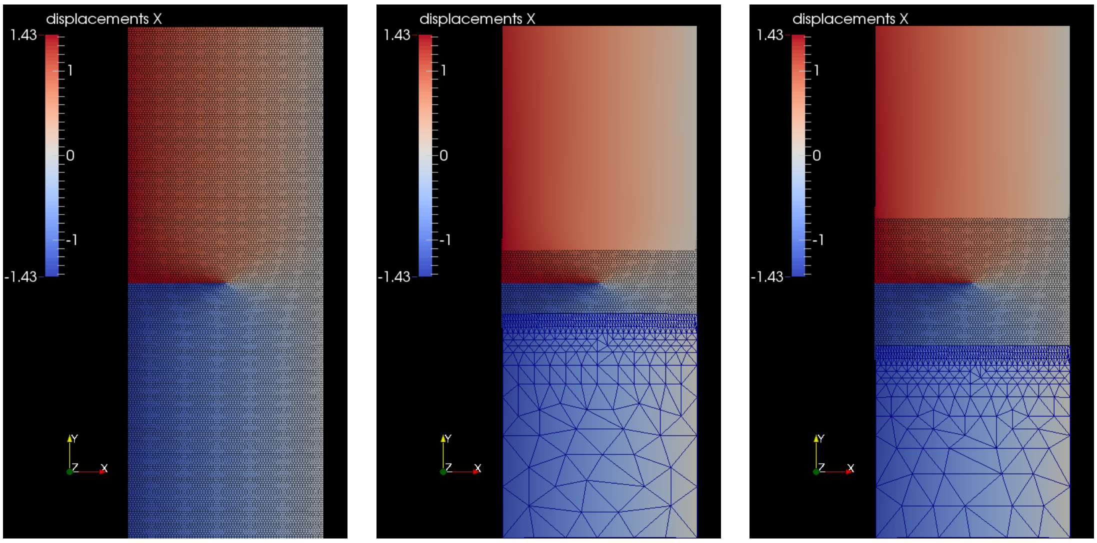

(a) Fully atomistic reference system (b) Coupled system, $h_m = 5\,a_y$ (c) Coupled system, $h_m = 10\,a_y$

Figure 4.7 – Coupled setups for a periodic array of straight dislocations.

x-y plane by

$$\gamma_{xy} = \frac{t_x}{C_{xyxy}}. \tag{4.6}$$

Under the shear stress, the dislocation rapidly accelerates and traverses the periodic boundary multiple times. In order to track the dislocation motion, the centrosymmetry parameter P_i for each atom i (see Kelchner et al., 1998) is computed periodically. The current dislocation position x_d is then estimated as the mean atomic position x_i weighted by P_i

$$x_\mathrm{d} = \frac{\sum_i P_i\, x_i}{\sum_i P_i}. \tag{4.7}$$

The centrosymmetry parameter can also be used to visualise the moving dislocation. Figure 4.8 show three snapshots from the simulation of the system $h_m = 5\,a_y$, where atoms with $P > 1$ are represented as white balls while all other atoms are shown translucent. It can be seen that the dislocation stays straight and quite compact an crosses the periodic boundary. Figure 4.9a shows the estimated dislocation position x_d as a function of time for all three systems. The duration of the initial transient regime increases with increasing molecular dynamics domain. This is no surprise since only the molecular dynamics domain has inertia and the static finite-element domain instantly adjust to the stress field. As the dislocation starts moving, two release waves travel up and down from the slip plane and shield the core, thus reducing its driving force. However, once the transient regime is overcome, all three systems exhibit identical dislocation velocities

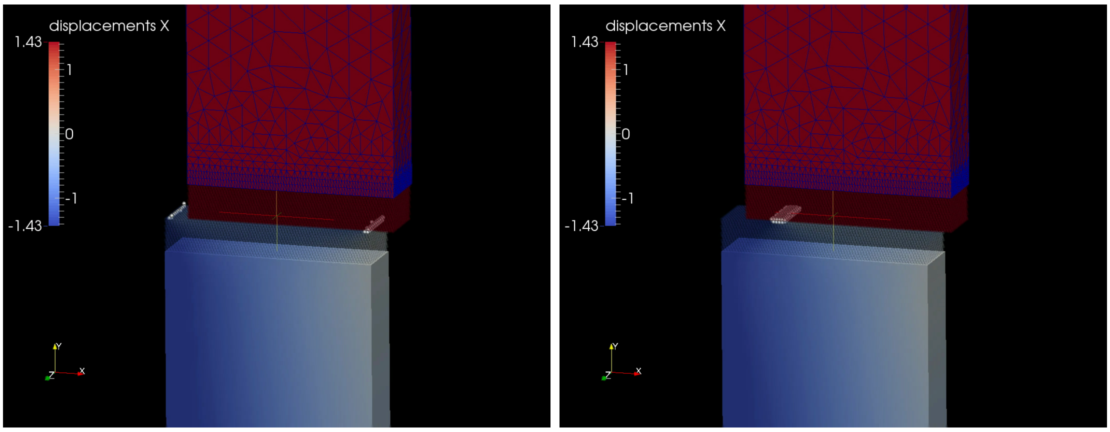
displacements X
1.43
1
0
-1
-1.43
Y
Z
X
displacements X
1.43
1
0
-1
-1.43
Y
Z
X

(a) Dislocation just crossing the periodic boundary.

(b) Dislocation advancing.

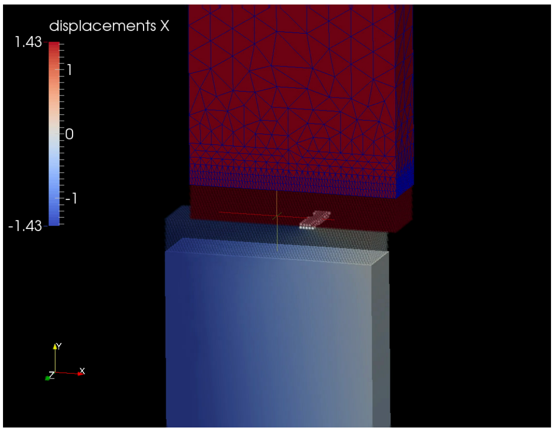
displacements X
1.43
1
0
-1
-1.43
Y
Z
X

(c) Dislocation advancing.

Figure 4.8 – The periodic array of straight dislocations travelling. Atoms with a centrosymmetry larger than one are shown as white balls to visualise the dislocation line. All other atoms are partly transparent. In order to help understand the illustrations, the meshes and atoms are warped by the real displacement, *i.e.* the periodic displacement has been unraveled to show the step created by accumulated slips of repeated dislocation passages.

for almost 100 ns after which the velocities of the coupled systems decrease significantly. A look at the temperature development shown in Figure 4.9c reveals that the decrease in velocity coincides with a significant increase in temperature. The increase in temperature explains the reduced dislocation mobility.

The FEAt/CADD coupling passes this test flawlessly.

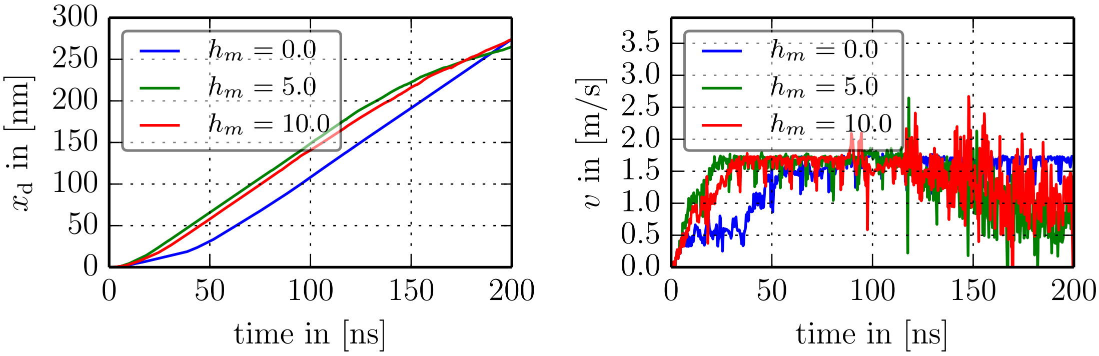

(a) Position as function of time. Transient regime lasts longer for larger molecular dynamics part. The steady-state slope is perfectly identical for all three systems until the saturation. Saturation occurs earlier for smaller molecular dynamics part.

(b) Velocity as function of time. Confirms that indeed, the steady-state slopes of the curves Subfigure (a) coincide.

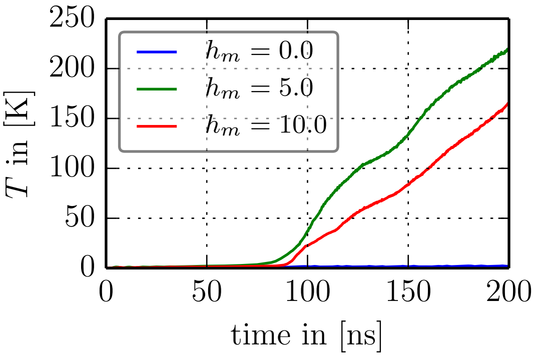

(c) Temperature as function of time. Temperature rises very slowly until for the coupled system the temperature rate suddenly increases. Increase in temperature coincides with saturation of dislocation velocity.

Figure 4.9 – Dislocation motion: coupled system vs full molecular dynamics

4.4 Dislocation Core Template

In order to reduce the dislocation dipole spacing during dislocation passing in two-dimensional CADD, Dewald and Curtin (2006) developed what they call a template of the full atomistic displacements that allows to reduce the distance at which spurious forces appear and allows a reduction of the jump distance. I propose to extend the concept and to apply it to three-dimensional dislocations that are intersected by the interface. The fundamental groundwork on this subject is presented here.

As explained in Section 4.1.1, the origin of the spurious forces when dislocations approach the interface is the linear reaction of the pad atoms within the core. The main idea of the dislocation core template is to correct the linear displacement field in the core region by a precomputed empirical and nonlinear displacement field, the so-called *core template*. I define the *exact* core template $\Delta\tilde{\boldsymbol{u}}_{\mathrm{c}}(\boldsymbol{x}_0)$ for an atom with original position $\boldsymbol{x}_0$ as the error of the plastic contribution $\tilde{\boldsymbol{u}}(\boldsymbol{x}_0)$ of a dislocation network in a system without elastic strain $\hat{\boldsymbol{u}}(\boldsymbol{x}_0) = \mathbf{0}$

$$\begin{aligned}\Delta\tilde{\boldsymbol{u}}_{\mathrm{c}}(\boldsymbol{x}_0) &= \boldsymbol{u}_{\mathrm{A}}(\boldsymbol{x}_0) - \tilde{\boldsymbol{u}}(\boldsymbol{x}_0), &(4.8)\\ &= \boldsymbol{u}_{\mathrm{A}}(\boldsymbol{x}_0) - \sum_j \tilde{\boldsymbol{u}}_j(\boldsymbol{x}_0), &(4.9)\end{aligned}$$

where $\boldsymbol{u}_{\mathrm{A}}(\boldsymbol{x}_0)$ is the exact atomistic solution and $\tilde{\boldsymbol{u}}_j(\boldsymbol{x}_0)$ is the contribution of the j-th discrete dislocation segment. The template can therefore be seen as a corrective field for the discrete dislocation dynamics solution. Let us furthermore assume that the atomistic solution can be split into individual contributions from the discrete dislocation segments as well

$$\boldsymbol{u}_{\mathrm{A}}(\boldsymbol{x}_0) = \sum_j \boldsymbol{u}_{\mathrm{A},j}(\boldsymbol{x}_0), \tag{4.10}$$

then the template can also be expressed in terms of such contributions

$$\Delta\tilde{\boldsymbol{u}}_{\mathrm{c}}(\boldsymbol{x}_0) = \sum_j \Delta\tilde{\boldsymbol{u}}_{\mathrm{c},j}(\boldsymbol{x}_0) = \sum_j \left[\boldsymbol{u}_{\mathrm{A},j}(\boldsymbol{x}_0) - \tilde{\boldsymbol{u}}_j(\boldsymbol{x}_0)\right]. \tag{4.11}$$

Far from any dislocation core, non-linear effects become negligible, and the small-strain linear elasticity solution $\tilde{\boldsymbol{u}}$ converges with the atomic solution $\boldsymbol{u}_{\mathrm{A}}$. With $r_d(\boldsymbol{x}_0)$ defined as the distance between $\boldsymbol{x}_0$ and the nearest dislocation core, this is expressed as

$$\lim_{r_d(\boldsymbol{x}_0)\to+\infty} ||\Delta\tilde{\boldsymbol{u}}_{\mathrm{c}}(\boldsymbol{x}_0)|| = 0. \tag{4.12}$$

This allows a practical definition of the dislocation core as the set of points C

$$C = \{\boldsymbol{x}_0 : ||\Delta\tilde{\boldsymbol{u}}_{\mathrm{c}}(\boldsymbol{x}_0)|| > \kappa\}, \tag{4.13}$$

for which the norm of the correction is greater than a suitably chosen positive tolerance κ. If κ is small enough, we can approximate the core template for a point $\boldsymbol{x}_0 = \boldsymbol{x}_{\mathrm{i}}$ inside the core of the k-th dislocation segment[8] as

$$\Delta\tilde{\boldsymbol{u}}_{\mathrm{c}}(\boldsymbol{x}_{\mathrm{i}}) = \sum_j \Delta\tilde{\boldsymbol{u}}_{\mathrm{c},j}(\boldsymbol{x}_{\mathrm{i}}) \approx \sum_j \delta_{kj}\Delta\tilde{\boldsymbol{u}}_{\mathrm{c},j}(\boldsymbol{x}_{\mathrm{i}}) = \Delta\tilde{\boldsymbol{u}}_{\mathrm{c},k}(\boldsymbol{x}_{\mathrm{i}}) \quad \forall \boldsymbol{x}_{\mathrm{i}} \in C_k \tag{4.14}$$

and for a point $\boldsymbol{x}_0 = \boldsymbol{x}_{\mathrm{o}}$ outside any core the approximate template is simply

$$\Delta\tilde{\boldsymbol{u}}_{\mathrm{c}}(\boldsymbol{x}_{\mathrm{o}}) = \sum_j \Delta\tilde{\boldsymbol{u}}_{\mathrm{c},j}(\boldsymbol{x}_{\mathrm{o}}) \approx \boldsymbol{0} \quad \forall \boldsymbol{x}_{\mathrm{o}} \notin C. \tag{4.15}$$

Note The empirical field $\boldsymbol{u}_{\mathrm{A},j}(\boldsymbol{x})$ is expressed a function of spatial coordinates as if the atomistic displacement field were defined everywhere in space instead of just on atomic positions. The details of how to obtain such a field will be discussed a bit later. For now we assume its existence and accuracy.

Figure 4.10 illustrates the application of the template: A dislocation line intersects the interface. Without a template, pad atoms are regular points in a discrete dislocation dynamics domain and their displacements are given by the superposition of the elastic solution $\hat{\boldsymbol{u}}$ and the solution due to all dislocation segments $\tilde{\boldsymbol{u}}$, see (2.7). In order to minimise spurious forces, we distinguish between pad atoms inside the nonlinear dislocation core (grey cylinder of radius r_{c} in the figure) and pad atoms in the linear elastic region.

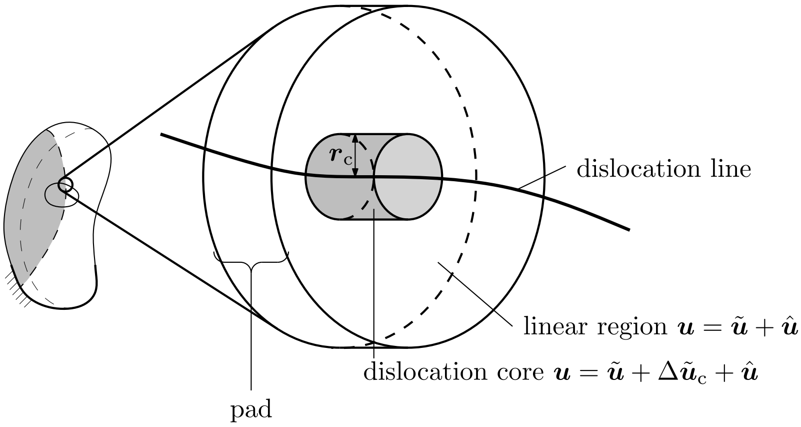
r_{c}
dislocation line
linear region $\boldsymbol{u} = \tilde{\boldsymbol{u}} + \hat{\boldsymbol{u}}$
dislocation core $\boldsymbol{u} = \tilde{\boldsymbol{u}} + \Delta\tilde{\boldsymbol{u}}_{\mathrm{c}} + \hat{\boldsymbol{u}}$
pad

Figure 4.10 – Schematic of dislocation core in the pad. For most of the pad, the linear elastic discrete dislocation dynamics displacement solution is adequate, in the vicinity of the dislocation line, however, adding the core template $\Delta\tilde{\boldsymbol{u}}_{\mathrm{c}}$ is required to minimise spurious forces.

The template correction field $\Delta\tilde{\boldsymbol{u}}_{\mathrm{c}}$ is added to the pad atoms within the core. With the help of (4.14) and (2.8) it is easily shown that this eliminates spurious forces for a pad atom in the core of dislocation segment j

---

[8] This formally requires $\boldsymbol{x}_{\mathrm{i}}$ not to be in the core of any other segment.

$$
\begin{aligned}
\boldsymbol{u} &= \hat{\boldsymbol{u}} + \Delta\tilde{\boldsymbol{u}}_{\mathrm{c}} \qquad + \tilde{\boldsymbol{u}}, && (4.16)\\
&= \hat{\boldsymbol{u}} + \underbrace{\boldsymbol{u}_{\mathrm{A},j} - \tilde{\boldsymbol{u}}_j}_{(4.14)} + \underbrace{\sum_{i=1}^{n} \tilde{\boldsymbol{u}}_i}_{(2.7)}, && (4.17)\\
&= \hat{\boldsymbol{u}} + \boldsymbol{u}_{\mathrm{A},j} \qquad + \sum_{\substack{i=1\\ i\neq j}}^{n} \tilde{\boldsymbol{u}}_i, && (4.18)
\end{aligned}
$$

where $\hat{\boldsymbol{u}}$ does not produce spurious forces as long as the discrete dislocation dynamics assumption of small strains is not violated, $\sum_{\substack{i=1\\ i\neq j}}^{n} \tilde{\boldsymbol{u}}_i$ contains only (small-strain) far field contributions of distant dislocation segments, since the closest one, j, is explicitly excluded, and $\boldsymbol{u}_{\mathrm{A},j}$ is the empirical atomistic displacement.

With the idea behind the template clearly defined, it is useful to state the limitations imposed on the problem of interest before going into the details of how to obtain a template.

- **Dislocation spacing:** Implicit in the template definition (4.8) is the assumption that dislocations lines in the pad are spaced far from one another, *i.e.* no two dislocation cores overlap. If this assumption is violated and two dislocation lines approach one another, there will be spurious forces acting on them in the pad.
- **Accuracy and simplicity:** The template is only useful if it can be precomputed and looked up during the simulation. This means that the displacement field for dislocation cores with arbitrary character angle and curvature needs to be accurately interpolatable from a finite number of precomputed dislocation cores.

4.4.1 Computing a Basic Core Template

As a simple example, this section details the extraction of the template for a prismatic dislocation core in magnesium from the atomic positions of a relaxed dislocation core. The dislocation core was obtained in a molecular statics computation using a Mendelev EAM potential (Mendelev et al., 2009). The details of the simulation are of no importance here, because the focus is on extracting the atomistic displacement field from it. The main idea is to interpret atoms as nodes of a finite element mesh on which the atomic displacements are interpolated like nodal values. For simplicity, the method considers only straight dislocations[9] and the coordinate system is chosen so that the line vector $\boldsymbol{\xi} = \boldsymbol{z}$ coincides with the z axis and the normal to the slip plane $\boldsymbol{n} = \boldsymbol{y}$ with the y axis, see Figure 4.11. The template can then be assumed to be a function of only x and y, and not of z, specifically, the atomic displacement field $\boldsymbol{u}_{\mathrm{A}}$ has the functional form

---

[9] The validity of this assumption is untested.

$$\boldsymbol{u}_{\mathrm{A}} = [u_{\mathrm{A}x}, u_{\mathrm{A}y}, u_{\mathrm{A}z}] = \boldsymbol{f}(\boldsymbol{x}) = \boldsymbol{f}([x, y]) . \tag{4.19}$$

The extraction follows five steps.

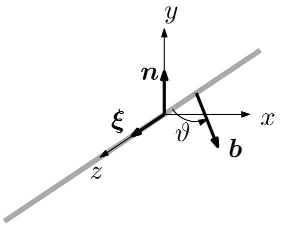

Figure 4.11 – Geometric setup for core template extraction. The fat grey line represents the straight infinite dislocation line. Because the line direction $\boldsymbol{\xi}$ coincides with the z axis and the normal to the slip plane $\boldsymbol{n}$ with the y axis, the burgers vector $\boldsymbol{b}$ is constrained to be in the $x - z$ plane. The character angle of the dislocation is ϑ.

1. For a given character angle ϑ, generate a dislocation and relax the system in a molecular statics minimisation. For simplicity, the dislocation line is assumed to coincide with the z axis. The line direction vector is then $\boldsymbol{\xi} = [0\,0\,1]$
2. Extract the original atomic positions $\boldsymbol{x}_{0,i}$ from within the core ($||\boldsymbol{x}|| \leq r_{\mathrm{c}}$) and the corresponding final relaxed positions $\boldsymbol{x}_{\mathrm{r},i}$. The index i refers to the i-th atom in the core. Compute the atomic displacements

$$\boldsymbol{u}_i = \boldsymbol{x}_{\mathrm{r},i} - \boldsymbol{x}_{0,i}. \tag{4.20}$$

3. Project $\boldsymbol{x}_{0,i}$ onto the $x - y$ plane in order to obtain a two-dimensional set of points $\bar{\boldsymbol{x}}_{0,i}$

$$\bar{\boldsymbol{x}}_{0,i} = \begin{bmatrix} 1 & 0 & 0 \\ 0 & 1 & 0 \end{bmatrix} \boldsymbol{x}_{0,i}. \tag{4.21}$$

   This set of points contains many duplicate or near duplicates because atoms are projected on top of one another. Clean up the set by looping through all pairs of neighbouring projected atoms and disregard one atom of each pair that is significantly closer to one another than the typical interatomic spacing.

4. Compute the Delaunay triangulation of the points $\bar{\boldsymbol{x}}_{0,i}$ (Delaunay, 1934).
5. The triangles are interpreted as linear triangular finite elements (e.g. Belytschko et al., 2000; Tadmor et al., 2012). In order to use the triangulation for efficient interpolation, the shape functions and isoparametric mapping of spatial coordinates

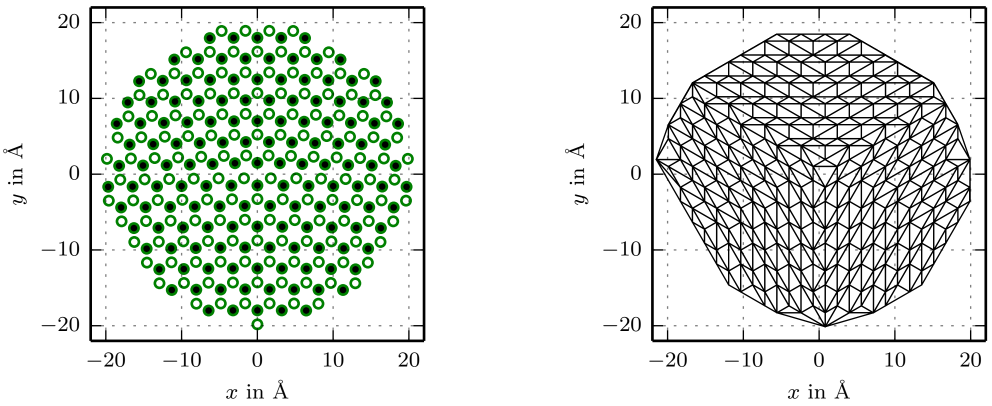

(a) Extracted core atoms. Because of the HCP structure of Magnesium, two overlapping hexagonal structures are visible when looking along the dislocation line. Note that the core is well visible in the centre and stayed fully compact.

(b) The mesh is based of initial positions, while the cutoff is applied in the deformed configuration. Therefore the mesh is asymmetric and contains no dislocation.

Figure 4.12 – Extracted core of a prismatic dislocation in magnesium.

to natural elemental coordinates are precomputed. The elemental shape functions N_i for triangles are

$$\left.\begin{aligned} N_1(\boldsymbol{\eta}) &= \eta_1, \\ N_2(\boldsymbol{\eta}) &= \eta_2, \\ N_3(\boldsymbol{\eta}) &= 1 - \eta_1 - \eta_2, \end{aligned}\right\} \tag{4.22}$$

where the η_i are the natural coordinates of the archetypal elements, (e.g. Gmür, 2000). The spatial coordinates of a point $\boldsymbol{\eta} = [\eta_1, \eta_2]$ are obtained for an element by interpolating the nodal positions using these shape functions

$$\boldsymbol{x}(\boldsymbol{\eta}) = \sum_{i=1}^{3} N_i(\boldsymbol{\eta}) \boldsymbol{x}_i, \tag{4.23}$$

where $\boldsymbol{x}_i$ are the coordinates of the i-th node of the element in question. Substituting (4.22) into (4.23) yields

$$\begin{bmatrix} x \\ y \end{bmatrix} = \begin{bmatrix} x_1 - x_3 & x_2 - x_3 \\ y_1 - y_3 & y_2 - y_3 \end{bmatrix} \begin{bmatrix} \eta_1 \\ \eta_2 \end{bmatrix} + \begin{bmatrix} x_3 \\ y_3 \end{bmatrix}, \tag{4.24}$$

> or, in homogenised coordinates $\bar{\boldsymbol{\eta}}$ and $\bar{\boldsymbol{x}}$
>
> $$\underbrace{\begin{bmatrix} 1 \\ x \\ y \end{bmatrix}}_{\bar{\boldsymbol{x}}} = \underbrace{\begin{bmatrix} 1 & 0 & 0 \\ x_3 & x_1 - x_3 & x_2 - x_3 \\ y_3 & y_1 - y_3 & y_2 - y_3 \end{bmatrix}}_{\mathbf{S}_{\boldsymbol{x}}} \underbrace{\begin{bmatrix} 1 \\ \eta_1 \\ \eta_2 \end{bmatrix}}_{\bar{\boldsymbol{\eta}}}, \tag{4.25}$$
>
> where $\mathbf{S}_{\boldsymbol{x}}$ is the elemental coordinate transformation matrix. Note that – for non-degenerate elements – $\mathbf{S}_{\boldsymbol{x}}$ is inversible and the inverse relationship $\bar{\boldsymbol{\eta}} = \mathbf{S}_{\boldsymbol{x}}^{-1}\bar{\boldsymbol{x}}$ holds. Analogously, the elemental displacement matrix $\mathbf{S}_{\boldsymbol{u}}$ can be defined
>
> $$\underbrace{\begin{bmatrix} 1 \\ u_x \\ u_y \\ u_z \end{bmatrix}}_{\bar{\boldsymbol{u}}} = \underbrace{\begin{bmatrix} 1 & 0 & 0 \\ u_{3,x} & u_{1,x} - u_{3,x} & u_{2,x} - u_{3,x} \\ u_{3,y} & u_{1,y} - u_{3,y} & u_{2,y} - u_{3,y} \\ u_{3,z} & u_{1,z} - u_{3,z} & u_{2,z} - u_{3,z} \end{bmatrix}}_{\mathbf{S}_{\boldsymbol{u}}} \underbrace{\begin{bmatrix} 1 \\ \eta_1 \\ \eta_2 \end{bmatrix}}_{\bar{\boldsymbol{\eta}}}. \tag{4.26}$$
>
> The interpolated displacement $\bar{\boldsymbol{u}}$ for a point $\bar{\boldsymbol{x}}$ inside the element is then given by
>
> $$\bar{\boldsymbol{u}}(\bar{\boldsymbol{x}}) = \mathbf{S}_{\boldsymbol{u}}\mathbf{S}_{\boldsymbol{x}}^{-1}\bar{\boldsymbol{x}}. \tag{4.27}$$
>
> Compute $\mathbf{S}_{\boldsymbol{u}}$ and $\mathbf{S}_{\boldsymbol{x}}^{-1}$ for every element and tabulate them. Note that (4.27) gives a mathematical definition to the atomistic displacement field $\boldsymbol{u}_{\mathrm{A}}$ discussed earlier.

With the matrices $\mathbf{S}_{\boldsymbol{u}}$ and $\mathbf{S}_{\boldsymbol{x}}^{-1}$ tabulated for each element, the core template $\Delta\tilde{\boldsymbol{u}}_{\mathrm{c}}$ can be computed on the fly during simulations. In order to deal with arbitrary character angles, the template needs to be computed for a range of angles and the resulting displacement field interpolated between nearest angles.

This idea is mostly untested for the time being and its full implementation is now subject of a successor PhD thesis.

4.5 Straight Hybrid Dislocations

We refer to dislocation lines that cross the coupling interface $\partial\Omega_{\mathrm{AC}}$ as hybrid dislocations, because they have two different descriptions on either side of the interface, yet are a single entity. In the atomistic domain Ω_{A}, the dislocation exists implicitly whereas it is modelled explicitly as a sequence of discrete dislocation nodes and segments in the continuum domain.

The simulation of a moving straight hybrid dislocation can be used as a test bed for core templates: ideally, the dislocation moves with equal velocity on either side of $\partial\Omega_{\mathrm{AC}}$, and the spurious forces in the pad are small enough not to pin the dislocation line at the coupling interface. This makes the study of straight hybrid dislocations a useful milestone in the implementation of three-dimensional CADD. The general setup for such a dislocation is schematically shown in Figure 4.13: a dislocation line intersects the interface at a right angle. In order for the dislocation to stay straight, the boundary conditions along the dislocation line direction (z in the figure) need to be either periodic or symmetric, thus mimicking an infinitely long line.

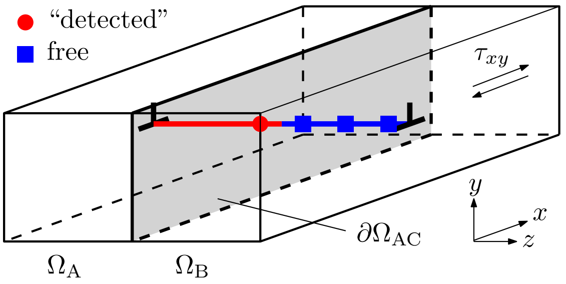

Figure 4.13 – Simulation setup for straight hybrid dislocation. The blue squares represent regular free discrete dislocation dynamics nodes. The constrained "detected" node, represented by the red disk, is moved by the coupling scheme, not the discrete dislocation dynamics method. The interface (marked grey) is intersected at a right angle.

In the example of a pure edge dislocation, the displacement field is planar and confined to the x-y plane as long as the dislocation stays straight, *i.e.* does neither bow out, get pinned nor move at different speeds in the two domains. This case allows a further simplification: as long as the line remains straight, the contribution of the finite-element domain is uniform and can be replaced by a simple uniform stress. Assuming that the dislocation mobility law used in the discrete dislocation dynamics part of the dislocation is well fitted to the temperature and potential in the molecular dynamics domain, the only forces that could make the line non-straight are spurious pinning forces at the interface.

Figure 4.14 illustrates the motion of the hybrid dislocation during one iteration of the CADD scheme defined in Algorithm 4.2. Initially at $t = t_n^+$,[10] the dislocation line is straight and the nonlinear core region of the molecular dynamics dislocation is accommodated at the pad using a core template. The template is centred around the dislocation segment that intersects the interface. The free discrete dislocation dynamics nodes – represented by blue disks – are subject to a Peach-Koehler force illustrated by the blue arrows. The detected and constrained end node – the blue cross – is considered blocked by the discrete dislocation dynamics domain. During the first step of the coupling scheme, the dislocation advances by an increment Δl on most of its length with the exception of the interface, where the domains provide each other's (blocked) boundary conditions, *i.e.* the pad atoms and the detected and constrained discrete dislocation dynamics node retain the position of $t = t_n^+$ at $t = t_{n+1}^-$. A pinning effect is visible in the

---

[10] The exponent $()^+$ indicates the time instantly after the coupling step, an exponent $()^-$ instantly before.

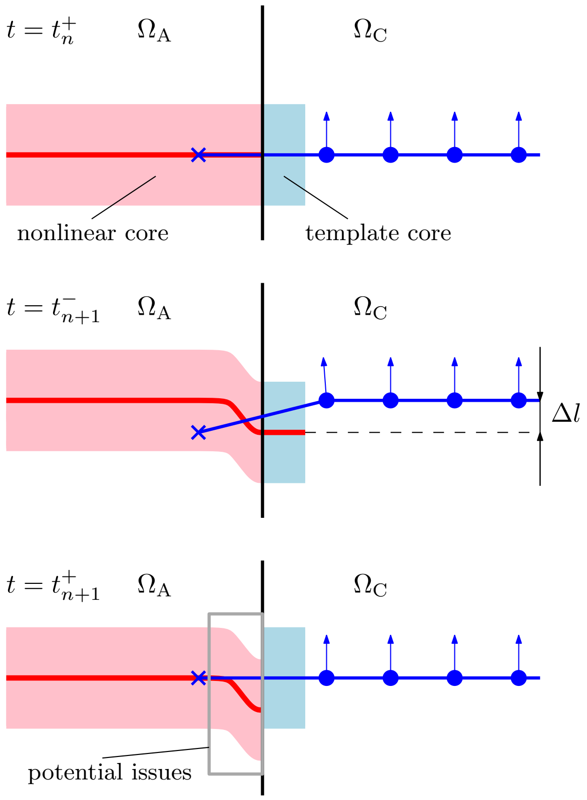

Figure 4.14 – Hybrid dislocation pinning at the interface

schematic. During the coupling step, the molecular dynamics dislocation is re-detected and the constrained node is put back into the centre of the dislocation line, thus re-straightening the discrete dislocation line at $t = t_{n+1}^+$. Note that the molecular dynamics dislocation line is still nominally crooked at its end (framed area in the figure). Keeping in mind that a dislocation only advances by a small fraction of a Burgers vector per time step $\Delta l \ll ||B||$ and the non-linear core is typically several Burgers vectors in diameter, this effect appears small and it is difficult to predict whether it is a problem or not at the current state of development.

In order to test the coupling scheme from a purely algorithmic point of view, the proof-of-concept setup of the hybrid dislocation has been further simplified without too much regard for mechanical accuracy.[11] The considered system is schematically depicted in Figure 4.15a. The molecular dynamics domain is comprised of a block of magnesium of width w, height h and thickness b. The lattice orientation (indicated next to the coordinate system) is such that a prismatic dislocation line along the z axis can glide on the x-y plane. Magnesium has been chosen here because its prismatic edge dislocation cores have the property of staying perfectly compact. We use the Mendelev et al. (2009)

---

[11] A complete simulation, with adequate boundary conditions is left as future work, after the template method is fully implemented.

EAM potential with a cutoff radius $r_{\text{cut}} = 7.5$ Å. The discrete dislocation dynamics domain is very large, effectively mimicking an infinite solid. Initially, an edge dislocation along the z axis is introduced in both the discrete dislocation dynamics and the molecular dynamics domain as pictured in Figure 4.15a. In the molecular dynamics domain, this is done by applying the Volterra field of isotropic linear elasticity (e.g. Bulatov and Cai, 2006; Hirth and Lothe, 1992) on all atoms. The last and the first node of the discrete dislocation is a constrained node and is not moved by the discrete dislocation dynamics domain. All atoms within r_{cut} of the outer boundary are considered as pad atoms and not moved by the molecular dynamics domain. The initial state is shown in Figure 4.15b.

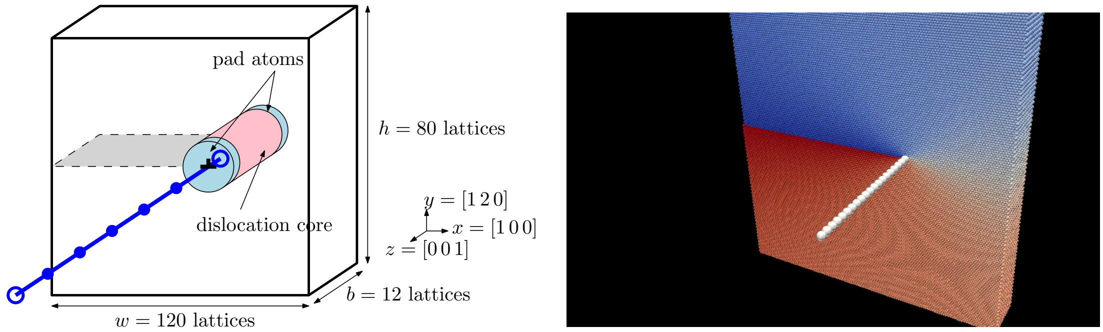

(a) Schematic setup of simplified hybrid dislocation simulation. The pad region (light blue cylinders) are shown only in the core region for clarity.

(b) Initial configuration. The atoms are coloured by displacement in x direction. The displacement discontinuity across the cut surface in the slip plane is clearly visible as the sharp transition from blue to red. The location of the dislocation core is at the edge of the cut plane. The discrete dislocation nodes are represented by the large white spheres.

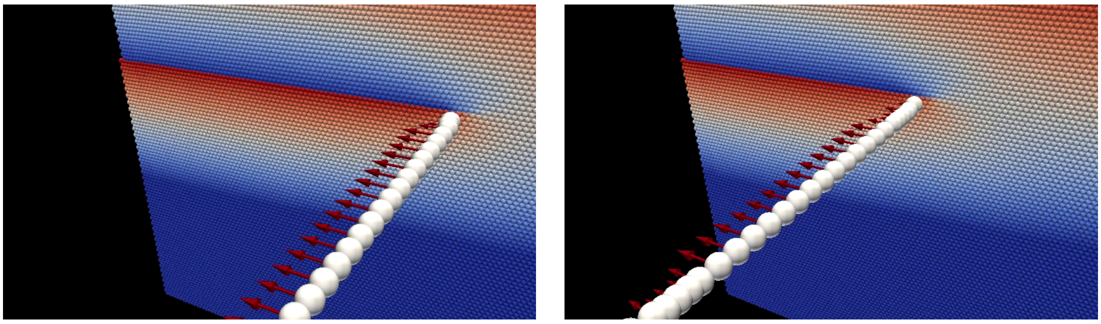

(c) The crystal is severely sheared and a uniform shear stress is applied on the discrete dislocation dynamics domain. Only the atoms of the central slice of the crystal are shown here in order to visualise the interior. The Peach-Koehler forces on the dislocation nodes are illustrated by the red arrows.

(d) As the dislocation moves, it stays mostly straight, although a slight wiggle of the end can be observed.

Figure 4.15 – Simulation of simplified hybrid dislocation

The simulation starts by adding a strong shear strain γ_l to the molecular dynamics domain including the pad,

$$\boldsymbol{u}^{+}(\boldsymbol{x}) = \begin{bmatrix} 1 & \gamma_l & 0 \\ 0 & 1 & 0 \\ 0 & 0 & 1 \end{bmatrix} \boldsymbol{x} + \boldsymbol{u}^{-}(\boldsymbol{x}), \tag{4.28}$$

where $\boldsymbol{u}^{-}(\boldsymbol{x})$ and $\boldsymbol{u}^{+}(\boldsymbol{x})$ are the displacement fields right before and after the start of the simulation. At the same time, a uniform shear stress τ_l is applied to the discrete dislocation dynamics domain

$$\boldsymbol{\sigma} = \begin{bmatrix} 0 & \tau_l & 0 \\ \tau_l & 0 & 0 \\ 0 & 0 & 0 \end{bmatrix} \tag{4.29}$$

The values of both γ_l and τ_l as well as the dislocation mobility have been fitted to one another using trial and error and have therefore no physical relevance.[12]

In the coupling step (Algorithm 4.2), the dislocation position in the crystal is determined by monitoring the displacements just above and below the slip plane and used to update the position of the constrained end nodes of the discrete dislocation line. Both end nodes are moved synchronously to emulate a crystal on either end of the line. The position of the dislocation nodes within the pad region are used to update the Volterra field on the entire pad.

Figure 4.15c shows a snapshot from the simulation soon after the start. Only the atoms of the central layer of the crystal are shown and coloured by x-displacement, blue being negative and red positive. The Peach-Koehler force acting on the dislocation nodes (white spheres) is indicated by the red arrows. The sharp transition from blue to red atoms in front of the dislocation indicates the cut plane of the edge dislocation. A velocity mismatch between the two domains has caused the end of the discrete dislocation to bow slightly forward and refine the line by splitting a few nodes. This mismatch, however, is small and the dislocation stays straight overall, as can be seen in Figure 4.15d, at the end of the simulation. The hybrid dislocation has successfully been propagated without getting pinned.

Note that this study merits to be repeated under more physical conditions as a final confirmation. Ideally, the study is performed under low applied stress with a core template.

---

[12] For this reason, their numerical values have been omitted here.

4.6 Coupled Frank-Read Source

This section describes work, which is – despite not having been completed yet – interesting, because it outlines the next milestone in the CADD development and shows that the current implementation is already capable of simulating cases that, because of their size, would be very difficult to handle in single scale molecular dynamics simulations and does so at greatly reduced computational cost.

A Frank-Read source (see, *e.g.* Hirth and Lothe, 1992, Chapter 20) in a cylindrical molecular dynamics domain has been chosen as a test case in which all components of CADD except for the dislocation detection/passing and hybrid dislocations can be tested. Figure 4.16a shows the general setup. A large cylindrical monocrystal of aluminium is modelled mostly by a finite-element domain Ω_{C} with a cylindrical molecular dynamics inclusion Ω_{A}. A prismatic dislocation loop acts as a double Frank-Read source.

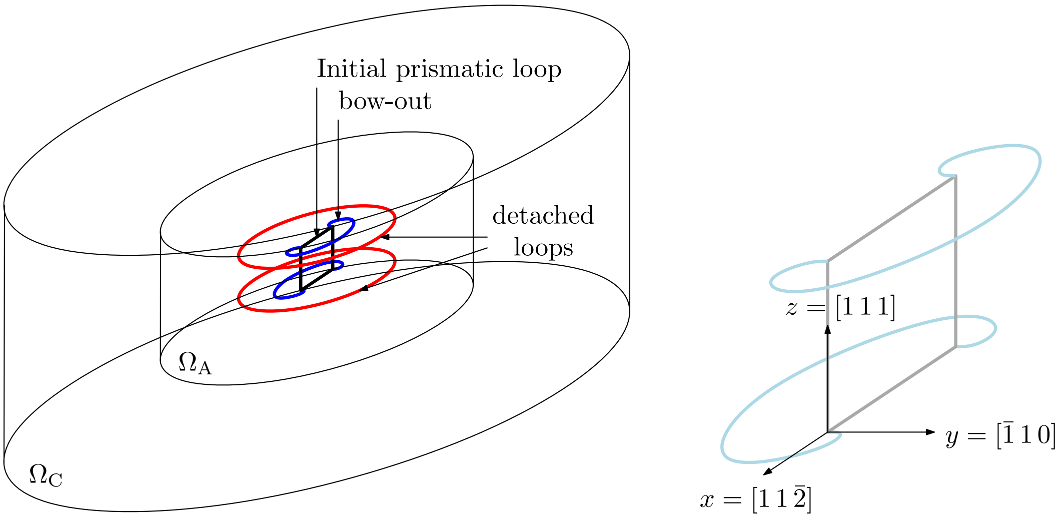

(a) Frank-Read source inside cylindrical molecular dynamics domain coupled to a continuum environment.

(b) Prismatic dislocation obtained by collapsed square vacancy in the plane $(\bar{1}\,1\,0)$

Figure 4.16 – Schematic of coupled Frank-Read source

The idea behind the test is best explained in the top view depicted in Figure 4.17. A Frank-Read source sheds concentric, roughly circular[13] dislocation loops. Dislocation loops that approach the cylindrical coupling interface can then be passed into the continuum at once, analogously to two-dimensional dislocation passing, by inserting a dipole loop, thus avoiding the complication of hybrid dislocations. This means that every continuous dislocation line is either completely modelled as an explicit discrete dislocation dynamics loop or is completely inside Ω_{A} as an implicit loop. The hope is that – following the argument of Section 4.1.1 and the authors of two-dimensional CADD

---

[13] Depending on the crystal system.

(see Shilkrot et al., 2004) – the error associated with the insertion of a dipole loop is small enough to not change the results in a significant way.

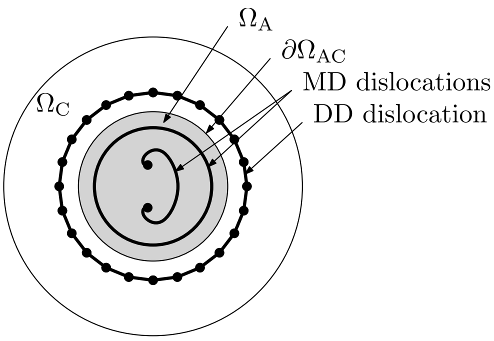

Figure 4.17 – Idealised coupled Frank-Read source. Concentric dislocation loops interact across the coupling interface $\partial\Omega_\mathrm{AC}$, but no hybrid dislocations occur.

The molecular dynamics domain Ω_A is modelled using the Mendelev et al. (2008) potential for aluminium and the finite-element domain Ω_C uses an anisotropic linear elastic constitutive law fitted to the potential. The loop is obtained by cutting a square vacancy of thickness $\left\|\frac{1}{2}\left\langle 1\,1\,0\right\rangle\right\|$ out of a $\left(\bar{1}\,1\,0\right)$ plane, see Figure 4.16b for details on the lattice orientations. Subsequently, the vacancy is closed by straining the crystal in the vicinity. The forcibly closed vacancy serves as initial conditions for a molecular statics minimisation, resulting in a relaxed prismatic edge dislocation loop shown in Figure 4.18a.[14] The Burgers vector of this loop is $\frac{1}{2}\left[\bar{1}\,1\,0\right]$. Therefore, the horizontal top and bottom segments of the loop in $\left[1\,1\,\bar{2}\right]$ direction are on the $\left\{1\,1\,1\right\}\left\langle 1\,1\,0\right\rangle$ slip system, which is the major slip system in FCC (see Hirth and Lothe, 1992, Chapter 9). They have dissociated into Shockley partials and are relatively mobile. The vertical segments along the $\left[1\,1\,1\right]$ direction, however, retained compact cores and should be relatively sessile as they do not correspond to a slip system known to occur in FCC crystals.

The cylindrical disk of the molecular dynamics domain is coupled to a finite-element domain on its entire boundary, as depicted in Figure 4.18c. Parts of the MD mesh are omitted in the figure to allow a view onto the enclosed molecular dynamics domain of which in turn half has been omitted to show the dislocation loop within it and its orientation. The bottom surface of the finite-element domain is blocked and a traction along the y axis is applied to the top surface with the lateral boundaries left free. Note that the mesh is fully refined at the pad. In the system depicted in Figure 4.18c, the molecular dynamics domain boundary has a radius and height of $r_\mathrm{A} = h_\mathrm{A} = 100$ Å (not including the pad) and the finite-element domain boundary is $r_\mathrm{C} = h_\mathrm{C} = 500$ Å. Overall, it contains $N_\mathrm{at} = 260093$ atoms and $N_\mathrm{el} = 435765$ elements with $N_\mathrm{nd} = 113946$ nodes. If the system were modelled in pure molecular dynamics, it would contain roughly $N_\mathrm{eq} = 26 \times 10^6$ atoms. Since the vast majority of the elements are actually inside the pad, increasing the size of the finite-element part of the problem, even significantly, comes at

---

[14] A similar geometry is studied by de Koning et al. (2003) in a small molecular dynamics study.

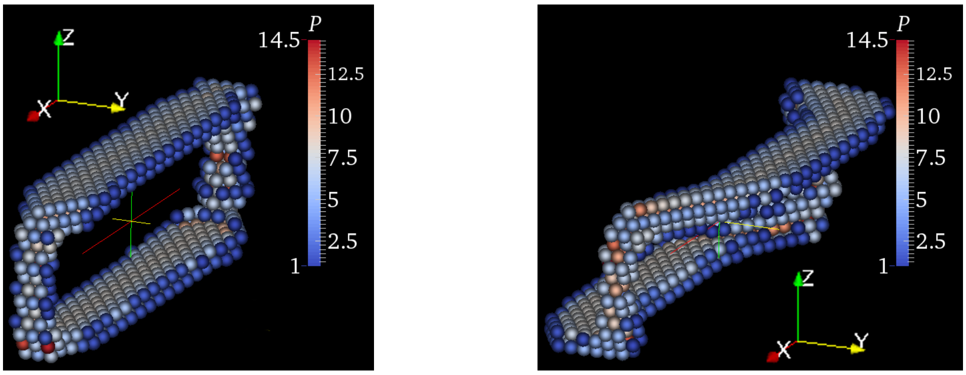

(a) Relaxed collapsed vacancy, only atoms with a centrosymmetry parameter $P > 1$ are represented. Note that the mobile horizontal segments of the loop dissociate into partials while the sessile vertical segments retain compact cores.

(b) Visualised source with slight bow-out under load.

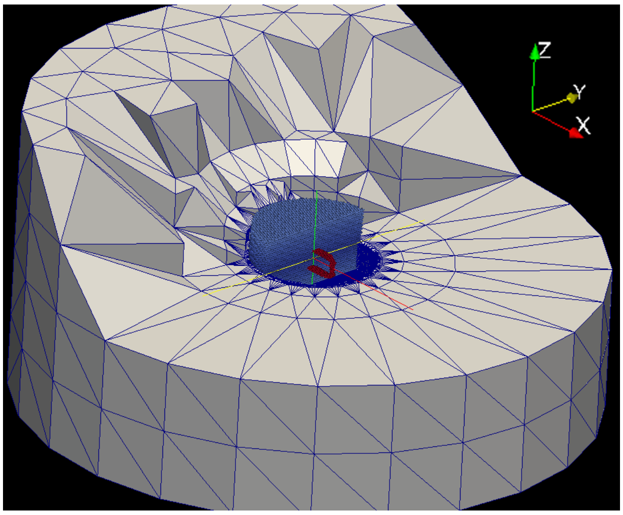

(c) Full simulated system. Parts of the finite-element mesh (grey elements) have been cut away to reveal the cylindrical molecular dynamics domain (blue atoms) of which again half is cut away to show the orientation of the dislocation loop (red atoms).

Figure 4.18 – Simulation setup for Frank-Read source

an almost negligible increase of computational cost.

At the current state of development, the Frank-Read source fails to open under smooth loading. Figure 4.19 shows the situation. Only atoms with a centrosymmetry parameter $P > 1$ are shown. The white atoms correspond to the coupled source after $t = 23.25$ ps under a shear load of $\tau_{yz} = 1.2$ GPa. The blue atoms correspond to a reference source, which has been obtained by shock-loading the un-collapsed vacancy with the same load and depicts the situation $t = 5.2$ ps after the shock wave impacts the source. One can see that the vertical segments of the initial source do not remain sessile under smooth loading, instead they glide on the $(1\,1\,\bar{2})$ plane and thus prevent the bow-out of the mobile top and bottom segments from forming closed loops. The shock-loaded vacancy, on the other hand, nucleates two dislocation loops without getting destroyed.

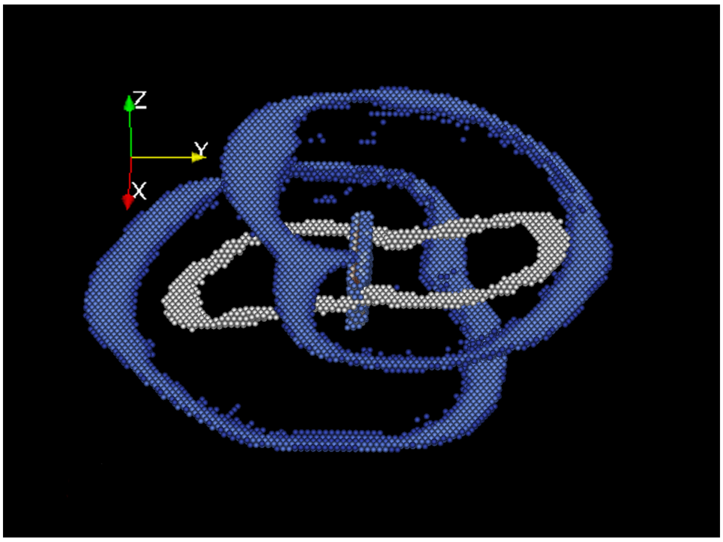

Figure 4.19 – Frank-Read source fails to open correctly. Only atoms with centrosymmetry parameter $P > 1$ are shown. The blue atoms are part of dislocations emitted from the shock-loaded vacancy visible in the centre, while the white atoms depict the failing smoothly loaded loop.

The reason behind the failing of the source has not yet been thoroughly investigated, and no speculations as to the reasons behind the failure are presented here. Instead, let us look at the computational efficiency of the implementation. Table 4.2 compares some performance indicators for the problem presented here to a molecular dynamics problem of the same spatial volume. It can be seen that the coupling has reduced the number of degrees of freedom by about a factor of 70 and the memory use by a factor of about 4. On a single core, the coupled problem runs 28.1 times faster than the reference case. It appears that the main objective of multiscale modelling, the decrease in computational cost in order to simulate larger domains or longer time scales is achieved by the currently developed implementation of CADD. Note that while these comparisons have been made

	MD	coupled
degrees of freedom	78 018 480	1 122 117
memory used	9.683 GiB	2.543 GiB
sequential steps/second	0.012	0.34
sequential speedup	1	28.1

Table 4.2 – Comparison between full molecular dynamics and coupled performance. The sequential runs were performed on the same Intel Xeon processor.

for sequential runs of the test cases, our implementation also runs in parallel.

4.7 Conclusions

In this chapter, the main differences between two- and three-dimensional CADD have been presented to highlight the obstacles to a complete three-dimensional CADD implementation. A road map has been established that addresses each of the obstacles and aims at the efficient and parallel realisation of three-dimensional CADD. The plan uses the multiscale coupling framework LibMultiscale and several other open-source software projects to keep the development effort low without compromising performance. For every milestone of the road map, a test case is proposed.

The foundations of the plan have been implemented and the corresponding test cases have been presented. A fundamental contribution to the development of CADD – its general dynamic instability – has been discovered. The discussion of the stability issues, however, applies generally to displacement coupling methods and is therefore treated apart in the next chapter.

5 Dynamic Stability of Ghost Force-Free Atomistic/Continuum Coupling Methods

This chapter is the modified version of a manuscript that has been submitted for publication and is in review as of the writing of this thesis.

As discussed earlier, atomistic methods such as molecular dynamics are powerful tools in the investigation of nanoscale contact and other physical phenomena at the nanoscale and help understand and predict behaviour at scales too small to be accurately described by continuum methods (Luan and Robbins, 2005). The very short time steps of the order of femtoseconds and high memory requirements of molecular dynamics, however, severely limit its usefulness in the investigation of slow phenomena or large problems.

These high computational costs motivate the development and use of concurrent multiscale methods. Examples include the several methods presented in Section 2.4, in which only a small part of the computational domain – where strongly nonlinear atomic-scale phenomena are expected to occur – is resolved atomistically. The better part of the domain is treated using coarser, computationally cheaper continuum methods such as the finite-element method in order to reduce the number of degrees of freedom of the problem by minimising the number of atoms taken into account.

It has been explained that one main distinguishing factor between different coupling methods is the governing formulation. Some methods, such as QC, have a well-defined potential energy functional (Hamiltonian). These methods have good energy conservation properties, but generally suffer from ghost forces near the interface, see for instance the review by Curtin and Miller (2003) or Miller and Tadmor (2009) for a detailed discussion. Mobile defects such as dislocations are particularly sensitive to ghost forces. Other methods, such as CADD or FEAt abandon a well-defined Hamiltonian to get rid of the ghost forces by coupling displacements, therefore essentially treating coupled domains as separate problems that provide each other's boundary conditions.

In this chapter, we use the example of CADD to analyse the dynamics of displacement coupling methods in detail and show that they are generally unstable. Particularly, we explain that they are generally unsuitable for dynamic problems at high temperatures.

The chapter is organised as follows. Displacement coupling is explained in Section 5.1 using the example of CADD and some pertinent previous work. A one-dimensional coupled model case is used to demonstrate the instability inherent to displacement coupling methods and the influence of the initial temperature is discussed. Section 5.2 analyses the observed instability from a theoretical point of view using a further reduced one-dimensional model. In Section 5.3, we discuss several approaches to manage the instability by modifying the dynamics and the coupling scheme, including a novel approach that achieves stable, ghost force-free displacement coupling.

5.1 Instability in Displacement Coupling (CADD): Numerical Examples

5.1.1 CADD Revisited

As mentioned in Section 2.4, CADD couples a fully atomistic domain to an elastic continuum with discrete dislocations. The method has four distinct parts: an atomistic domain, a continuum domain with discrete dislocations, a coupling scheme and an algorithm to pass dislocations between the domains. Because we analyse the dynamic stability of CADD and the passing of dislocations across the interface has no stability implications, we concentrate only on CADD's continuum-atomistics coupling scheme.

CADD was first introduced in Shilkrot et al. (2002a), but the original formulation was shown to lead to an artificially increased coupling interface stiffness in Curtin and Miller (2003). A revised displacement-based coupling for CADD was subsequently presented in Shilkrot et al. (2004). In this chapter we use the revised CADD method as an example case for displacement coupling.

The coupling is performed by synchronising displacements across a sharp interface, shown schematically in Figure 5.1. The interface atoms coincide with the boundary nodes of the finite-element mesh; they are regular atoms subject to the interatomic potential. Their displacements are imposed as Dirichlet boundary conditions on the boundary nodes of the finite-element mesh. The pad atoms are attached to the finite elements and move with them. They serve as boundary condition for the molecular dynamics problem and may, but do not have to, coincide with finite-element nodes.

CADD has been used to study several phenomena such as dislocation emission from crack tips, void growth or nanoindentation in quasistatic (zero temperature) problems (Shilkrot et al., 2004), fully dynamic problems at finite temperature (Shiari et al., 2005) and intermediate problems where finite temperature atomistics is coupled to quasistatic discrete dislocations (Qu et al., 2005). To the best of our knowledge, only plane strain

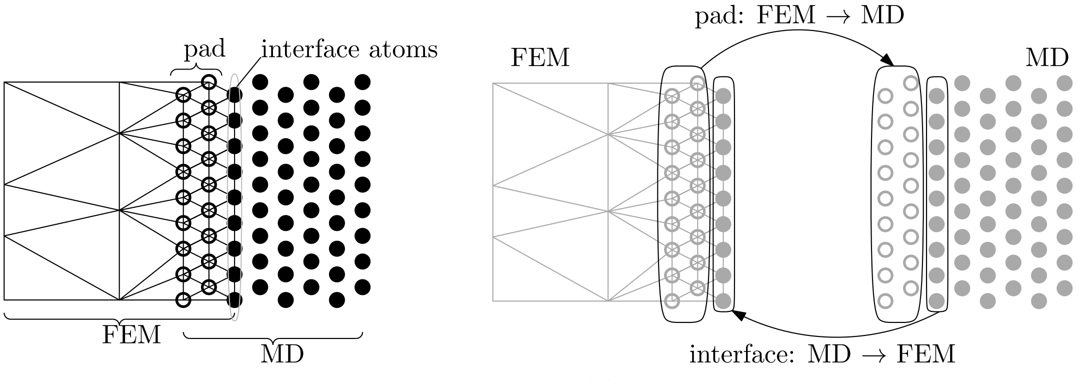

(a) Coupled problem (b) Split, separated representation

Figure 5.1 – Sharp interface coupling in CADD. The left (continuum) half of the domain is discretised using the finite-element method, the right side is treated with full atomistic resolution using molecular dynamics. The interface atoms (in the grey ellipse in Figure 5.1a) coincide with the boundary nodes of the finite-element mesh and their displacements are used as Dirichlet boundary conditions for the continuum (lower arrow in Figure 5.1b). The atoms in the pad may or may not coincide with finite-element nodes. They are moved by the finite-element method and provide the boundary conditions for the atomistic problem (upper arrow in Figure 5.1b).

implementations of the CADD method exist.

5.1.2 Instability of the One-Dimensional Problem

In this section, we present a simple dynamic model problem and show that it is dynamically unstable, particularly at high temperatures and look at some of the influencing factors. The one-dimensional example case used here has $n_d = 50$ degrees of freedom of which the first 25 are finite-element nodes (including the interface node). A schematic of the system is shown in Figure 5.2. The circles represent finite-element nodes and the crosses molecular dynamics atoms. The interface and pad atoms have overlaid circles and crosses. For simplicity, we use a Lennard-Jones potential for the atomistics that matches the elastic properties of the finite-element mesh, see Appendix A for details on the matching. All simulation results in this section are reported in dimensionless reduced Lennard-Jones units, making the numerical values of the simulation parameters arbitrary and irrelevant.

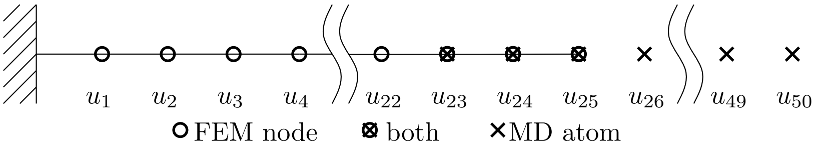

Figure 5.2 – Schematic of one-dimensional test case.

The initial conditions impose a zero initial displacement $\boldsymbol{u}(0) = \boldsymbol{0}$ and the initial velocity

$\boldsymbol{v}(0)$ corresponding to a given reduced initial temperature[1] $T^*(0) = T_0^*$,

$$
\begin{aligned}
&E_{\text{kin}}(0) = \frac{T_0^* \epsilon}{2} = \sum_{i=1}^{n_d} \tfrac{m}{2} v_i^2, \\
&\rightarrow v_i(0) = (-1)^i \sqrt{\frac{T_0^* \epsilon}{m}}.
\end{aligned}
\tag{5.1}
$$

Note that this is not an equilibrium distribution, and that the initial regime, in which the temperature settles down to about half of the initial temperature as the system trades kinetic for potential energy cannot be trusted to behave thermodynamically fully correctly. However, the time needed for the system to become unstable is several orders of magnitude larger than the time it takes for the temperatures to settle in all our simulations.

Integration in time is performed with the widely-used velocity-Verlet scheme (Griebel et al., 2007). In order to avoid additional stability issues due to this scheme, we use a safe, very conservative integration time step Δt based on the approximate shortest oscillation period τ_{min} in the system. The Lennard-Jones potential is linearised as described in Appendix A and the global stiffness matrix $\mathbf{K}$ of the system assembled. Now, τ_{min} is

$$
\tau_{\text{min}} = 2\pi \frac{m}{\lambda_{\text{max}}},
\tag{5.2}
$$

where m is the atomic/nodal mass and λ_{max} the largest eigenvalue of $\mathbf{K}$. Both $\Delta t = \frac{\tau_{\text{min}}}{25}$ and $\Delta t = \frac{\tau_{\text{min}}}{50}$ are used in the following simulations and the cutoff distance of the Lennard-Jones potential is varied as to incorporate only first, first and second, or up to third neighbour interactions.

Figure 5.3 shows the evolution of the temperature for $T_0^* = 0.1$ and different choices of Δt and the number of neighbour interactions N_{neigh} considered. We observe an exponential increase of the temperature until roughly around $t^* = 500$ where the fluctuations become very strong. The melting point of Lennard-Jonesium at zero pressure is around $T_m^* \approx 0.7$ (Mastny and de Pablo, 2007), coinciding with this onset of strong fluctuations. Once the temperature comes close to or exceeds T_m^*, the simulation results should no longer be considered physical, because we do not recompute neighbour lists. We will therefore concentrate our observations in all simulations on the initial regime, before the coupling instability takes the temperature close to the melting point.

Figure 5.3a shows the evolution of T^* for two different time steps. While the temperatures

---

[1] The dimensionless reduced temperature is given by $T^* = T\frac{k_{\text{B}}}{\epsilon}$, where k_{B} is Boltzmann's constant, and reduced time is given by $t^* = t\sqrt{\frac{\epsilon}{m\sigma}}$. The energy ϵ and the distance σ are parameters of the Lennard-Jones potential and are derived in Appendix A.

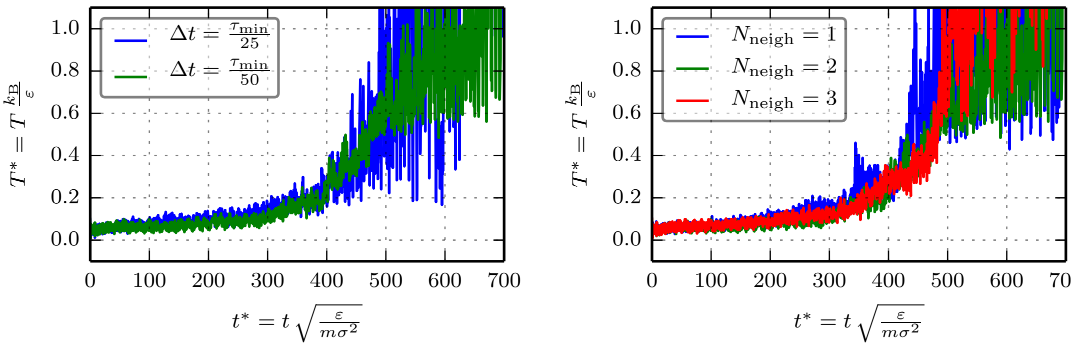

(a) Time step-independent behaviour of instability. First and second neighbour interactions are considered ($N_{\text{neigh}} = 2$).

(b) Interaction range-independent behaviour of instability. $\Delta t = \frac{\tau_{\min}}{50}$.

Figure 5.3 – Evolution of temperature for $T_0^* = 0.1$

fluctuate significantly more for the longer time step, the mean increase and divergence of T^* appear insensitive to Δt. The influence of the cutoff radius of the interatomic potential can be seen in Figure 5.3b, where the evolution of T^* is shown for first neighbour interaction only ($N_{\text{neigh}} = 1$), first and second ($N_{\text{neigh}} = 2$) as well as first, second and third neighbour interaction ($N_{\text{neigh}} = 3$). Save for the fluctuations, the evolution of the instability appears insensitive to the potential cutoff radius as well. This indicates that the instability does not stem from an integration or interatomic potential issue.

It is important to point out that the curves shown in Figure 5.3 all collapse onto one another because the simulations start at a moderate temperature. When starting from very low temperatures, where the system is close to the linearised model, the time it takes for the temperature to diverge becomes more sensitive to details such as initial conditions, time step or cutoff radius. Figure 5.4 shows the same analysis as in the previous section, but for much lower starting temperatures.

Figures 5.4a, 5.4b show the influence of Δt and N_{neigh} on the duration of the unstable transition. We observe that the curves (until they reach temperatures closer to T_m^*) appear to diverge in a similar manner. Figure 5.4c shows the exact same results as Figure 5.4b, but the time axes have been shifted as to make the curves collapse, and they match perfectly.

We propose the following explanation for the significant variations in the divergence time when starting from very low temperatures: at very low T_0^*, the system is very close to its linear approximation, and the relative displacements of the pad interface atoms remain mostly in a small range, where the traction-compression asymmetry of the interatomic potential – which we will show to be the root cause of the instability in Section 5.2.2 – is negligible. From time to time, statistical fluctuations push these displacements into the asymmetric range, resulting in a small surge of excess energy. With each of these rare

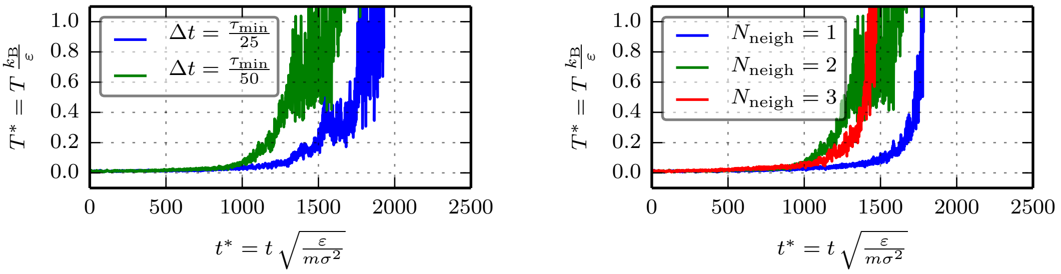

(a) Influence of time step at $T_0^* = 0.02$, $N_{\text{neigh}} = 2$

(b) Influence of number of neighbours taken into account at $T_0^* = 0.02$, $\Delta t = \frac{\tau_{\min}}{50}$

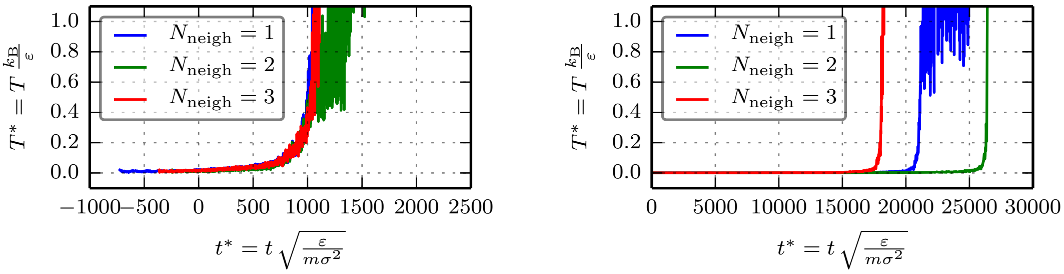

(c) Results of Figure 5.4b on a shifted time axis.

(d) Influence of number of neighbours taken into account at $T_0^* = 0.002$

Figure 5.4 – Sensitivity on details at low temperatures.

events, the energy of the system increases a bit, making the reoccurrence of such an event more likely (i.e., frequent). For higher values of T_0^*, the system starts immediately in the asymmetric range and the instability is not fuelled by statistically extreme (i.e. rare) but by average, continuously occurring events. By their nature, rare events are much more sensitive to small variations in the system, such as Δt and N_{neigh}. Figure 5.4d shows the evolution starting from an even lower temperature $T_0^* = 0.002$ where the differences in divergence time are even more pronounced. Note also that the order in which the three systems diverge is not the same as in Figure 5.4b, indicating that it is not the number of neighbours taken into account that makes the system diverge faster or slower, but the initial conditions. This appears to support our proposed explanation.

We do not pursue these observations further, since they are quite particular to one-dimensional systems, which have only a single interface atom and N_{neigh} pad atoms (which are the only nodes/atoms contributing to the instability), whereas two and three-dimensional systems have large numbers of them, thus making the "rare events" much more common.

5.2 Stability Analysis

Proving or refuting the stability of displacement coupling methods such as CADD in a general case is difficult, if not impossible, because of the nonlinear empirical nature of interatomic potentials and the shear number of degrees of freedom involved. To simplify our analysis, we define a simplified one-dimensional case with only a few degrees of freedom and a Lennard-Jones potential with second neighbour interaction.

In this section, we demonstrate that the observed instability is due to the asymmetric traction-compression behaviour of the interatomic potential. First, we show that the linearised problem and its velocity-Verlet discretisation in time are stable and then present an unstable, further simplified problem with asymmetric, piece-wise linear springs.

5.2.1 Simple One-Dimensional Displacement Coupling Case

Figure 5.5 shows the schematic of a simple, one-dimensional displacement coupling problem with six degrees of freedom. From left to right we see

- one regular finite-element node, linked to a clamp by a spring,
- two pad atoms or nodes,
- the interface atom or node and
- two free atoms.

The asymmetric force interactions across the interface are visualised by the directional spring symbols with arrow heads. For instance the interface atom “feels” a force due to the spring k_1 from the closest pad node, while that node feels a force due to the spring k from the interface atom. This force asymmetry violates Newton’s Third Law.

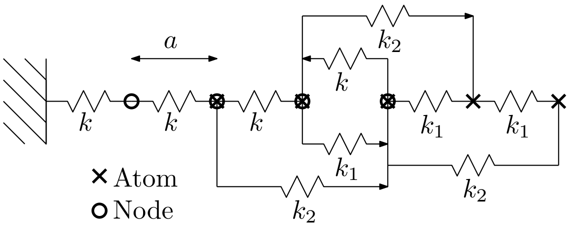

Figure 5.5 – Schematic of a small 1D CADD case. Note that the directional springs (with arrows) act only in one direction. They are responsible for the non-Newtonian mechanics of the coupled system. The interatomic spacing a and the continuum stiffness k are given, the stiffnesses k_1 and k_2 depend on a and k.

The springs k_1 and k_2 represent the first and second neighbour interaction due to the Lennard-Jones potential and are therefore nonlinear. In this section, we will compare the nonlinear case to the linearised problem in which the i-th neighbour spring is $k_i = \alpha_i k$ with

$$\alpha_1 = 1.2209, \qquad \alpha_2 = -0.0052260. \tag{5.3}$$

The details of the linearisation and the derivation of the α_i coefficients can be found in Appendix A. The linearised system can be represented as a matrix equation

$$m\ddot{\boldsymbol{u}} + \mathbf{K}\boldsymbol{u} = \mathbf{0}, \tag{5.4}$$

where m is the atomic mass, $\boldsymbol{u}$ the displacement vector and $\mathbf{K}$ the stiffness matrix given by

$$\mathbf{K} = k \begin{bmatrix} 2 & -1 & 0 & 0 & 0 & 0 \\ -1 & 2 & -1 & 0 & 0 & 0 \\ 0 & -1 & 2 & -1 & 0 & 0 \\ 0 & -\alpha_2 & -\alpha_1 & 2\alpha_1 + 2\alpha_2 & -\alpha_1 & -\alpha_2 \\ 0 & 0 & -\alpha_2 & -\alpha_1 & 2\alpha_1 + \alpha_2 & -\alpha_1 \\ 0 & 0 & 0 & -\alpha_2 & -\alpha_1 & \alpha_1 + \alpha_2 \end{bmatrix}. \tag{5.5}$$

The system is stable if the real parts of the eigenvalues real(λ_i) of $\frac{1}{m}\mathbf{K}$ are not negative. This particular system has the eigenvalues

$$\begin{aligned} &\lambda_1 = 0.0581\tfrac{k}{m}, \quad \lambda_2 = 0.5037\tfrac{k}{m}, \quad \lambda_3 = 1.2961\tfrac{k}{m}, \\ &\lambda_4 = 2.2529\tfrac{k}{m}, \quad \lambda_5 = 3.1598\tfrac{k}{m}, \quad \lambda_6 = 3.7990\tfrac{k}{m}, \end{aligned}$$

which are distinct, real and positive. The linearised system is therefore stable. Note that this is the case independently of the choice of k and m (provided they are positive). Furthermore note that $\mathbf{K}$ is asymmetric (because of the non-Newtonian interactions) but that this asymmetry does *not* result in instability.

Discretisation in Time The integration in our simulations is performed using the velocity-Verlet scheme, as is done commonly in molecular dynamics (Plimpton, 1995; Griebel et al., 2007). Algorithm 5.1 shows the scheme applied to a linear system as described by (5.4) for given initial displacements $\boldsymbol{u}_0$, velocities $\boldsymbol{v}_0$ and time t_0 and a given time step Δt.

After defining a state vector $\boldsymbol{x}$

$$\boldsymbol{x} = \begin{bmatrix} \boldsymbol{u} \\ \dot{\boldsymbol{u}} \end{bmatrix}, \tag{5.6}$$

we can write the discretised system as a discrete state-space system (Zadeh and Desoer,

Algorithm 5.1 Velocity-Verlet scheme for a linear system

```
$\ddot{\boldsymbol{u}} \leftarrow -\frac{1}{m}\mathbf{K}\boldsymbol{u}$    ▷ Initial conditions $\boldsymbol{u} = \boldsymbol{u}_0$, $\dot{\boldsymbol{u}} = \boldsymbol{v}_0$, $t = t_0$, $i = 0$
while $t < t_{\text{end}}$ do
    $t \leftarrow t + \Delta t$
    $i \leftarrow i + 1$
    for all particles do
        1.) $\dot{\boldsymbol{u}}_{i+1/2} \leftarrow \dot{\boldsymbol{u}}_i - \frac{\Delta t}{2m}\mathbf{K}\boldsymbol{u}_i$
        2.) $\boldsymbol{u}_{i+1} \leftarrow \boldsymbol{u}_i + \Delta t\, \dot{\boldsymbol{u}}_{i+1/2} = \left[\mathbf{I} - \frac{\Delta t^2}{2m}\mathbf{K}\right] \boldsymbol{u}_i + \Delta t\, \dot{\boldsymbol{u}}_i$
        3.) $\ddot{\boldsymbol{u}}_{i+1} \leftarrow -\frac{1}{m}\mathbf{K}\boldsymbol{u}_{i+1} = -\frac{1}{m}\mathbf{K}\left[\mathbf{I} - \frac{\Delta t^2}{2m}\mathbf{K}\right] \boldsymbol{u}_i - \frac{\Delta t}{m}\mathbf{K}\dot{\boldsymbol{u}}_i$
        4.) $\dot{\boldsymbol{u}}_{i+1} \leftarrow \dot{\boldsymbol{u}}_{i+1/2} + \frac{\Delta t}{2}\ddot{\boldsymbol{u}}_{i+1} = \frac{\Delta t}{2m}\mathbf{K}\left[\frac{\Delta t^2}{2m}\mathbf{K} - 2\mathbf{I}\right] \boldsymbol{u}_i + \left[\mathbf{I} - \frac{\Delta t^2}{2m}\mathbf{K}\right] \dot{\boldsymbol{u}}_i$
    end for
end while
```

2008)

$$\boldsymbol{x}_{i+1} = \underbrace{\begin{bmatrix} \mathbf{I} - \frac{\Delta t^2}{2m}\mathbf{K} & \Delta t\mathbf{I} \\ \frac{\Delta t}{2m}\mathbf{K}\left[\frac{\Delta t^2}{2m}\mathbf{K} - 2\mathbf{I}\right] & \mathbf{I} - \frac{\Delta t^2}{2m}\mathbf{K} \end{bmatrix}}_{\mathbf{\Phi}(\Delta t)} \boldsymbol{x}_i \tag{5.7}$$

Such a system is stable if all eigenvalues λ_i of the transition matrix $\mathbf{\Phi}(\Delta t)$ are within the open complex unit disk $\max(||\lambda_i||) \leq 1$ (Zadeh and Desoer, 2008). For a given system (i.e., for a given mass m and stiffness matrix $\mathbf{K}$), the eigenvalues λ_i of $\mathbf{\Phi}$ depend on the chosen time step Δt. We state without proof that a critical time step Δt_{crit} exists for which

$$\max(||\lambda_i(\Delta t)||) \leq 1 \quad \forall \Delta t \in [0, \Delta t_{\text{crit}}], \tag{5.8}$$

for such a linearised system and which can simply be found numerically.

Figure 5.6 shows the evolution of the temperature T^* of the system depicted in Figure 5.5 (blue) and compares it to its linearised version (green) and the corresponding uncoupled full molecular dynamics case (red). The numerical parameters are listed in Table 5.1. The critical stable time step Δt_{crit} of the system has been estimated with a precision of 10^{-8} by simple bisection and the integration time step has been arbitrarily chosen to be $\Delta t = \frac{1}{3}\Delta t_{\text{crit}}$. The reduced initial temperature is imposed by applying an initial velocity field corresponding to T_0^* quickly resulting in a mean temperature of $\frac{1}{2}T_0^*$. The values of the numerical parameters k, a and m are irrelevant, since results are reported in dimensionless reduced units.

All three systems stay around $\frac{1}{2}T_0^*$ until about $t^* = 10000$, when the nonlinear coupled system starts to be distinctively hotter than the others and at about $t^* = 15000$ it clearly diverges while both the full molecular dynamics and the linearised coupled problem

parameter	value	description
k	1.2	spring stiffness
a	1.4	interatomic spacing
m	2.21	atomic mass
n_{neigh}	2	no. of neighbour interactions
Δt	0.464	integration time step
T_0^*	0.02	reduced initial temperature

Table 5.1 – Parameters of numerical application. The units system is irrelevant since all results are presented in dimensionless form. The time step has been chosen as $\frac{1}{3}$ of the stable time step of the linearised system.

remain stable. Therefore, the source of the instability cannot be explained by properties of the linearised system. The origin of the instability lies in the nonlinearity of the interactions in the coupling scheme.

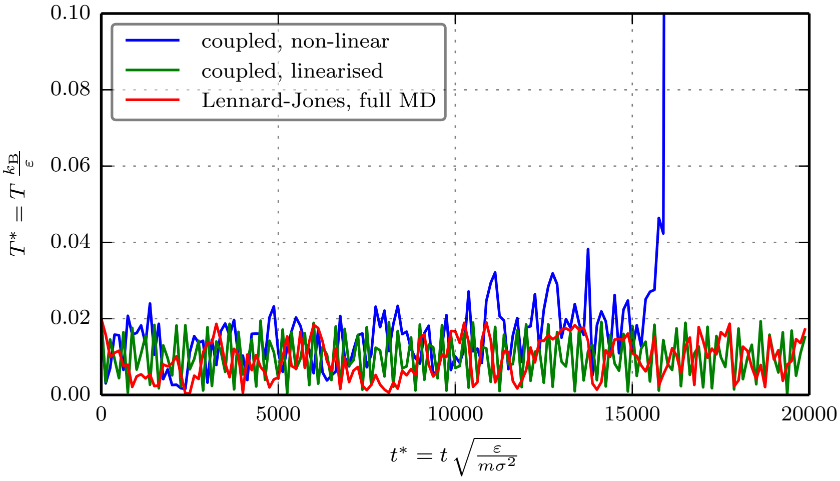

Figure 5.6 – Comparison between linearised (green) and nonlinear (blue) coupled system. The uncoupled, full Lennard-Jones case (red) is represented as reference. Both the full Lennard-Jones system and the linearised system are stable, while the nonlinear coupled system becomes unstable around $t^* = 15000$.

5.2.2 Simplified Model with Traction-Compression Asymmetry

We claim that the instability is due to the asymmetric traction-compression behaviour of interatomic potentials. We explore this idea with a further simplified system, schematically shown in Figure 5.7a, that exhibits such a traction-compression asymmetry. Two masses m are linked by the springs k_1 and k_2. The springs act only in one direction, mimicking the non-Newtonian mechanics of the coupled system where the force exerted by the left mass onto the right one $f_{\text{l}\to\text{r}}$ is not the equal opposite of the force exerted by the right mass on the left one $f_{\mathrm{r}\to\mathrm{l}} \neq -f_{\mathrm{l}\to\mathrm{r}}$. The asymmetric traction-compression behaviour of interatomic potentials is emulated in spring $k_2(\mathrm{sgn}(\Delta u))$ by making the stiffness dependent on the sign of the relative displacement $\Delta u = u_2 - u_1$ between the two masses, see Figure 5.7b,

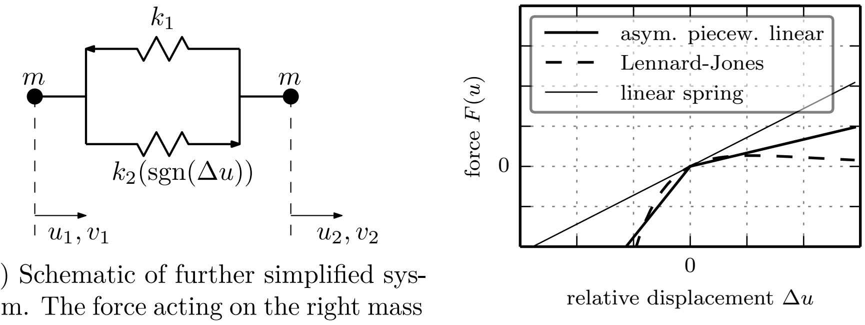

(a) Schematic of further simplified system. The force acting on the right mass depends on the asymmetric spring k_2, the force on the left mass on k_1.

(b) An asymmetric, piece-wise linear spring $k_2(\mathrm{sgn}(\Delta u))$ mimicks the asymmetry of the Lennard-Jones potential.

Figure 5.7 – Simplified system with asymmetric traction-compression behaviour

$$k_2 = \begin{cases} k_2^- & \text{if } \Delta u < 0 \\ k_2^+ & \text{else.} \end{cases} \tag{5.9}$$

For simplicity, we will write $k_2(\boldsymbol{u})$ instead of $k_2(\mathrm{sgn}(\Delta u))$. This nonlinear system is very convenient for our analysis because it has only one eigenmode with non-zero eigenfrequency. More importantly, the oscillation period is independent of the amplitude, a feature usually reserved for linear systems. From here on, the exponents $(*)^+$ and $(*)^-$ will be used to denote quantities relating to the stretched and compressed state of the system, respectively.

The set of differential equations governing this system is

$$\begin{aligned} m\ddot{\boldsymbol{u}}_1 - k_1[u_1 - u_2] &= 0, \\ m\ddot{\boldsymbol{u}}_2 - k_2(\boldsymbol{u})[u_2 - u_1] &= 0, \end{aligned} \tag{5.10}$$

where the u_i's and v_i's are the displacements and velocities of the masses m. We represent the system as a continuous-time state-space system (Zadeh and Desoer, 2008) by defining the state vector $\boldsymbol{x}$

$$\boldsymbol{x} = \begin{bmatrix} u_1 & u_2 & v_1 & v_2 \end{bmatrix}^{\mathrm{T}}, \tag{5.11}$$

and substituting (5.10). The evolution of the state is

$$\dot{\boldsymbol{x}} = \boldsymbol{f}(\boldsymbol{x}) = \begin{bmatrix} v_1 \\ v_2 \\ -\frac{1}{m}k_1[u_1 - u_2] \\ -\frac{1}{m}k_2(\boldsymbol{u})[u_2 - u_1] \end{bmatrix} = \underbrace{\begin{bmatrix} 0 & 0 & 1 & 0 \\ 0 & 0 & 0 & 1 \\ -\frac{k_1}{m} & \frac{k_1}{m} & 0 & 0 \\ -\frac{k_2(\boldsymbol{u})}{m} & \frac{k_2(\boldsymbol{u})}{m} & 0 & 0 \end{bmatrix}}_{\mathbf{A}(\boldsymbol{u})} \boldsymbol{x}. \tag{5.12}$$

When the system is in either traction or compression, it behaves as a linear time-independent system and only the transitions between those two states are nonlinear. Therefore, it oscillates by spending half an oscillation period of the stretched system T^+, followed by half a period of the compressed system T^-. The angular frequencies of system (5.12) in *either* the stretched *or* the compressed state are given by the eigenvalues λ_i of $\mathbf{A}(\boldsymbol{u})$ (Bellman, 1969),

$$\lambda_{1,2} = 0, \qquad \lambda_{3,4} = \pm\sqrt{\frac{k_1 + k_2(\boldsymbol{u})}{m}}\boldsymbol{i} = \pm\omega\boldsymbol{i}, \tag{5.13}$$

where ω is the only non-zero angular frequency of the system and $\boldsymbol{i}$ the imaginary unit. The zero eigenvalues λ_1 and λ_2 correspond to solid body motion and are of no concern here. Note that all the real parts of all eigenvalues are zero. The compressed and the stretched system are therefore individually stable (unsurprisingly). We denote the angular frequency of the stretched and the compressed system by ω^+ and ω^-, respectively, and do the same for the system matrices $\mathbf{A}^+$ and $\mathbf{A}^-$. The oscillation period T of the system is therefore

$$T = \tfrac{1}{2}\left[T^+ + T^-\right] = \pi\left[\frac{1}{\omega^+} + \frac{1}{\omega^-}\right] \tag{5.14}$$

The solution to (5.12) is (Zadeh and Desoer, 2008)

$$\boldsymbol{x}(t) = \underbrace{\exp\left(\int_{t_0}^{t} \mathbf{A}(\boldsymbol{u}(\tau))\mathrm{d}\tau\right)}_{\boldsymbol{\Phi}(t_0,t)} \boldsymbol{x}(t_0), \tag{5.15}$$

if $\int_{t_0}^{t} \mathbf{A}(\boldsymbol{u}(\tau))\mathrm{d}\tau$ and $\mathbf{A}(\boldsymbol{u}(t))$ commute for all t, in which case the matrix $\boldsymbol{\Phi}(t_0, t)$ is the state transition matrix.

The system matrices $\mathbf{A}^+$ and $\mathbf{A}^-$ do not commute. Therefore, the transition matrix that evolves the system by one full period $\mathbf{\Phi}_T = \mathbf{\Phi}(t_0, t_0 + T) = \mathbf{\Phi}_T$ has to be composed[2]

$$\begin{aligned} \mathbf{\Phi}_T = \mathbf{\Phi}_{T^+}\mathbf{\Phi}_{T^-} &= \exp\left(\int_{t_0}^{t_0+\frac{T^+}{2}} \mathbf{A}^+ \mathrm{d}\tau\right) \exp\left(\int_{t_0+\frac{T^+}{2}}^{t_0+T} \mathbf{A}^- \mathrm{d}\tau\right) \\ &= \exp\left(\tfrac{1}{2}\mathbf{A}^+ T^+\right) \exp\left(\tfrac{1}{2}\mathbf{A}^- T^-\right). \end{aligned} \tag{5.16}$$

Since the system allows solid body motion, the displacements are free to diverge and the system state is trivially unbounded. We wish to show however that the energy diverges, i.e. that v_1 and v_2 diverge. For this we define the output vector $\boldsymbol{y}$

$$\boldsymbol{y} = \begin{bmatrix} v_1 \\ v_2 \end{bmatrix} = \underbrace{\begin{bmatrix} 0 & 0 & 1 & 0 \\ 0 & 0 & 0 & 1 \end{bmatrix}}_{\mathbf{C}} \boldsymbol{x}. \tag{5.17}$$

After N_{cycle} periodic cycles, $\boldsymbol{y}$ is

$$\boldsymbol{y}(N_{\text{cycle}}) = \mathbf{C}\mathbf{\Phi}_T^{N_{\text{cycle}}} \boldsymbol{x}_0, \tag{5.18}$$

where $\boldsymbol{x}_0$ is the initial state. The output is bounded if and only if (Zadeh and Desoer, 2008) there exists a number M such that

$$\left|\left|\mathbf{C}\mathbf{\Phi}_T^{N_{\text{cycle}}}\right|\right| < M < \infty \qquad \forall N_{\text{cycle}} > 0. \tag{5.19}$$

Since the matrices $\mathbf{A}^+$ and $\mathbf{A}^-$ are neither commutative nor diagonisable (the geometric multiplicity of the eigenvalue 0 is 1), it is cumbersome to show analytically that the output in unbounded. For our purpose however, merely showing that the system is not stable *in general* with a counterexample suffices. Figure 5.8b shows the evolution of $\left|\left|\mathbf{C}\mathbf{\Phi}_T^{N_{\text{cycle}}}\right|\right|$ as a function of N_{cycle} using the numerical parameters listed in Table 5.8a. It clearly displays an instability.

While this does not constitute rigorous proof by any means, it shows that for all practical intents and purposes, displacement coupling between a linear model and one with a traction-compression asymmetry can lead to strong instabilities.

5.3 Strategies to Achieve Stability or Manage Instability

In this section we propose a few modifications to the coupling scheme in order improve its stability and discuss their implications. Keeping in mind that the main purpose of

---

[2] Here, we assume that the starting time t_0 is at the beginning of a compression period. Since we are interested in the long-term stability behaviour, this does not reduce the generality of the result.

parameter	value	description
k_1	2	stiffness 1
k_2^+	1.5	stiffness 2, traction
k_2^-	2.5	stiffness 2, compression
m	1.2	mass

(a) Example parameters for unstable asymmetric system

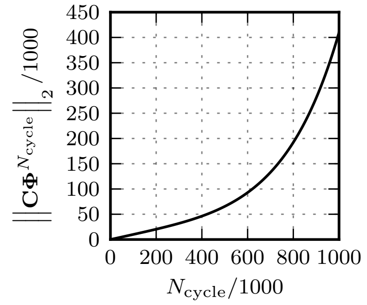

(b) Maximum singular value of $\mathbf{C\Phi}^{N_\text{cycle}}$ as a function of the number of cycles N_cycle

Figure 5.8 – Unstable example system

CADD is to propagate discrete dislocations in the continuum, we only present methods that retain linear elasticity in the continuum since the discrete dislocation dynamics method is based on linear superposition of stress fields.

In the following, we discuss two workarounds that modify the dynamics of the continuum and the atomistic domain, respectively, without changing the coupling scheme – the quasistatic continuum and thermostatting – and two strategies that modify the coupling scheme – force-coupling and a harmonic buffer layer. The harmonic buffer layer solves the problem fundamentally. All numerical examples presented in this section are simulations of the system defined in Section 5.1.2 and depicted in Figure 5.2, unless mentioned otherwise.

5.3.1 Quasistatic Continuum

While the original studies using CADD (Shilkrot et al., 2002b,a, 2004) examined fully quasistatic systems (molecular statics coupled to static finite elements), later studies such as Qu et al. (2005) coupled molecular dynamics to static finite-element assuming that dynamics in the continuum (far from nonlinear elastic effects) are slow enough to be neglected. In that case, the instability is trivially avoided because the absence of kinetic energy in the continuum prevents inertial effects in the dynamic interaction between the atomistic and the continuum domains. The obvious drawback of this method is that problems exhibiting dynamic phenomena in the entire simulation domain cannot be handled. Furthermore, the solution of the static finite-element problem is often computationally significantly more costly than explicit dynamics.

Figure 5.9a shows a comparison between regular dynamic coupling and quasi-static continuum coupling. It is clearly visible that the static continuum renders the system completely stable.

5.3.2 Thermostatting

Molecular dynamics simulations commonly employ thermostats in order to achieve or maintain prescribed temperatures. If predicting accurately the amount of energy dissipated by the system is of no concern, thermostatting can be used to prevent the instability. This works best at very low temperatures, where the excess heat energy rate is small (see exponential increase of T^* in Figures 5.3 and 5.4). With increasing temperature, the increased excess heat rate requires stronger thermostats. While this is unproblematic for some simulations such as damped dynamics, a too strong thermostat can modify or suppress dynamic processes such as dislocation motion.

As the excess heat generation is locally confined to the interface, spatially varying thermostats can reduce such effects. Shiari et al. (2005) used a global Nosé-Hoover thermostat to simulate two dimensional nanoindentation of aluminum at finite temperature in fully dynamic CADD and Qu et al. (2005) combined a locally applied Langevin thermostat with a quasi-static continuum to minimize wave reflection at the continuum/atomistic interface.

Figure 5.9b shows the impact of adding a thermostat to the system. We use a Langevin thermostat (Schneider and Stoll, 1978) as implemented in molecular dynamics codes such as LAMMPS (Plimpton, 1995) with two different values for the time constant[3] τ. Both the molecular dynamics and the finite-element domains are subject to the thermostat. The smaller time constant $\tau = 700$ (stronger thermostat) keeps the temperature close to the initial temperature. The larger constant $\tau = 1400$ (weaker thermostat) is not sufficient to prevent the temperature from rising and illustrates a bad choice of τ.

It is important to note that the thermostat has to be stronger than the ones used in full molecular dynamics simulations. How much stronger depends on the geometry and size of the coupling interface, mechanical load, temperature and likely the interatomic potential, thus making the choice of appropriate thermostat parameters a nontrivial issue.

5.3.3 Force-Coupling

Instead of coupling the atomistic and continuum domains using displacement boundary conditions, the domains could interact through symmetric non-local boundary tractions. All coupling points (the pad and interface atoms) move with the finite-element mesh and the interatomic forces between the bulk and coupling atoms are computed and applied to the continuum as nodal forces. The interatomic forces between coupling atoms are set to zero since their effect is taken into account by the finite-element calculation. This coupling type has the advantages that all force interactions are symmetric and therefore

---

[3] In dimensionless reduced Lennard-Jones time $t^* = t\sqrt{\frac{\epsilon}{m\sigma^2}}$.

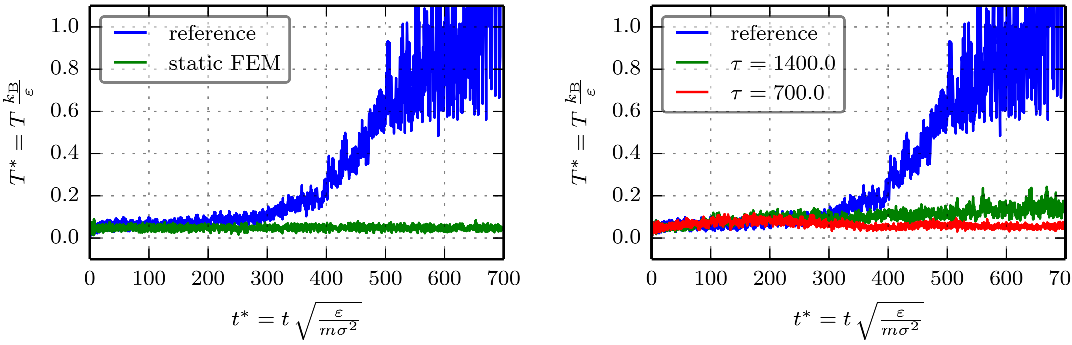

(a) CADD with statics in the continuum (green) does not suffer from instability. Dynamic CADD (blue) is shown as reference.

(b) Langevin thermostatted CADD compared to the dynamic CADD reference (blue). A weak thermostat (green) has a too large time constant τ to prevent an increase in temperature. An appropriate choice for τ (red) stabilises the system.

Figure 5.9 – Stability through modified dynamics. All simulations start at $T_0^* = 0.1$, consider interactions up to the second neighbour $N_{\text{neigh}} = 2$ and are discretised in time with $\Delta t = \frac{\tau_{\min}}{50}$.

stably integrable in time and that the Hamiltonian of the system is well defined. The drawback is that there are ghost forces analogous to those in the quasicontinuum method (Tadmor et al., 1996). Figure 5.11a compares force coupling to the regular displacement coupling. This coupling is very close to the original CADD formulation in Shilkrot et al. (2002a) or the QC method and therefore introduces the same spurious ghost forces (Curtin and Miller, 2003). Such ghost forces repel dislocations from the interfaces and make force-coupling unsuitable for CADD as a consequence.

5.3.4 Harmonic Buffer Layer

We have shown in Section 5.2.1 that a well defined Hamiltonian is not a necessary condition for stability. More specifically, linearised displacement coupling is stable. By introducing a layer of harmonic atoms (linear interatomic interaction through quadratic potentials) thicker than the cutoff radius of the interatomic potential the advantages of displacement coupling (no ghost forces) and force coupling (stability) can be combined[4].

Figure 5.10 schematically depicts the harmonic buffer layer method. Black disks represent the bulk atoms and circles the harmonic buffer atoms. Some of the buffer atoms are free atoms (grey filled circles) and some are pad atoms (empty circles). Bulk atoms interact with each other and with the buffer atoms through the nonlinear interatomic potential and the layer of free buffer atoms is thick enough that no pad and bulk atoms interact. The buffer atoms interact through a harmonic potential fitted to represent the elastic properties of the bulk atoms. They are coupled to the continuum using regular displacement coupling, leading to a stable formulation that is free of ghost forces at small deformations. Figure 5.11b compares the evolution of T^* for the harmonic buffer layer to that of regular displacement coupling. Note that – contrary to the previously presented modifications – this approach completely solves the stability problem rather than providing a workaround. This makes the harmonic buffer layer a promising modification to displacement coupling at the cost of an increased implementation complexity.

---

[4] I would like to acknowledge the very helpful discussions with W. A. Curtin, with respect to the idea of the harmonic buffer layer, which he initiated.

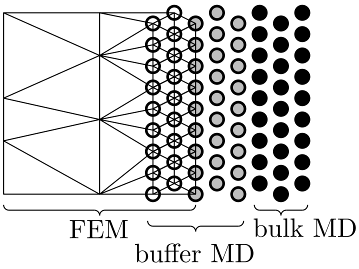

Figure 5.10 – Harmonic buffer layer coupling. The empty circles are pad atoms. Together with the grey filled circles they form the harmonic buffer layer. This layer interacts with the bulk atoms (black solid disks) through the nonlinear interatomic potential of the bulk.

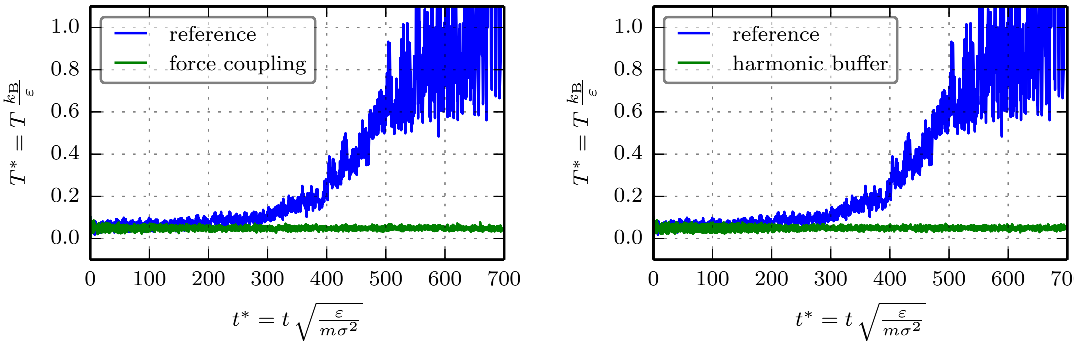

(a) Force coupling (green) stabilises the system. The blue line is regular displacement coupling.

(b) Introducing a harmonic buffer layer (green) gives similar stable results as force coupling, see Figure 5.11a. The blue line is regular displacement coupling.

Figure 5.11 – Stability through modified coupling. All simulations start at $T_0^* = 0.1$, consider interactions up to the second neighbour $N_{\text{neigh}} = 2$ and are discretised in time with $\Delta t = \frac{\tau_{\min}}{50}$.

5.3.5 A Few Words on the Bridging Domain Method

The bridging domain method (Xiao and Belytschko, 2004) (BDM) is a well established displacement coupling method[5] which has been successfully used for fully dynamic coupled atomistics and continuum problems (Xiao and Belytschko, 2004; Anciaux and Molinari, 2010, 2009) without apparent stability issues. In BDM, both the continuum and the atomistic description coexist in an extended overlapping bridging zone. The fine scale and the coarse scale energies are scaled by modifying the velocities in the overlapping (bridging) domain. However, the velocity scaling does not by itself stabilise the displacement coupling. Rather, because the method does not require full atomistic resolution of the finite-element mesh to the atomistic scale, the atomistic domain usually has more degrees of freedom in the overlapping zone than the continuum domain and the projection of velocities of the (fine scale) atomistic degrees of freedom onto the (coarse scale) degrees of freedom of the mesh dissipates kinetic energy. This dissipation can *hide* the instability.

Frequently however, one relies on a full atomistic resolution of the finite-element mesh near the interface in order to avoid an added artificial interfacial stiffness[6] and then the degrees of freedom of both scales match in the bridging domain. In this case the method is no longer dissipative. Figure 5.12 shows the temperature evolution of systems that are coupled using the BDM with two different overlap sizes and compares them to the displacement coupling reference. The size of the overlap zone is defined here by the number of atoms/nodes it contains N_b.

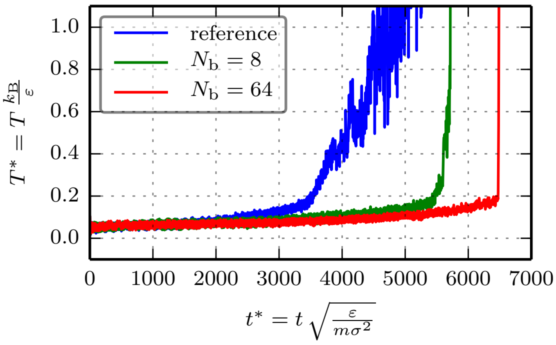

Figure 5.12 – Bridging domain method. Influence of the size of the bridging zone N_b. Even large zones do not avoid instability.

In order to accommodate large overlap sizes, the system size has been increased to 500 degrees of freedom of which the first 250 are finite-element nodes. All other parameters and initial conditions remain identical to the system described in Section 5.1.2 and

---

[5] Strictly speaking a velocity coupling method.

[6] Methods like CADD even require full resolution to avoid repulsing approaching dislocations from the interface.

Figure 5.2. One can see that even without dissipation of kinetic energy in the bridging domain, the BDM heats up less rapidly than regular displacement coupling, however the instability remains. Increasing the overlap size from 8 to 64 lattices only provides minimal improvements at an unpractical computational cost.

5.3.6 Three-Dimensional Problem

In order to show that the phenomena described in the previous section are not specific to one-dimensional systems, this section presents some supporting three-dimensional results. Figure 5.13 shows the simple three-dimensional setup used to compute the subsequent results. The atoms are set up in a face centred cubic (FCC) lattice with a lattice constant of $a = 4.05$ Å to mimic aluminium and the interatomic interactions are governed by the Mendelev et al. (2008) embedded atom model (EAM) potential of the form

$$E_{\text{pot}} = \frac{1}{2}\sum_{ij} V(r_{ij}) + \sum_{i} \Phi(\bar{\varrho}_i), \tag{5.20}$$

where $V(r_{ij})$ is a pair potential, $r_{ij} = ||\boldsymbol{r}_i - \boldsymbol{r}_j||$ is the distance between atoms i and j and Φ is the embedding energy required to insert an atom into the electron density $\bar{\varrho}_i = \sum_{j \neq i} \varrho(r_{ij})$ at the position of atom i due to all other atoms. The functions V, Φ and ϱ are semi-empirical potentials. The lattice is oriented so that the x, y and z axis point in the lattice directions $[\bar{1}, 10]$, $[1, 1, 1]$ and $[1, 1, 2]$ with respect to the coordinate system shown in Figure 5.13. The very thick pad is fully resolved atomistically, i.e., every pad or interface atom coincides with a finite-element node. The finite elements use an anisotropic, linearly elastic constitutive law that was fitted to match the Mendelev potential for small strains. Periodic boundary conditions in x and z directions emulate a large domain, the continuum surface at $y = y_{\max}$ (left boundary in Figure 5.13) is blocked and the atomic surface at $y = y_{\min}$ (right boundary in Figure 5.13) is left unconstrained. It is a very small system with 3648 atoms, of which 2240 are free (bulk) atoms, 1344 are pad atoms and 64 are interface atoms. The mesh consists of 11430 elements with 2155 nodes. In the original (initial) configuration, all atoms are at perfect lattice positions and the finite-element mesh is undeformed. Most of the system is therefore initially at rest, with only the atoms at the free boundary slightly off equilibrium.

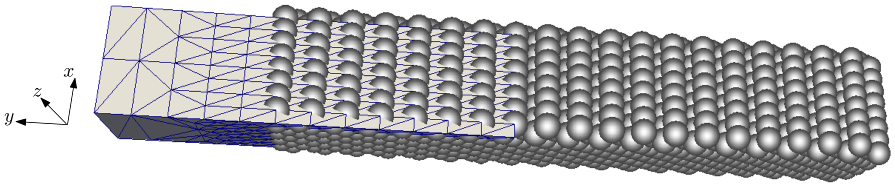

Figure 5.13 – Three-dimensional simulation case. Note that the finite-element mesh is fairly coarse on the left end and then gradually refined towards the pad zone, where the finite-element nodes coincide with atomic positions.

The system is mostly analogous to the one-dimensional system of the previous section, with one main difference; the continuum always starts at zero temperature. We will point out when this difference is of importance. Figure 5.14a shows the evolution of the temperature T for two different time steps and initial conditions. The red lines show the evolution of systems started at zero temperature and the blue lines the evolution of systems started at finite temperature. The source of energy to trigger the instability in the cold (red) case is the free boundary that emits a wave at the beginning of the simulation, as it relaxes. After about 30 ps of slow heat generation, the instability becomes fairly obvious and the temperature diverges.

The simulations starting at finite temperature are initialised with a random velocity field that corresponds to $T_0 = 50$ K. Since the initial displacement is zero, the temperature quickly drops to $\frac{1}{2}T_0$ as the system trades kinetic for potential energy. The subsequent slow drop in temperature to just above $T = 20$ K is due to the continuum starting at zero temperature; heat from the atomistic domain bleeds into it. After about $t = 7$ ps, the instability's heat generation rate exceeds the heat flow into the continuum, the temperature starts rising and finally diverges sometime after $t = 22$ ps, earlier than the cold case.

Both the initially cold and hot system have been simulated with time steps of $\Delta t = 1$ fs (solid lines) and $\Delta t = 0.25$ fs (dashed lines). One can see that the time step has very little influence on the temperature evolution, consistent with the predictions based on the one-dimensional simulations, see Figure 5.3a.

Figure 5.14b compares the evolution of T of the fully dynamic system (blue line) to the system with a quasistatic continuum domain (red line). As predicted by the one-dimensional analysis (see Figure 5.9a), prohibiting the dynamic interaction between the two domains solves the stability issues. Note that T for the quasistatic case, since the continuum does not heat up, hovers exactly around $T = 25\text{ K} = \frac{1}{2}T_0$. In order to save computational cost, we employ a scheme to update the continuum only when necessary. Details on our update scheme are presented in Appendix B. For conciseness, we do not show three-dimensional results with thermostats, force-coupling or a harmonic buffer layer.

Conclusion

We have shown that atomistic/continuum displacement coupling is dynamically unstable, and our analysis pin-points the linear/nonlinear mismatch – specifically the traction/compression asymmetry of interatomic potentials interacting with the traction/compression symmetry of the linear elastic continuum – to be the source of the observed instability.

Local/non-local mismatches leading to asymmetric forces that violate Newton's Third

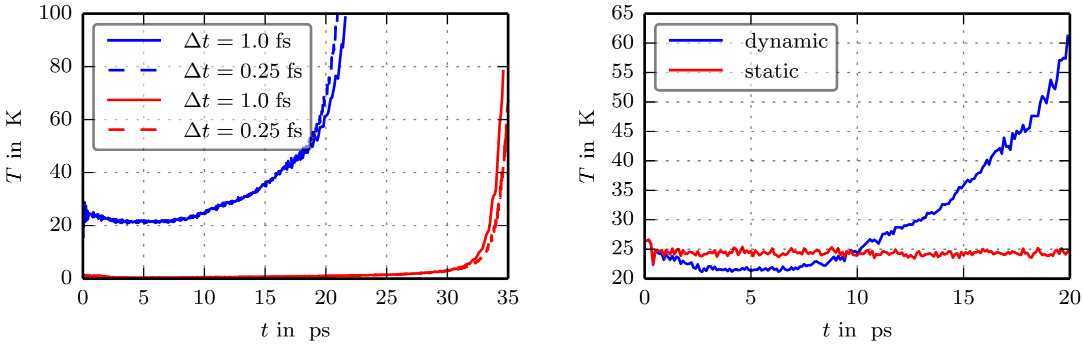

(a) The instability is fairly insensitive to the time step, as predicted by the 1D model (See Figure 5.3a). The red lines correspond to a system that started cold, blue for an initial temperature of 50 K.

(b) A quasistatic continuum stabilises the system, as predicted by the 1D model (See Figure 5.9a)

Figure 5.14 – Temperature evolution for the three-dimensional problem. The regular displacement coupling is unstable, as predicted by the one-dimensional simulations.

Law and lead to asymmetric stiffness matrices in the case of linear systems, however, are shown *not to be a problem for stability.*

We found a general solution to the stability problem that we call the harmonic buffer layer method and two simple workarounds which can be appropriate in some circumstances, leading us to give the following best practice recommendations:

- Adding a harmonic buffer layer to the atomistic/continuum interface fully solves the instability of displacement coupling, while *preserving full dynamics without ghost forces or the need for a bridging domain.* It comes at a heightened implementation cost.
- A simple method is to evacuate the excess heat due to the instability by thermostatting the computational domain. It does not require changes to the coupling method and most molecular dynamics codes already implement thermostats, thus making this a quick and simple fix. Thermostats however modify the dynamics of the system and because of the instability, the thermostat needs to be stronger than what would be sufficient for full molecular dynamics simulations. Appropriate thermostat parameters need to be chosen carefully. Since the spurious excess heat generation increases with increasing temperature, this approach is particularly unsuitable for high temperatures and requires a very careful interpretation of finite temperature results. While thermostatting might be appropriate in special cases where accurately predicting dynamics is of minor concern, these limitations make it a clearly inferior choice in general.
- Using a quasistatic continuum eliminates the root of the instability by avoiding

> inertial effects in the interaction between the atomistic and continuum domain. In problems for which concurrent multiscale coupling is interesting, only a small part of the computational domain exhibits fast nonlinear atomistic phenomena. If the dynamics of the surrounding continuum region can be safely assumed to be much slower, the quasistatic continuum is an elegant solution to the stability problem, albeit at the cost of statics finite-element calculations which are typically more expensive than dynamics.

With these recommendations, and the fundamentals presented in the previous chapter, it is possible to build stable simulation methods for large-scale domains.

6 Concluding Remarks and Outlook

6.1 Summary

In this thesis, I investigated the numerical modelling of nanoscale contact between crystalline metals from two sides. On the one hand, molecular dynamics has been used to study frictional contact and the limitations of single-scale modelling in this context. On the other hand, the development of three-dimensional CADD has been advanced in order to model and help understand the phenomena of contact taking into account all relevant length scales.

6.1.1 Single Scale Work

A large parametric nanoscale scratching study was performed to study the effects of scratching speed, indentation depth, microstructure and domain size on the frictional work as well as the development of plastic zones. A novel combined molecular dynamics and molecular statics approach for analysing nanoscale friction has been developed to define a clean separation of the friction work W_{sc} into heat generation Q and creation or release of permanently stored plastic deformation energy E_{pl}. Both Q and E_{pl} have been found to be distinctly scratch speed dependent, but while Q increases with increasing speed, E_{pl} appears to do the opposite. This indicates that at higher scratch speeds, plastic deformation does not have the time to establish itself permanently.

The study showed that microstructures help shield the bulk material from wear by trapping dislocations within grain boundaries. It has furthermore shown that in polycrystals, grain coarsening under the indenter presents an energy-releasing mechanism that competes with the storage of plastic energy. Without shielding microstructure, however, plasticity develops over length scales that go beyond the limitations of molecular dynamics. The analysis of E_{pl} shows that even the largest studied cases are not large enough to make size-effects disappear, thus motivating the development of appropriate multiscale methods for modelling plasticity.

6.1.2 Multiscale Work

An extension of the Coupled Atomistics and Discrete Dislocations (CADD) method to three dimensions has been worked out theoretically and a road map to its implementation including appropriate and practical test cases for each of its milestones is proposed. The foundations for efficient coupling on parallel computing clusters have been implemented within the open-source coupling framework LibMultiscale. Wherever possible, pre-existing and well-tested open-source software projects were modified into LibMultiscale plugins to reduce the development effort. Several test cases are presented in detail do demonstrate the functionality of the implementation.

The work on the three-dimensional CADD implementation has led to the observation that that displacement coupling multiscale methods without a well-defined energy functional are generally dynamically unstable. As a consequence these methods are particularly ill suited to finite temperature calculations. These limitations were previously poorly understood, as numerous examples of such misuse in the literature show. Various practical remedies to manage the instability were proposed and a fundamental solution to the problem is proposed theoretically in the form of a new coupling method with a harmonic buffer layer in which the driving force behind the instability does not exist.

6.1.3 Main Contributions

Of the work presented in this thesis, the three main contributions to the field of contact modelling in computational material science are the following.

- The method for the quantification of stored plastic energy in frictional contact in atomistic simulations
- The stability analysis of ghost force-free displacement coupling atomistic/continuum concurrent multiscale methods and proposed solution
- The road map to a three-dimensional Coupled Atomistics and Discrete Dislocations method.

6.2 Outlook

6.2.1 Immediate Future Work without Software Development

The method for the computation of permanently stored plastic energy E_{pl} developed for the nanoscratch study described in Chapter 3 has, so far, only been used for single crystal aluminium substrates of one single orientation and on a few nanocrystalline microstructures, even though it is applicable to any crystalline structure. Currently, a similar study is in preparation, in which the substrate is silicon carbide, and studies of more material systems will follow.

Apart from investigating new materials, it is interesting to look more into the effect of commensurability between indenter and substrate. Remember that all the single-crystal scratches where performed on commensurate setups in which the indenter and substrate were cut from the same crystal, and their interaction was treated the same way as all bulk atom interactions. This configuration was chosen because it provides an upper bound on the adhesion to the indenter that can be expected. Further studies could investigate incommensurate geometries and possibly mimic third-body interactions (lubrication) by modelling the indenter-substrate interaction with a reduced adhesion interatomic potential. This will likely reduce the friction forces (and therefore also the coefficient), but it is unclear how it will impact the evolution of E_{pl}.

Furthermore, future studies will probably examine the effects of impurities and atomic-scale roughness.

6.2.2 New Software Developments

The development of dislocation templates for arbitrary character angles is one of the objectives of a PhD project currently in progress. Once available, these templates will be used to improve the study of hybrid dislocations of Section 4.5. Understanding the magnitude of the potential spurious pinning forces acting on hybrid dislocations at the interface and their impact on the overall CADD coupling is important to estimate the performance of three-dimensional CADD in general.

The implementation of the DD $\leftrightarrow$ FE coupling as the next milestone on the road map of Chapter 4 in combination with the already implemented FEAt-coupling will enable us to perform a class of three-dimensional CADD calculations: coupled problems which do not involve hybrid dislocations, such as the coupled Frank-Read source of Section 4.6 can be simulated. While this still represents a substantial limitation to three-dimensional CADD, problems such as the Frank-Read source can then be studied at a range of length scales that is currently unavailable: from the Ångström to the micron. Furthermore, the DD $\leftrightarrow$ FE coupling in not only useful in the context of CADD, but is a full three-dimensional discrete dislocation dynamics simulator in its own right that allows to perform discrete dislocation dynamics calculations with complex boundary conditions, a feature that ParaDiS alone does not provide.

The last remaining step on the road map is the implementation of robust dislocation detection, as provided by methods such as DXA, briefly described in Section 4.1.2. It is a particularly interesting step, because its inclusion into LibMultiscale will not only complete the CADD coupling, but also provide exciting new analysis possibilities for single-scale calculations. The dislocation detection provides line segment-representations of full dislocation networks present in the atomistic domain. These can also be used outside of CADD, as discussed in the next section.

6.2.3 New Types of Studies Made Possible by Developments

Three-dimensional CADD is a coupling method with a very broad field of applications. This thesis concentrated mostly on contact, where CADD allows to drastically increase the plastic zones in indentation, scratching and friction problems, but it can equally be used to study problems such as fracture and plasticity around crystal defects.

The scratch study of Chapter 3 will be greatly improved by CADD coupling, which will allow the plastic zones to grow unencumbered by the (too small) atomistic domain boundaries. Realistic estimations of these sizes are currently impossible to obtain.

The method for the extraction of E_{pl} of Chapter 3 requires low temperatures, because the large deformations that accompany quenching from high finite temperatures can generate plasticity of their own, thus rendering the estimates worthless. However, as a by-product of the CADD development, it may be possible to compute E_{pl} for finite temperature domains: the dislocation detection plugin will provide line-segment representations of the dislocation networks in the substrate. These segments can be fed to the discrete dislocation dynamics plugin to compute the networks' self-energies. Naturally, the accuracy of such discrete dislocation dynamics estimates must be confirmed first by extensive low-temperature comparisons of the E_{pl} calculations and the discrete dislocation dynamics estimates. If they compare well, however, the estimation of E_{pl} at finite temperature is made possible.

A Fitting the Lennard-Jones Parameters

Determination of the Lennard-Jones Potential The Lennard-Jones potential is given as a function of interatomic distance r

$$V_{\mathrm{LJ}}(r) = 4\,\epsilon \left[\left[\frac{\sigma}{r} \right]^{12} - \left[\frac{\sigma}{r} \right]^{6} \right], \tag{A.1}$$

where ϵ is the depth of the potential's energy well and σ the distance at which the potential is zero. The goal is to determine ϵ and σ so that the potential satisfies the interatomic spacing a and exhibits the same stiffness k as the FEM part of the problem in the limit of infinitesimal strains. An atom in an infinite chain spaced by r_∞ has the energy

$$\begin{aligned} V_{\mathrm{chain}}(r_\infty) &= \sum_{i=-\infty, i\neq 0}^{\infty} \tfrac{1}{2} V_{\mathrm{LJ}}(i r_\infty) = \sum_{i=1}^{\infty} 4\,\epsilon \left[\left[\frac{\sigma}{i r_\infty} \right]^{12} - \left[\frac{\sigma}{i r_\infty} \right]^{6} \right], \\ &= 4\,\epsilon \left[\left[\frac{\sigma}{r_\infty} \right]^{12} \sum_{i=1}^{\infty} \frac{1}{i^{12}} - \left[\frac{\sigma}{r_\infty} \right]^{6} \sum_{i=1}^{\infty} \frac{1}{i^{6}} \right], \\ &= 4\,\epsilon \left[\zeta_\infty(12) \left[\frac{\sigma}{r_\infty} \right]^{12} - \zeta_\infty(6) \left[\frac{\sigma}{r_\infty} \right]^{6} \right], \end{aligned} \tag{A.2}$$

where $\zeta_n(m) = \sum_{i=1}^{n} \frac{1}{i^m}$ is a corrective factor when taking into account interactions up to the n-th neighbour in the chain. In (A.2) the interactions between all atoms are considered by using $n = \infty$. However, since interatomic potentials[1] are short-ranged, it is typically sufficient to determine a cutoff radius and consider only interactions with the first n neighbours in the chain, in which case the interatomic spacing will be denoted r_n.

The parameter σ of the potential can be computed from the spacing a, where the chain potential has to be at its minimum. Here, we consider a chain with n-th neighbour interactions and the corresponding interatomic spacing r_n

---

[1] In the absence of electric charges causing long-ranged Coulomb forces, that is.

$$\left.\frac{\partial V_{\text{chain}}}{\partial r_n}\right|_{r_n=a} = 0 = 24\frac{\epsilon}{r_n}\left.\left[2\,\zeta_n(12)\left[\frac{\sigma}{r_n}\right]^{12} - \zeta_n(6)\left[\frac{\sigma}{r_n}\right]^{6}\right]\right|_{r_n=a},$$

$$\Rightarrow \sigma = a\sqrt[6]{\frac{\zeta_n(6)}{2\zeta_n(12)}}. \tag{A.3}$$

With σ fixed, the parameter ϵ can be determined as function of the spring stiffness k, which corresponds to the second derivative of the chain potential[2]

$$-k = \left.\frac{\partial^2 V_{\text{chain}}}{\partial r_n^2}\right|_{r_n=a} = 24\frac{\epsilon}{r_n^2}\left.\left[7\,\zeta_n(6)\left[\frac{\sigma}{r_n}\right]^{6} - 26\,\zeta_n(12)\left[\frac{\sigma}{r_n}\right]^{12}\right]\right|_{r_n=a},$$

$$\Rightarrow \epsilon = \frac{ka^2}{24\left[26\,\zeta_n(12)\left[\frac{\sigma}{a}\right]^{12} - 7\,\zeta_n(6)\left[\frac{\sigma}{a}\right]^{6}\right]}. \tag{A.4}$$

Linearisation of the Problem In order to linearise the problem, the i-th neighbour-spring stiffness k_i is obtained by evaluating the second derivative of the Lennard-Jones potential at $r = ia$,

$$k_i = -\left.\frac{\partial^2 V_{\text{LJ}}}{\partial r^2}\right|_{r=ia} = 24\frac{\epsilon}{(ia)^2}\left[26\left[\frac{\sigma}{ia}\right]^{12} - 7\left[\frac{\sigma}{ia}\right]^{6}\right]. \tag{A.5}$$

By substituting (A.3) into (A.4) and then into (A.5), we obtain

$$k_i = k\frac{1}{3i^2\zeta_n(6)}\left[\frac{13}{2}\frac{\zeta_n(6)}{i^{12}\zeta_n(12)} - \frac{7}{2i^6}\right] = \alpha_i k, \tag{A.6}$$

where the coefficients α_i depend only on the number of neighbours n taken into account and not on the potential parameters ϵ and σ. The result (A.6) can be verified by a simple physical argument: in order for the FEM chain and the linearised MD chain to match, the tension in both chains must be equal at equal uniform strain ϵ, i.e. when either chain is cut, the tension force f that acted on the severed FEM spring $f = ka\epsilon$ must be equal to the sum of the tension forces f_j that acted on all severed springs k_j. When cutting an n-th neighbour chain, we sever one first neighbour spring k_1, two second neighbour springs k_2 and so on until n n-th neighbour springs k_n, see Figure A.1. Every

---

[2] Note that the same result can be obtained by applying the Cauchy-Born rule, see Tadmor et al. (1996)

i-th neighbour spring k_i is strained by $ia\epsilon$ and the total force is therefore

$$\begin{aligned} f = ka\epsilon &= \sum_{i=1}^{n} i^2\, k_i a\epsilon, \\ \Rightarrow k &= \sum_{i=1}^{n} i^2 k_i. \end{aligned} \tag{A.7}$$

Note that the stiffnesses (A.6) satisfy this equivalence condition between the continuum and the MD.

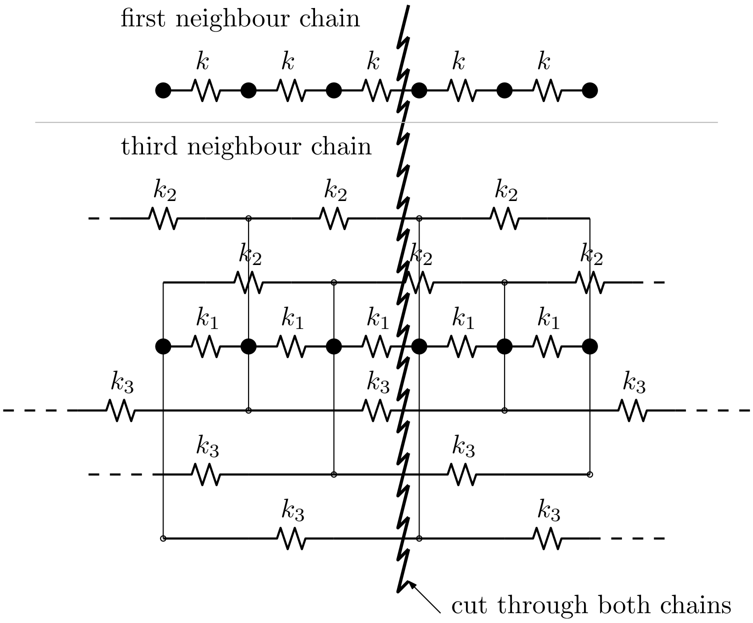
first neighbour chain
k
k
k
k
k
third neighbour chain
k_2
k_2
k_2
k_2
k_2
k_2
k_1
k_1
k_1
k_1
k_1
k_3
k_3
k_3
k_3
k_3
k_3
k_3
cut through both chains

Figure A.1 – Cut through a chain with n-th neighbour interactions. Any cut severs one first neighbour spring k_1, two second neighbour springs k_2 and so on until n n-th neighbour springs k_n. At constant strain ϵ, every n-th neighbour spring is stretched or compressed by $\Delta u = n\epsilon$.

B On-Demand Update Strategy for Quasistatic Continuum

Computing a static solution for two- or three-dimensional FEM problems is much more costly than an explicit dynamic step because it involves solving a matrix equation of the type

$$\underbrace{\mathbf{K}\boldsymbol{u} - \boldsymbol{f}_{\text{ext}}}_{\boldsymbol{r}(\boldsymbol{u})} = \mathbf{0}, \tag{B.1}$$

where $\boldsymbol{u}$ contains the displacements for all n_{dof} degrees of freedom, $\mathbf{K}$ is the system's assembled stiffness matrix of size $n_{\text{dof}} \times n_{\text{dof}}$ and $\boldsymbol{f}_{\text{ext}}$ contains optional external forces on the degrees of freedom. The vector $\boldsymbol{r}(\boldsymbol{u})$ is the residual force vector. However, since the goal of the quasistatic continuum is not to track thermal fluctuations but slower deformations, it is not necessary to update the static continuum at every time step. Qu et al. (2005) proposed to update the continuum at a rate corresponding to the typical atomic vibration (Debye frequency) and added stochastic variations to the update schedule in order to reduce resonant behaviour due to the periodicity of the update, which can "erroneously pump energy into, or extract energy out of, the atomistic region" (Qu et al., 2005). We propose a simple aperiodic, adaptive, lazy update method where (B.1) is only solved when needed.

- The residual $\boldsymbol{r}(\boldsymbol{u})$ is evaluated at every time step. Since $\mathbf{K}$ is a very sparse matrix, this is computationally cheap.
- If $||\boldsymbol{r}(\boldsymbol{u})||$ exceeds a predefined tolerance, an update is triggered.

Figure B.1 compares the temperature evolution for two systems with identical initial conditions but two orders of magnitude of difference in the update tolerance. We use a tolerance normalised by the number of interface atoms since they are the only nodes of the mesh that move. This way, the tolerances are comparable across different meshes. Initially, the two system temperatures evolve almost identically and only after about $t = 30$ ps do the systems exhibit a slight difference of the order of the temperature

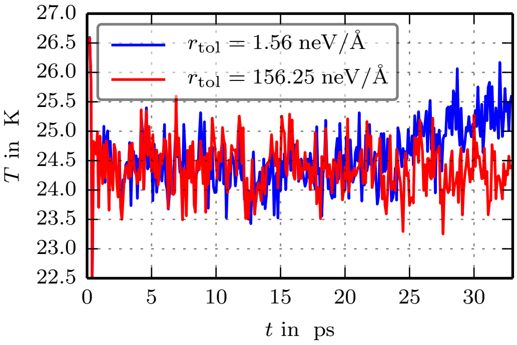

Figure B.1 – Temperature of the atomistic domain with lazily updated continuum. The reported tolerances are the global tolerance divided by the number of interface atoms.

fluctuations. The choice of the tolerance appears to have a very small influence on the system dynamics, making the proposed update method a safe choice.

C Rotation of Elastic Tensors

Let $\boldsymbol{\epsilon}'$, $\boldsymbol{\sigma}'$ and $\mathbb{C}'$ be the strain, stress and elastic stiffness tensors of an orthotropic material expressed in the coordinate system for which the basis vectors $\boldsymbol{e}'^{i}$ are normal to the material symmetry planes. The matrix $\mathbf{R}$ allowing to pass from the material basis to the global basis is given by

$$R_{ij} = \boldsymbol{e}'_i \cdot \boldsymbol{e}_j, \tag{C.1}$$

where $\boldsymbol{e}_j$ is the j-th basis vector of the coordinate system in which we wish to express the elastic stiffness tensor $\mathbb{C}$. Note that in this convention, the base vectors $\boldsymbol{e}'_j$ of the material coordinate system form the *row* vectors of the rotation matrix. The stress and strain in the material reference are related to the global reference by

$$\boldsymbol{\epsilon}' = \mathbf{R}\boldsymbol{\epsilon}\mathbf{R}^{\mathrm{T}}, \boldsymbol{\sigma}' = \mathbf{R}\boldsymbol{\sigma}\mathbf{R}^{\mathrm{T}}. \tag{C.2}$$

The definition of the direct tensor product allows to reformulate (C.2) as

$$\mathbf{R}\boldsymbol{\epsilon}\mathbf{R}^{\mathrm{T}} = \left(\mathbf{R}\underline{\otimes}\mathbf{R}\right)\boldsymbol{\epsilon} = \underline{\mathbb{R}}\boldsymbol{\epsilon}. \tag{C.3}$$

Or, in index notation

$$R_{ij}\epsilon_{jk}R_{lk} = R_{ij}R_{lk}\epsilon_{jk}, \text{or} \tag{C.4}$$

$$\Rightarrow \underline{R}_{ijkl}\epsilon_{kl} = R_{ik}R_{jl}\epsilon_{kl}. \tag{C.5}$$

I also define $\underline{\mathbb{R}}^{\mathrm{T}}$ as

$$\mathbf{R}^{\mathrm{T}}\underline{\otimes}\mathbf{R}^{\mathrm{T}} = \underline{\mathbb{R}}^{\mathrm{T}} \tag{C.6}$$

The constitutive law for orthotropic materials (or any linear elastic material) is

$$
\begin{aligned}
\boldsymbol{\sigma}' &= \mathbb{C}'\boldsymbol{\epsilon}', \\
\mathbf{R}\boldsymbol{\sigma}\mathbf{R}^{\mathrm{T}} &= \mathbb{C}'\mathbf{R}\boldsymbol{\epsilon}\mathbf{R}^{\mathrm{T}}, && \text{(C.7)} \\
\underline{\mathbb{R}}\boldsymbol{\sigma} &= \mathbb{C}'\underline{\mathbb{R}}\boldsymbol{\epsilon}, \\
\boldsymbol{\sigma} &= \underbrace{\underline{\mathbb{R}}^{\mathrm{T}}\mathbb{C}'\underline{\mathbb{R}}}_{\mathbb{C}}\,\boldsymbol{\epsilon}. && \text{(C.8)}
\end{aligned}
$$

This is easily verified in index notation, starting from (C.7)

$$R_{ij}\sigma_{jk}R_{lk} = C'_{ilmn}R_{mo}\epsilon_{op}R_{np}, \tag{C.9}$$

We premultiply by $\mathbf{R}^{\mathrm{T}}$ and postmultiply by $\mathbf{R}$

$$\underbrace{R_{ia}R_{ij}}_{\delta_{aj}}\,\sigma_{jk}\,\underbrace{R_{lk}R_{lb}}_{\delta_{kb}} = R_{ia}C'_{ilmn}R_{mo}\epsilon_{op}R_{np}R_{lb}, \tag{C.10}$$

This can be reorganised to reflect the vectorial form (C.8)

$$\sigma_{ab} = \underbrace{\underbrace{R_{ia}R_{lb}}_{\underline{R}^{\mathrm{T}}_{abil}}\,C'_{ilmn}\,\underbrace{R_{mo}R_{np}}_{\underline{R}_{mnop}}}_{C_{abop}}\,\epsilon_{op}. \tag{C.11}$$

Bibliography

Abraham, F. F., Bernstein, N., Broughton, J. Q., Hess, D., 2000. Dynamic Fracture of Silicon: Concurrent Simulation of Quantum Electrons, Classical Atoms, and the Continuum Solid. MRS Bulletin 25 (05), 27–32.

Abraham, F. F., Broughton, J. Q., Bernstein, N., Kaxiras, E., 1998. Spanning the length scales in dynamic simulation. Computers in Physics 12, 538–546.

Amontons, G., 1699. Sur l'origine de la résistance dans les machines. Mémoires de l'Académie Royale, 206–222.

Amontons, G., 1999. Resistance in machines. 1. Friction law. Journal of Japanese Society of Tribologists 44 (4), 229–235.

Anciaux, G., 2009. Libmultiscale, .
URL http://libmultiscale.gforge.inria.fr/

Anciaux, G., Coulaud, O., Roman, J., 2006. High performance multiscale simulation of crack propagation. 2006 International Conference on Parallel Processing Workshops, Proceedings, 473–480.

Anciaux, G., Molinari, J.-F., 2009. Contact mechanics at the nanoscale, a 3D multiscale approach. International Journal for Numerical Methods in Engineering 79 (9), 1041.

Anciaux, G., Molinari, J. F., 2010. Sliding of rough surfaces and energy dissipation with a 3D multiscale approach. International Journal for Numerical Methods in Engineering 83 (8-9), 1255.

Anton, H., Rorres, C., 2000. Elementary Linear Algebra, 8th Applications Edition. Wiley.

ASTM, 2010. Standard Test Methods for Determining Average Grain Size. Tech. Rep. e112, ASTM, ASTM Int'l, West Conshohocken, Pa, US.

Bailey, A. I., Courtney-Pratt, J. S., 1955. The Area of Real Contact and the Shear Strength of Monomolecular Layers of a Boundary Lubricant. Proceedings of the Royal Society of London. Series A, Mathematical and Physical Sciences 227 (1171), 500–515.

Barnett, D. M., 1985. The displacement field of a triangular dislocation loop. Philosophical Magazine A 51 (3), 383–387.

Barnoush, A., Welsch, M. T., Vehoff, H., 2010. Correlation between dislocation density and pop-in phenomena in aluminum studied by nanoindentation and electron channeling contrast imaging . Scripta Materialia 63 (5), 465–468.

Baumberger, T., Caroli, C., 2006. Solid friction from stick–slip down to pinning and aging. Advances in Physics 55 (3-4), 279.

Bellman, R., 1969. Stability Theory of Differential Equations. Dover Publications.

Belytschko, T., Liu, W. K., Moran, B., 2000. Nonlinear Finite Elements for Continua and Structures. Wiley.

Berendsen, H. J. C., 2007. Simulating the Physical World: Hierarchical Modeling from Quantum Mechanics to Fluid Dynamics. Cambridge University Press, New York, NY, USA.

Blau, P. J., 2001. The significance and use of the friction coefficient. Tribology International 34 (9), 585–591.

Blau, P. J., 2008. Friction Science and Technology, 2 Edition. CRC Press, Boca Raton, FL, USA.

Born, M., Oppenheimer, R., 1927. Zur Quantentheorie der Molekeln. Annalen der Physik 84 (20), 0457–0484.

Bowden, F. P., Tabor, D., JUL-DEC 1942. Mechanism of metallic friction. Nature 150, 197–199.

Brandl, C., Derlet, P. M., Van Swygenhoven, H., 2011. Dislocation mediated plasticity in nanocrystalline Al: the strongest size. Modelling and Simulation in Materials Science and Engineering 19 (7), 074005.

Brinckmann, S., Mahajan, D. K., Hartmaier, A., 2012. A scheme to combine molecular dynamics and dislocation dynamics. Modelling and Simulation in Materials Science and Engineering 20 (4), 045001.

Broughton, J. Q., Abraham, F. F., Bernstein, N., Kaxiras, E., 1999. Concurrent coupling of length scales: Methodology and application. Phys. Rev. B 60 (4), 2391–2403.

Brukman, M. J., Marco, G. O., Dunbar, T. D., Boardman, L. D., Carpick, R. W., APR 25 2006. Nanotribological properties of alkanephosphonic acid self-assembled monolayers on aluminum oxide: Effects of fluorination and substrate crystallinity. Langmuir 22 (9), 3988–3998.

Bulatov, V., Cai, W., 2006. Computer Simulations of Dislocations (Oxford Series on Materials Modelling). Oxford University Press, USA.

Bulatov, V., Cai, W., Fier, J., Hiratani, M., Hommes, G., Pierce, T., Tang, M., Rhee, M., Yates, K., Arsenlis, T., 2004. Scalable line dynamics in ParaDiS. In: Proceedings of the 2004 ACM/IEEE conference on Supercomputing. p. 19.

Bulatov, V. V., Hsiung, L. L., Tang, M., Arsenlis, A., Bartelt, M. C., Cai, W., Florando, J. N., Hiratani, M., Rhee, M., Hommes, G., Pierce, T. G., de la Rubia, T. D., 2006. Dislocation multi-junctions and strain hardening. Nature 440 (7088), 1174–8.

Cai, W., Jun 2001. Atomistic and Mesoscale Modeling of Dislocation Mobility. Ph.D. thesis, Massachusetts Institute of Technology.

Cai, W., Arsenlis, A., Weinberger, C., Bulatov, V., 2006. A non-singular continuum theory of dislocations. Journal of the Mechanics and Physics of Solids 54 (3), 561.

Cai, W., Arsenlis, T., Bulatov, V., Hommes, G., Rhee, M., Tang, M., 2004a. ParaDiS (Parallel Dislocation Simulator). last visited Jun 22, 2014.
URL http://paradis.stanford.edu

Cai, W., Bulatov, V. V., 2004. Mobility laws in dislocation dynamics simulations. Materials Science and Engineering A 387-389 (387-389), 277–281.

Cai, W., Bulatov, V. V., Pierce, T. G., Hiratani, M., Rhee, M., Bartelt, M., Tang, M., 2004b. Massively-parallel dislocation dynamics simulations. In: Kitagawa, H., Shibutani, Y. (Eds.), Iutam Symposium on Mesoscopic Dynamics of Fracture Process and Materials Strength. Vol. 115 of Solid Mechanics and its Applications. pp. 1–11.

Carnes, K., JUN 2005. The ten greatest events in tribology history. Tribology & Lubrication Technology 61 (6), 38–47.

Chakravarthy, S. S., Curtin, W., MAY 2010. Effect of source and obstacle strengths on yield stress: A discrete dislocation study. Journal of the Mechanics and Physics of Solids 58 (5), 625.

Chandross, M., Lorenz, C. D., Stevens, M. J., Grest, G. S., FEB 19 2008. Simulations of nanotribology with realistic probe tip models. Langmuir 24 (4), 1240–1246.

Curnier, A., 2000. Méthodes numériques en mécanique des solides, 2 Edition. Presses polytechniques et universitaires romandes, Lausanne, Switzerland.

Curtin, W. A., Miller, R. E., 2003. Atomistic/continuum coupling in computational materials science. Modelling and Simulation in Materials Science and Engineering 11 (3), –33.

Datta, D. K., Picu, R. C., Shephard, M. S., 2004. Composite Grid Atomistic Continuum Method: An Adaptive Approach to Bridge Continuum with Atomistic Analysis. International Journal for Multiscale Computational Engineering 2 (3), 401–419.

de Koning, M., Cai, W., Bulatov, V. V., 2003. Anomalous Dislocation Multiplication in FCC Metals. Physical Review Letters, vol. 91, Issue 2, id. 025503 91, 25503.

Del Pedro, M., Pahud, P., 2003. Mécanique Vibratoire - Systèmes discrets linéaires, 3rd Edition. Presses polytechniques et universitaire romandes, Lausanne, Switzerland.

Delaunay, B., 1934. Sur la sphère vide. A la mémoire de Georges Voronoï. Bulletin de l'Académie des Sciences de l'URSS. Classe des sciences mathématiques et naturelles 1 (6), 793–800.

Derlet, P. M., Van Swygenhoven, H., Jan 2003. Atomic positional disorder in fcc metal nanocrystalline grain boundaries. Phys. Rev. B 67 (1), 014202.

Dewald, M., Curtin, W. A., 2006. Analysis and minimization of dislocation interactions with atomistic/continuum interfaces. Modelling and Simulation in Materials Science and Engineering 14 (3), 497.

El-Awady, J. A., Uchic, M. D., Shade, P. A., Kim, S.-L., Rao, S. I., Dimiduk, D. M., Woodward, C., 2013. Pre-straining effects on the power-law scaling of size-dependent strengthening in Ni single crystals . Scripta Materialia 68 (3–4), 207–210.

Evans, A., Hutchinson, J., 2009. A critical assessment of theories of strain gradient plasticity. Acta Materialia 57 (5), 1675.

Gao, Y., Lu, C., Huynh, N., Michal, G., Zhu, H., Tieu, A., 2009. Molecular dynamics simulation of effect of indenter shape on nanoscratch of Ni. Wear 267 (11), 1998.

Giessibl, F. J., Jul 2003. Advances in atomic force microscopy. Rev. Mod. Phys. 75 (3), 949–983.

Gmür, T., 2000. Méthode des éléments finis en mécanique des structures. Presses polytechniques est universitaires romandes, Lausanne, Switzerland.

Griebel, M., Knapek, S., Zumbusch, G., 2007. Numerical Simulation in Molecular Dynamics: Numerics, Algorithms, Parallelization, Applications (Texts in Computational Science and Engineering). Springer.

Gu, J.-C., Rice, J. R., Ruina, A. L., Tse, S. T., 1984. Slip motion and stability of a single degree of freedom elastic system with rate and state dependent friction. Journal of the Mechanics and Physics of Solids 32 (3), 167–196.

Heyn, E., 1903. Short reports from the metallurgical and metallographical laboratory of the royal mechanical and technical testing institute of Charlottenburg. The Metallographist VI, 39–64.

Hill, T. L., 1987. Statistical Mechanics: Principles and Selected Applications. Dover Publications.

Hirth, J. P., Lothe, J., 1992. Theory of Dislocations, second Edition. Krieger Publishing Company, Malabar, Florida, U.S.A.

Hod, O., 2012. Interlayer commensurability and superlubricity in rigid layered materials. Physical Review B 86 (7).

Honeycutt, J. D., Andersen, H., 1987. Molecular Dynamics Study of Melting and Freezing of Small Lennard-Jones Clusters. Journal of Physical Chemistry 91 (19), 4950–4963.

Hoy, R., Robbins, M., 2007. Strain Hardening in Polymer Glasses: Limitations of Network Models. Physical Review Letters 99 (11).

Hughes, T. J. R., 1987. The Finite Element Method: Linear Static and Dynamic Finite Element Analysis. Prentice Hall.

Junge, T., Molinari, J.-F., 2014. Plastic activity in nanoscratch molecular dynamics simulations of pure aluminium . International Journal of Plasticity 53 (0), 90–106.

Kelchner, C. L., Plimpton, S. J., Hamilton, J. C., Nov 1998. Dislocation nucleation and defect structure during surface indentation. Phys. Rev. B 58 (17), 11085–11088.

Kohlhoff, S., Gumbsch, P., Fischmeister, H., 1991. Crack-Propagation in bcc Crystals Studied with a Combined Finite-Element and Atomistic Model. Philosophical Magazine A-Physics Of Condensed Matter Structure Defects And Mechanical Properties 64 (4), 851–878.

Komanduri, R., Chandrasekaran, N., Raff, L., 2000. Molecular dynamics simulation of atomic-scale friction. Physical Review B 61, 14007–14019.

LAMMPS, 2010. LAMMPS.
URL http://lammps.sandia.gov

Lee, S.-W., Han, S. M., Nix, W. D., 2009. Uniaxial compression of fcc Au nanopillars on an MgO substrate: The effects of prestraining and annealing . Acta Materialia 57 (15), 4404–4415.

Liu, X. M., Liu, Z. L., Wei, Y. G., 2012. Nanoscale Friction Behavior of the Ni-Film/Substrate System Under Scratching Using MD Simulation. Tribology Letters.

Liu, Y., Szlufarska, I., MAR 8 2010. Effect of trace moisture on friction. Applied Physics Letters 96 (10).

Luan, B., Feb 2006. Simulations of contact and friction: connecting atomic and continuum descriptions. Ph.D. thesis, Johns Hopkins University, Baltimore MD, USA.

Luan, B., Hyun, S., Molinari, J., Bernstein, N., Robbins, M., 2006. Multiscale modeling of two-dimensional contacts. Physical Review E 74 (4).

Luan, B., Robbins, M. O., 2005. The breakdown of continuum models for mechanical contacts. Nature 435 (7044), 929–32.

Luan, B., Robbins, M. O., 2009. Hybrid Atomistic/Continuum Study of Contact and Friction Between Rough Solids. Tribology Letters 36 (1), 1.

Mastny, E. A., de Pablo, J. J., 2007. Melting line of the Lennard-Jones system, infinite size, and full potential. Journal of Chemical Physics, Volume 127, Issue 10, pp. 104504-104504-8 (2007). 127, 4504.

McQuarrie, D. A., 1975. Statistical mechanics. Harper & Row, New York.

Mendelev, M. I., Asta, M., Rahman, M. J., Hoyt, J. J., 2009. Development of interatomic potentials appropriate for simulation of solid-liquid interface properties in Al-Mg alloys. Philosophical Magazine, vol. 89, issue 34, pp. 3269-3285 89, 3269–3285.

Mendelev, M. I., Kramer, M. J., Becker, C. A., Asta, M., 2008. Analysis of semi-empirical interatomic potentials appropriate for simulation of crystalline and liquid Al and Cu. Philosophical Magazine 88 (12), 1723–1750.

Merkle, A. P., Marks, L. D., 2007. A predictive analytical friction model from basic theories of interfaces, contacts and dislocations. Tribology Letters 26 (1), 73.

Miller, R., Shilkrot, L., Curtin, W., 2004. A coupled atomistics and discrete dislocation plasticity simulation of nanoindentation into single crystal thin films. Acta Materialia 52 (2), 271.

Miller, R. E., Tadmor, E. B., 2009. A unified framework and performance benchmark of fourteen multiscale atomistic/continuum coupling methods. Modelling and Simulation in Materials Science and Engineering 17 (5).

Mo, Y., Szlufarska, I., 2010. Roughness picture of friction in dry nanoscale contacts. Physical Review B 81 (3), 035405.

Mo, Y., Turner, K. T., Szlufarska, I., 2009. Friction laws at the nanoscale. Nature 457 (7233), 1116–9.

Molinari, A., Estrin, Y., Mercier, S., JAN 1999. Dependence of the coefficient of friction on the sliding conditions in the high velocity range. Journal of Tribology - Transactions of the ASME 121 (1), 35–41.

Moseley, P., Oswald, J., Belytschko, T., 2012. Adaptive atomistic-to-continuum modeling of propagating defects. International Journal for Numerical Methods in Engineering 92, 835–856.

Nair, A. K., Parker, E., Gaudreau, P., Farkas, D., Kriz, R. D., 2008. Size effects in indentation response of thin films at the nanoscale: A molecular dynamics study. International Journal of Plasticity 24 (11), 2016.

Nicola, L., Bower, A., Kim, K.-S., Needleman, A., Van der Giessen, E., 2007. Surface versus bulk nucleation of dislocations during contact. Journal of the Mechanics and Physics of Solids 55 (6), 1120.

Nicola, L., Bower, A. F., Kim, K. S., Needleman, A., Van der Giessen, E., 2008. Multi-asperity contact: A comparison between discrete dislocation and crystal plasticity predictions. Philosophical Magazine 88 (30), 3713.

Olmsted, D. L., Jr, L. G. H., Curtin, W. A., Clifton, R. J., 2005. Atomistic simulations of dislocation mobility in Al, Ni and Al/Mg alloys. Modelling and Simulation in Materials Science and Engineering 13 (3), 371.

Philippon, S., Sutter, G., Molinari, A., 2004. An experimental study of friction at high sliding velocities. Wear 257 (7-8), 777.

Plimpton, S., 1995. Fast parallel algorithms for short-range molecular-dynamics. Journal of computational physics 117 (1), 1–19.

PostgreSQL, G. D. G., 2008. PostgreSQL 8.4.8. URL http://www.postgresql.org.

Qian, D., Wagner, G. J., Liu, W. K., 2004. A multiscale projection method for the analysis of carbon nanotubes . Computer Methods in Applied Mechanics and Engineering 193 (17–20), 1603–1632.

Qu, S., Shastry, V., Curtin, W. A., Miller, R. E., 2005. A finite-temperature dynamic coupled atomistic/discrete dislocation method. Modelling and Simulation in Materials Science and Engineering 13 (7), 1101–1118.

Rabinowicz, E., 1995. Friction and Wear of Materials. Cambridge University Press, New York, NY, USA.

Rapaport, D. C., 2004. The Art of Molecular Dynamics Simulation. Cambridge University Press.

Richart, N., Anciaux, G., Molinari, J.-F., 2010. An optimized finite-element library: Akantu. Flash informatique 10, 11–12.

Richart, N., Molinari, J.-F., 2014. Implementation of a parallel finite-element library: test case on a non-local continuum damage model. submitted.

Romero, P. A., Anciaux, G., Molinari, A., Molinari, J. F., 2012. Friction at the tool-chip interface during orthogonal nanometric machining. Modelling and Simulations in Materials Sciences and Engineering.

Romero, P. A., Anciaux, G., Molinari, A., Molinari, J.-F., 2013. Insights into the thermomechanics of orthogonal nanometric machining. Computational Materials Science 72, 116–126.

Rudd, R. E., Broughton, J. Q., 2005. Coarse-grained molecular dynamics: Nonlinear finite elements and finite temperature. Phys. Rev. B 72 (14), 144104.

Sansoz, F., Dupont, V., 2006. Grain growth behavior at absolute zero during nanocrystalline metal indentation. Applied Physics Letters 89 (11), 111901.

Schneider, T., Stoll, E., 1978. Molecular-dynamics study of a three-dimensional one-component model for distortive phase transitions. Phys. Rev. B 17 (3), 1302–1322.

Shenoy, V. B., Miller, R., Tadmor, E. B., Phillips, R., Ortiz, M., 1998. Quasicontinuum Models of Interfacial Structure and Deformation. Phys. Rev. Lett. 80 (4), 742–745.

Shenoy, V. B., Miller, R., Tadmor, E. b., Rodney, D., Phillips, R., Ortiz, M., 1999. An adaptive finite element approach to atomic-scale mechanics–the quasicontinuum method. Journal of the Mechanics and Physics of Solids 47 (3), 611–642.

Shiari, B., Miller, R. E., Curtin, W. A., 2005. Coupled atomistic/discrete dislocation simulations of nanoindentation at finite temperature. Journal of Engineering Materials and Technology-Transactions of the ASME 127 (4), 358–368.

Shilkrot, L., Miller, R., Curtin, W. A., 2002a. Coupled Atomistic and Discrete Dislocation Plasticity. Physical Review Letters 89 (2), 025501.

Shilkrot, L. E., Curtin, W. A., Miller, R. E., 2002b. A coupled atomistic/continuum model of defects in solids. Journal of the Mechanics and Physics of Solids 50 (10), 2085–2106.

Shilkrot, L. E., Miller, R. E., Curtin, W. A., 2004. Multiscale plasticity modeling: coupled atomistics and discrete dislocation mechanics. Journal of the Mechanics and Physics of Solids, Volume 52, Issue 4, p. 755-787. 52, 755–787.

Spijker, P., Anciaux, G., Molinari, J. F., 2011. Dry Sliding Contact Between Rough Surfaces at the Atomistic Scale. Tribology Letters 44 (2), 279.

Spijker, P., Anciaux, G., Molinari, J. F., 2012. Relations between roughness, temperature and dry sliding friction at the atomic scale. Tribology International in press.

Stukowski, A., 2009. Visualization and analysis of atomistic simulation data with OVITO–the Open Visualization Tool. Modelling and Simulation in Materials Science and Engineering 18 (1), 015012.

Stukowski, A., Albe, K., 2010. Dislocation detection algorithm for atomistic simulations. Modelling and Simulation in Materials Science and Engineering 18 (2), 025016.

Stukowski, A., Bulatov, V. V., Arsenlis, A., 2012. Automated identification and indexing of dislocations in crystal interfaces. Modelling and Simulation in Materials Science and Engineering 20 (8), 085007.

Szlufarska, I., Chandross, M., Carpick, R. W., 2008. Recent advances in single-asperity nanotribology. Journal of Physics D: Applied Physics 41 (12), 123001.

Tadmor, E. B., Miller, R. E., 2012. Modeling Materials: Continuum, Atomistic and Multiscale Techniques. Cambridge University Press.

Tadmor, E. B., Miller, R. E., Elliott, R. S., 2012. Continuum mechanics and thermodynamics : from fundamental concepts to governing equations. Cambridge University Press, Cambridge, UK New York.

Tadmor, E. B., Ortiz, M., Phillips, R., 1996. Quasicontinuum analysis of defects in solids. Philosophical Magazine A – Physics of Condensed Matter Structure Defects and Mechanical Properties 73 (6), 1529–1563.

Tucker, G. J., Foiles, S. M., 2013. Molecular dynamics simulations of rate-dependent grain growth during the surface indentation of nanocrystalline nickel. Materials Science and Engineering: A 571 (0), 207–214.

van der Giessen, E., Needleman, A., 1995. Discrete Dislocation Plasticity - A Simple Planar Model. Modelling and simulation in Materials Science and Engineering 3 (5), 689–735.

Van Swygenhoven, H., Derlet, P., Frøseth, A., 2006. Nucleation and propagation of dislocations in nanocrystalline fcc metals. Acta Materialia 54 (7), 1975.

Volterra, V., 1907. Sur l'équilibre des corps élastiques multiplement connexes. Annales scientifiques de l'École Normale Supérieure 24, 401–517.

Voronoï, M. G., 1908. Recherches sur les parallélloèdres primitifs. Journal für die reine und angewandte Mathematik 134 (1/4), 198–287.

Wagner, G. J., Liu, W. K., 2003. Coupling of atomistic and continuum simulations using a bridging scale decomposition . Journal of Computational Physics 190 (1), 249–274.

Weertman, J., Weertman, J., 1992. Elementary Dislocation Theory, 1st Edition. Oxford University Press.

Weygand, D., Poignant, M., Gumbsch, P., Kraft, O., 2008. Three-dimensional dislocation dynamics simulation of the influence of sample size on the stress–strain behavior of fcc single-crystalline pillars. Materials Science and Engineering: A 483-484, 188.

Xiao, S. P., Belytschko, T., 2004. A bridging domain method for coupling continua with molecular dynamics. Computer Methods in Applied Mechanics and Engineering 193 (17-20), 1645–1669.

Zadeh, L. A., Desoer, C. A., 2008. Linear System Theory: The State Space Approach (Dover Civil and Mechanical Engineering). Dover Publications.

Zienkiewicz, O. C., 1986. The Finite Element Method, 3 Edition. McGraw-Hill Companies.

Zimmerman, J., Kelchner, C., Klein, P., Hamilton, J., Foiles, S., 2001. Surface Step Effects on Nanoindentation. Physical Review Letters 87 (16).

Till Junge

Avenue de Beaulieu 10
c/o Sandra Penić
1005 Lausanne
☎ *+41 76 571 10 78*
✉ *till.junge@altermail.ch*

Education

Currently PhD candidate

Topic	Multiscale modelling of plasticity
Institution	Laboratory for Simulation in Solid Mechanics (LSMS), Swiss Federal Institute of Technology in Lausanne (EPFL), Switzerland
Supervisor	Prof. Jean-François Molinari

2008	**Master of Science in Mechanical Engineering**, EPFL, Lausanne Switzerland, 5.56/6.
2008	**Exchange semester**, *Massachusetts Institute of Technology (*MIT*)*, Cambridge, MA.
2006-2007	**Exchange year**, *Royal Institute of Technology*, Stockholm, Sweden.
2006	**Bachelor of Science in Mechanical Engineering**, EPFL, Lausanne Switzerland, 5.38/6.
2003	**High School Diploma**, *Alte Kantonsschule Aarau*, Aarau, Switzerland.

Master Thesis

Title	One Dimension Robot Juggler
Institution	Aerospace Controls Laboratory, MIT
Supervisor	Prof. Jonathan P. How
Description	Developed a control method for hybrid systems, applied to a juggling robot.

Academic Experience

Jul. 2007 - Feb. 2008	**Research assistant**, *Mechanical Systems Design Laboratory (*LCSM*)*, EPFL, Lausanne, Switzerland. Implemented a non-linear visco-elastic constitutive model for soft tissues
Nov. 2008 - Jun. 2009	**Doctoral Assistant**, *Laboratory for Applied Mechanics and Reliability Analysis (*LMAF*)*, EPFL, Lausanne, Switzerland. Simulation of soft tissues using a non-linear visco-elastic constitutive law. The project was dropped for lack of funding
Jun. 2009 - currently	**Doctoral Assistant**, LSMS, EPFL, Lausanne, Switzerland. Plasticity aspects of nano scale contact
2009, 2010, one month each	**Visiting student researcher**, *Brown University*, Providence, RI. Collaboration with Professor William A. Curtin on a 3D implementation of his coupled atomistics and discrete dislocations (CADD) method.

2011-currently, one month each year	**Statistical software developer**, *Université de Lausanne*, Lausanne, Switzerland. Development and maintenance of an open source R package (SPACOM) for multilevel analysis of spatially correlated data as part of civil service.

Teaching

Oct. 2004 - Feb. 2005, Oct. 2005 - Feb. 2006	**Teaching assistant**, *Laboratory for Production Management and Processes (LCPP)*, EPFL, Lausanne, twice 28 hours, about 100 students. Undergraduate statics for mechanical engineers
Oct. 2005 - Feb. 2006	**Teaching assistant**, LCSM, EPFL, Lausanne, 28 hours, about 50 students. Undergraduate introduction to mechanical engineering
Sep. 2007 - Feb. 2008	**Teaching assistant**, LMAF, EPFL, Lausanne, 28 hours, about 60 students. Undergraduate vibration mechanics
Sep. 2007 - Feb. 2008	**Teaching assistant**, LMAF, EPFL, Lausanne, 28 hours, about 60 students. Undergraduate introduction to the finite element method
Feb. 2009 - Jul. 2009	**Teaching assistant**, LMAF, EPFL, Lausanne, 28 hours, about 60 students. Undergraduate solid mechanics
Nov. 2008 - Feb. 2009	**Supervision of the Master Thesis of Patricia Scheuber**, LMAF, EPFL, Lausanne. Development of a traction experiment on pig tendons
Sep. 2009 - Jan. 2010 Sep. 2010 - Jan. 2011	**Teaching assistant**, LSMS, EPFL, Lausanne, twice 28 hours, about 100 students. Undergraduate structural mechanics
Sep. 2010 - Jan. 2011, Sep. 2011 - Jan. 2012, Sep. 2012 - Jan. 2013, Sep. 2013 - Dec. 2014	**Teaching assistant**, LSMS, EPFL, Lausanne, Four times 28 hours, from 100 to 130 students. Undergraduate introduction to continuum mechanics
Sep. 2011 - Jan. 2012	**Co-supervision of the Bachelor Thesis of Fabian Barras**, LSMS, EPFL, Lausanne. Implementation of structure elements for the finite element analysis code Akantu

Conferences and Workshop Presentations

1. **T. Junge, G. Anciaux, J.F. Molinari**, *Investigation of the size of plastic zones in nano indentation and nano scratching*, 1st EPFL Doctoral Conference in Mechanics, Lausanne, Switzerland, February 19th 2010.
2. **T. Junge, G. Anciaux, Curtin W.A., J.F. Molinari, T. Nogaret**, *Linking Discrete Dislocations and Molecular Dynamics in 3D: a Start*, IUTAM Symposium on Linking Scales in Computations: From Microstructure to Macro-scale Properties, Pensacola, FL, May 16-19, 2011.
3. **T. Junge, J.F. Molinari, G. Anciaux, W.A. Curtin**, *Coupling Atomistics and Discrete Dislocations in 3D: A Start*, Hermes 2012 Summer School, London, July 27-30, 2012.
4. **T. Junge, J.F. Molinari, G. Anciaux**, *Plastic activity in nanoscratch molecular dynamics simulations of pure aluminum*, 22th International Workshop on Computational Mechanics of Materials, Baltimore MD, September 24-26, 2012.

5. **T. Junge, J.F. Molinari, G. Anciaux**, *Plastic activity in nanoscratch molecular dynamics simulations of pure aluminum*, Engineering Science 49th Annual Technical Meeting, Atlanta GA, October 10-12, 2012.

Peer Reviewed Publications

1. **T. Junge, J.F. Molinari**, *Molecular dynamics nano-scratching of aluminium: a novel quantitative energy-based analysis method*, Procedia IUTAM 3 (2012), 192 -204.

Journal Articles

2. **T. Junge, J.F. Molinari**, *Plastic activity in nanoscratch molecular dynamics simulations of pure aluminium*, International Journal of Plasticity, Volume 53, Feb. 2014, 90-106.

Submitted Articles

3. **T. Junge, G. Anciaux, J.F. Molinari**, *Dynamic stability of ghost force-free atomistic/continuum coupling methods*, Submitted on May 13, 2014.
4. **J. Cho, T. Junge, J.F. Molinari, G. Anciaux**, *Dislocation core structures with several character angles in FCC Aluminum*, Submitted on July 17, 2014.

Computer Skills

Languages	C, C++(11), Fortran, Python 2/3, Matlab/Octave, SQL, R
Tools	GNU Emacs, LaTeX 2$_\varepsilon$, GCC, Swig, PostgreSQL, Lammps, ParaDiS, MPI, Blas/Lapack, Cmake
Miscellaneous	GNU/Linux, Windows, ARM and AVR embedded development

Languages

German	**Native**	
French	**Native**	*Bilingual childhood*
English	**Fluent**	*Cambridge Certificate in Advanced English (2002), spent 7 months in Boston, MA*

Fields of Expertise

- Computational solid mechanics using finite elements, molecular dynamics, discrete dislocations
- Concurrent multi-scale coupling schemes for solid mechanics
- Development of open-source simulation software